Electrophysiological Characterization of Microbial Rhodopsins

Dissertation

zur Erlangung des Doktorgrades
der Naturwissenschaften

vorgelegt beim Fachbereich Biochemie, Chemie und Pharmazie
der Johann Wolfgang Goethe-Universität
in Frankfurt am Main

von
Juliane Weissbecker
aus Ekibastus

Frankfurt am Main 2020
(D30)

vom Fachbereich Biochemie, Chemie und Pharmazie der

Johann Wolfgang Goethe-Universität als Dissertation angenommen.

Dekan	Prof. Dr. Clemens Glaubitz
1. Gutachter	Prof. Dr. Ernst Bamberg
2. Gutachter	Prof. Dr. Josef Wachtveitl

Datum der Disputation: _____

This work was carried out in the department of Biophysical Chemistry of the Max-Planck-Institute of Biophysics under the supervision of Prof. Dr. Ernst Bamberg.

Contents

1 Introduction

1.1 Optogenetics

The ability to control a single cell type in the brain while leaving others unaltered had long been a major challenge for neuroscience. In order to achieve the required spatial and temporal resolution for the task optical stimulation was identified as a possible tool. Light activation of neurons could be accomplished by different approaches e.g. using photolabile substrate cages for depolarizing ion channels [1] or genetically encoding a combination of phototransduction components to the target cells [2]. It was the discovery of the light-activated cation channel channelrhodopsin 2 (ChR2) from *Chlamydomonas reinhardtii* [3, 4], though, that would revolutionize the development of the field with the technology termed optogenetics.

Optogenetics combines genetic targeting strategies of light-sensitive proteins with fast optical control that allows to induce gain or loss of function events in specific cells. With the successful introduction of light-sensitivity to neurons by expressing ChR2 as a single-component optogenetic tool [5–7], its family of natural occurring light-driven proteins came into focus. The discovery of microbial rhodopsins (MRs), a family of photoactive retinylidene proteins, dates back to the early 1970's. Stoeckenius and Oesterhelt were the first to identify bacteriorhodopsin (BR) from *Halobacterium salinarum* as a light-driven proton pump [8]. In the following decades, scientists discovered MRs acting as ion pumps, channels and sensors that might be exploited as optogenetic tools. The first tool for neuronal hyperpolarization was the inward Cl^- pump halorhodopsin from *Natronomonas pharaonis* (NpHR) [9]. Expressing ChR2 and NpHR in neurons allows for signal activation or silencing by blue or yellow light, respectively (Figure 1.1) [10, 11].
The demands of different optogenetic applications triggered the search for more natural occurring MRs and the study of their properties. Essential features are the ion selectivity, kinetics, wavelength specificity and light sensitivity that were also optimized in engineered MRs by mutagenesis. A major challenge is the protein targeting and sufficient expression of potential tools and the ongoing research is essential for the extension of the optogenetic toolbox.

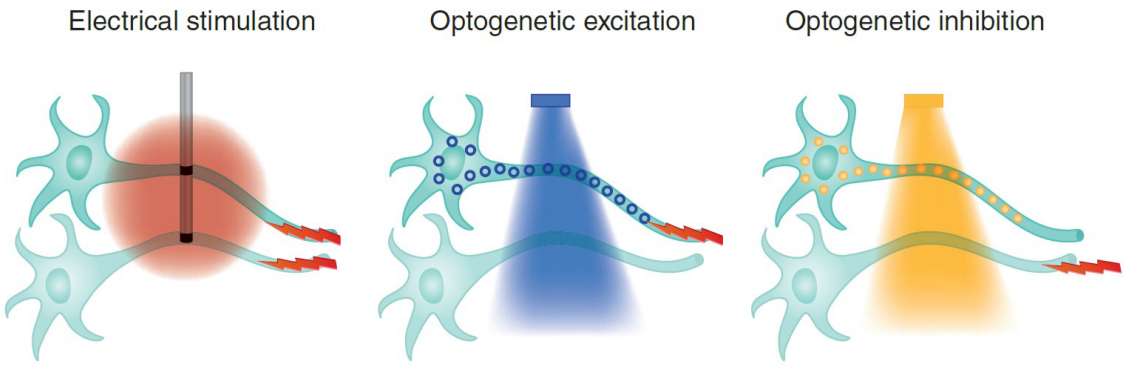

Figure 1.1: Optogenetics in neuroscience. The expression of e.g. ChR2 in targeted cells allows fast excitation of neurons with blue light. Cell specific inhibition of neuronal signaling can be achieved by exciting halorhodopsin proteins by yellow light. In contrast to the electrical approach with electrodes, the optogenetic approach allows specific excitation at the ms time scale. Image was taken from [12].

Although optogenetics evolved as a technique in neuroscience, its applications spread to different biological systems. The optical control of intracellular signaling pathways is not limited to excitable cells, but opens the door to essentially every tissue and cell type. Light-induced signaling of G protein-coupled receptor (GPCR) proteins was obtained by using vertebrate rhodopsin-GPCR chimeras (optoXRs) [13]. In other studies, light-induced control of GTPases involved in actin cytoskeletal dynamics was implemented [14, 15].
The regulation of the second messenger Ca^{2+} is involved in many important processes such as the cell cycle, the generation of action potentials and programmed cell death [16]. Manipulation of the Ca^{2+} signaling by light was accomplished by customized light-gated Ca^{2+} channels located in the plasma membrane or light-switchable ligands [17–19].

Optogenetics is a powerful research tool that enables the determination of causal links between activity in specific neuronal circuits and brain function and behavior in health and disease. Insights into the complex tissue functions in Parkinson's disease [20] and epilepsy [21] could be obtained by optical approaches. Besides the use in basic research, optogenetics has the potential to become a clinical tool for treating humans. The progress towards the restoration of vision in retinitis pigmentosa disease [22] and improved hearing prosthetics [23] is very promising and highlights the possibilities of this technique. A major challenge for future optogenetic applications is the precise cell-specific expression of optogenetic tools in living animals as well as their targeting to intracellular compartments.

1.2 Retinylidene Proteins

Light-sensitivity in retinylidene proteins (or rhodopsins) arises from the retinal chromophore which is a vitamin A aldehyde. The common seven-transmembrane-helix structure and the retinal bound to the seventh helix via a Schiff base (SB) linkage to the ϵ-amino group of a lysine residue are shared between all family members. The proteins are involved in two categories of biological functions: the light to energy conversion by creating electrochemical potentials and the initiation of intracellular signaling as photosensory receptors. The processes are initiated by an isomerization reaction of the chromophore that is followed by defined conformational changes of the protein in a sequence of intermediates that make up the characteristic photocycle.
Based on their primary sequence, type I and type II rhodopsins are distinguished. Type II rhodopsins that are also termed animal rhodopsins belong to the GPCR superfamily [24,25] and are involved in visual and nonvisual phototransduction [26,27]. Upon light absorption conformational changes of the protein enable the GDP/GTP exchange on heterotrimeric G proteins triggering the G protein signaling cascades [28].
Type I or microbial rhodopsins can be found in all three domains of life. Despite the common structural features and high sequence homologies MRs exhibit a large variety of functions (Figure 1.2). The ongoing search for new family members reveals more intriguing functions as in the case of a light-gated guanylyl cyclase from the fungus *Allomyces reticulatus* [29,30]. Amongst the most recently found proteins are the inward proton pump NsXeR [31,32] and the outward sodium pump KR2 [33] that are objects of this study. Extensive descriptions of retinylidene proteins can be found in [34,35].

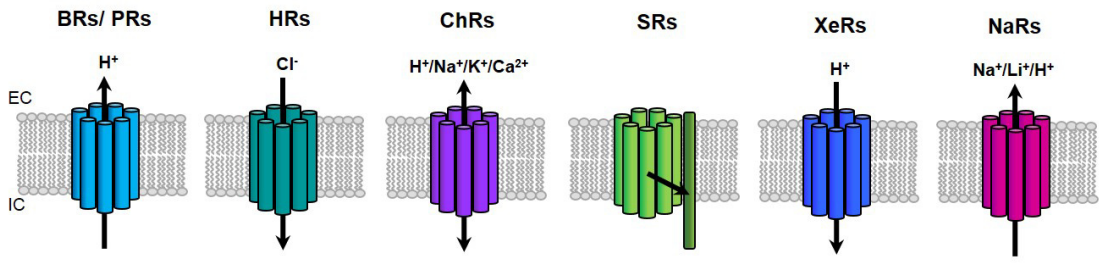

Figure 1.2: Functional variety of microbial rhodopsins. Arrows indicate the direction of ion transport or signal transduction to a transducer (here depicted as a transmembrane transducer protein). BRs: bacteriorhodopsins, PRs: proteorhodopsins, ChRs: channelrhodopsins, SRs: sensory rhodopsins, XeRs: xenorhodopsins, NaRs: Na^+-pumping rhodopsins.

1.3 Xenorhodopsins

In 2011, Ugalde *et al.* identified a new class of microbial rhodopsins that were named xenorhodopsins (XeRs) due to their diverse occurrence in five different Bacterial phyla and the Euryarchaeotal class Nanohaloarchaea [31]. XeRs are homologs of *Anabaena* sensory rhodopsin (ASR) [36], but opposed to the case of ASR no gene for a homolog of the ASR transducer protein could be found in genomes containing a XeR gene. The function of the new XeRs was unclear as also common features of proton pumps and halorhodopsins were not consistently shared [31].
Functional studies on several members of the family could prove that XeRs are a class of natural inward proton pumps [32, 37, 38]. Up to then only outward proton pumping rhodopsins like BR [8] or proteorhodopsin (PR) [39] were known. Outward proton pumps maintain proton gradients that are important for energy provision for biochemical reactions [40]. The function of the inward proton pumps in XeR-containing microbes is still elusive. So far, a sensory function similar to its homolog ASR is proposed [31].
In this work, the natural inward pump mechanism of XeR from the nanohaloarchaeon *Nanosalina* (NsXeR) [31] was studied. It was part of a metagenome from brines in Lake Tyrrell, Australia. First structural and functional studies on NsXeR were performed by Shevchenko *et al.* [32], but the underlying inward pump mechanism could not be fully resolved.

1.3.1 *Nanosalina* Xenorhodopsin

The light-induced inward proton pumping of NsXeR was demonstrated by pH measurements in *E. coli* or liposome suspensions and patch clamp experiments on mammalian cells [32]. Illuminating a suspension of NsXeR expressing *E. coli* led to an increase of the pH that decreased again when the light was turned off. The light-induced pH changes were completely abolished when the protonophore carbonyl cyanide *m*-chlorophenylhydrazone (CCCP) was added to the suspension.
Heterologous expression of NsXeR in human embryonic kidney (HEK) 293 and neuroblastoma glioma (NG) 108-15 cells yielded inward photocurrents in patch clamp measurements. The turnover rate for the proton pumping at a physiological membrane potential of -60 mV was determined to be $\sim$160 s^{-1}.
The general applicability of NsXeR in optogenetics was shown by the light-triggered spiking in rat hippocampal neurons with a firing success of 100% up to a frequency of 40 Hz [32].

NsXeR Structure

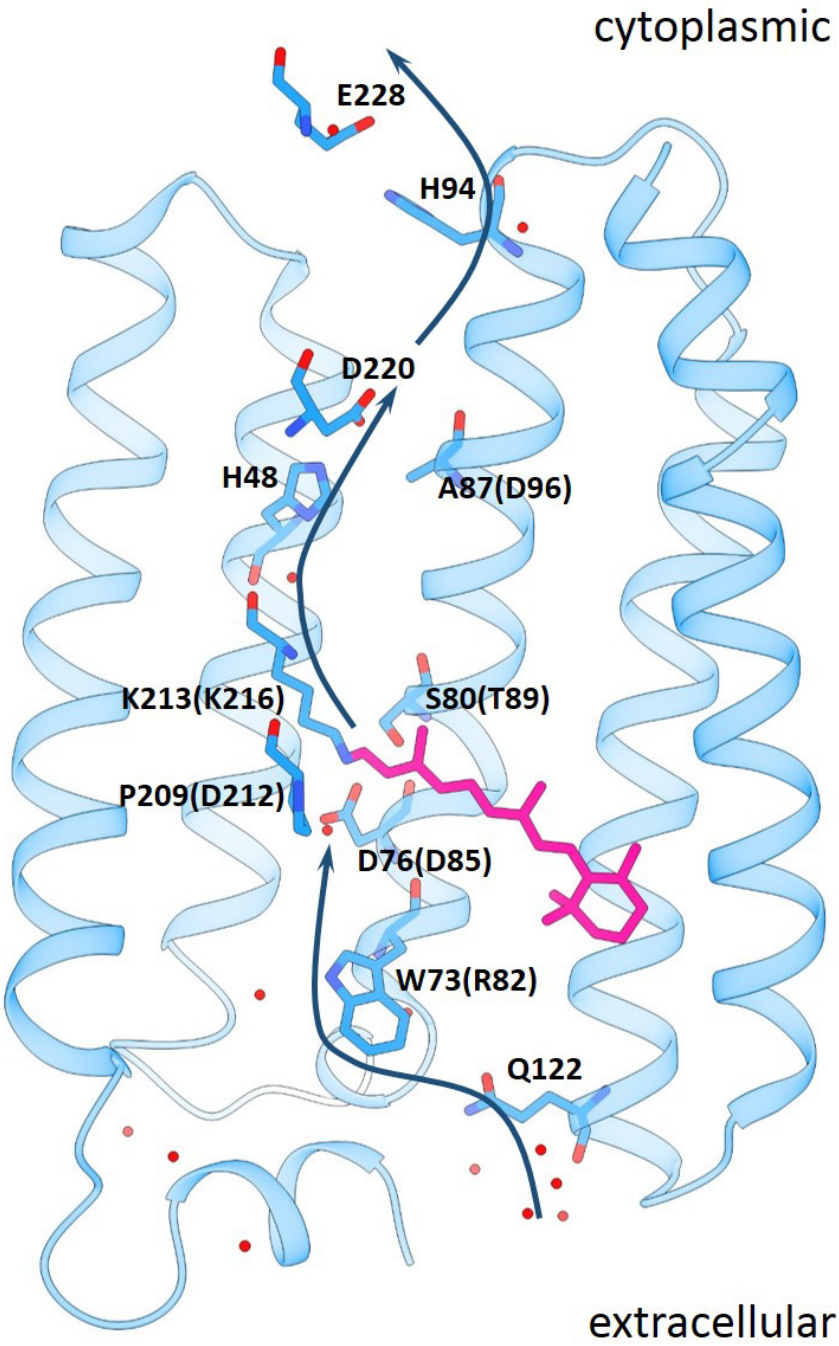

Figure 1.3: NsXeR structure (PDB ID: 6eyu) and putative ion translocation pathway. The all-*trans* retinal chromophore (pink) and key residues are shown. The numbers in brackets indicate the corresponding residues in BR. Red dots represent water molecules and helices six and seven are not shown. The putative proton translocation pathway suggested by [32] is marked by arrows.

The crystal structure of the NsXeR trimer was solved at a resolution of 2.5 Å [32]. The protein has seven transmembrane α helices (A-G) with an extracellular N-terminus and an intracellular C-terminus. A small N-terminal α helix precedes helix A and caps the extracellular side of the protein. The retinal chromophore is bound to Lys213 in helix G via a protonated Schiff base linkage. Compared to BR [41] helix A and G are significantly distorted. The highly conserved Asp212 (BR position) is replaced by Pro209 (NsXeR position) which is a substitution that is shared by all XeRs discovered so far [31].
The extracellular half of the protein contains cavities that are filled with water molecules. They are connected to the extracellular bulk via Gln122. Asp76, a residue in the active center close to the retinal Schiff base, is available to the uptake cavity through Tyr59. The connection between Asp76 and the Schiff base is mediated by a water molecule whereas the distance between Asp76 and the water is 2.9 Å and the water is located 3.2 Å away from the Schiff base in the dark state of NsXeR. Asp76 is found at the BR acceptor position Asp85 and is suggested to act as proton donor and SB counterion in NsXeR. The importance of the position is highlighted by the loss of color in Asp76 mutants. The position of Trp73 in the uptake cavity of NsXeR is typically occupied by a very conserved Arg residue (Arg82 in BR). It separates the uptake cavities from the active center and is critical for proton translocation. A chain of strong hydrogen bonds between residues of helix A and G (Ile6-Thr199-w5-Ser13-Ser202-w3-Trp73) is a unique feature of the NsXeR structure. It connects the active center with the extracellular bulk and is important for the stabilization of the protein.
The active center near the Schiff base in BR has a quadrupole structure made up of the positive charges of the Schiff base proton and Arg82 and the negative charges of Asp212 and Asp85 [41]. Therefore, the positive charge of the protonated Schiff base is stabilized by two negative charged counterions on the extracellular side. In the case of NsXeR a similar quadrupole structure cannot be found. The replacements of Asp212 and Arg82 (BR positions) by Pro209 and Trp73 (NsXeR positions), respectively, leave the Schiff base proton with a single negative charge at the extracellular side - the putative counterion Asp76.
The intracellular half of the protein holds a His48-Asp220 pair that is connected via a hydrogen bond. Asp220, located 12 Å from the SB, is the only ionizable residue close enough to be considered as a proton acceptor to the retinal SB. The residue corresponding to the proton donor Asp96 in BR is Ala87. Both His48 and Asp220 are crucial for proton pumping and are suggested to act as proton acceptor pair similar to the ones in PRs [42,43]. Thereby, the deprotonated state of the Asp is stabilized by the His-Asp interaction which lowers the Asp pK_a [43]. The residues His94-Glu228 located close to the cytoplasm are suggested to be part of the proton release pathway in NsXeR.

NsXeR Photocycle and Transport Mechanism

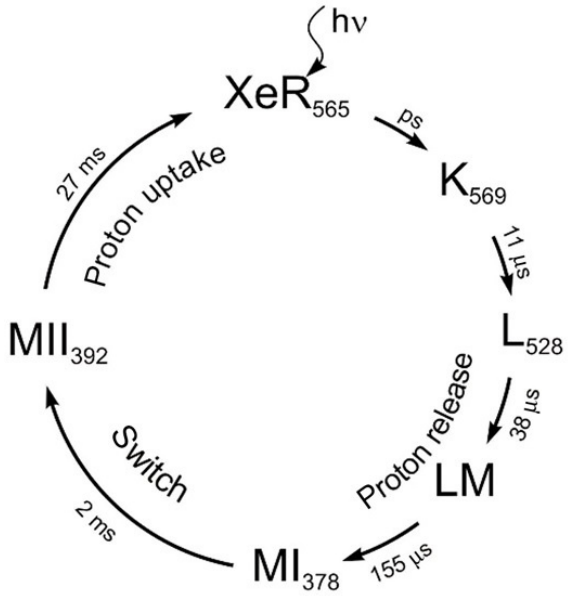

Figure 1.4: Photocycle model for NsXeR in nanodiscs at pH 7.5 and T = 20°C proposed by Shevchenko *et al.* [32].

In flash photolysis measurements Shevchenko *et al.* investigated the photocycle of NsXeR [32]. The description of the photocycle is commonly performed by comparison to the well known BR photocycle intermediates that were thoroughly reviewed in [44–47].
In nanodiscs as well as solubilized in detergent the protein has a ground state absorption maximum at 565 nm and no light dark adaptation could be observed. The predominant isomer fraction is in all-*trans* configuration and the Schiff base linkage is protonated. Upon light illumination the photocycle (Figure 1.4) is triggered with the 13-*cis* isomerization of the retinal leading to a red-shifted K-like intermediate (λ_{max} = 569 nm) that occurs in the picosecond timescale. It is followed by the blue-shifted L intermediate and a LM equilibrium state in the microsecond time domain. The first of two M intermediates, MI, rises with a half time of 155 μs. The M state is defined by a deprotonated Schiff base whose proton is transferred to an acceptor residue upon formation. The underlying mechanism in BR is a transient pK_a drop of the retinal Schiff base from over 13 in the ground state. The two spectrally and kinetically different M states in NsXeR are an unusual feature in retinal proteins. MI has three characteristic absorption maxima at 360, 378 and 398 nm, whereas the absorption spectrum of MII only shows a single band with a maximum at 392 nm. The transition between those states proceeds with a half time of 2 ms before MII decays back to the ground state with 27 ms.
For the transport mechanism of NsXeR Shevchenko *et al.* [32] propose that upon illumination the retinal isomerizes and the Schiff base proton is transferred to the putative acceptor

pair His48-Asp220 upon MI formation. The MI to MII transition was assigned to a switch that alters the accessibility to the Schiff base from the intracellular to the extracellular side. The MII decay is accompanied by the reprotonation of the Schiff base. The putative proton donor is Asp76 that has to be transiently protonated during the photocycle to fulfill its role.

1.3.2 *Parvularcula oceani* Xenorhodopsin

Another member of the XeR family was found in the α-proteobacterium *Parvularcula oceani* at 800 m depth in the south-eastern Pacific. The inward proton pumping of *Parvularcula oceani* rhodopsin (PoXeR) was first proven in *E. coli* suspension assays and in electrophysiological measurements on PoXeR expressing mouse neural cells by Inoue *et al.* [38]. Similar to NsXeR the protein arranges itself in trimers and has a maximum absorption wavelength of 568 nm. In the dark the chromophore of PoXeR has a 92% share all-*trans* retinal whereas exposure to light leads to equally distributed parts of all-*trans* and 13-*cis* retinal [38]. The photocycle of PoXeR was investigated from the picosecond to second time scale [38, 48] (Figure 1.5). It is about 10 times slower compared to NsXeR which makes the wild type unsuitable for optogenetic applications. Inoue *et al.* report that the M-intermediate with a deprotonated Schiff base appears with two distinct time constants (210 μs and 6 ms) [38].

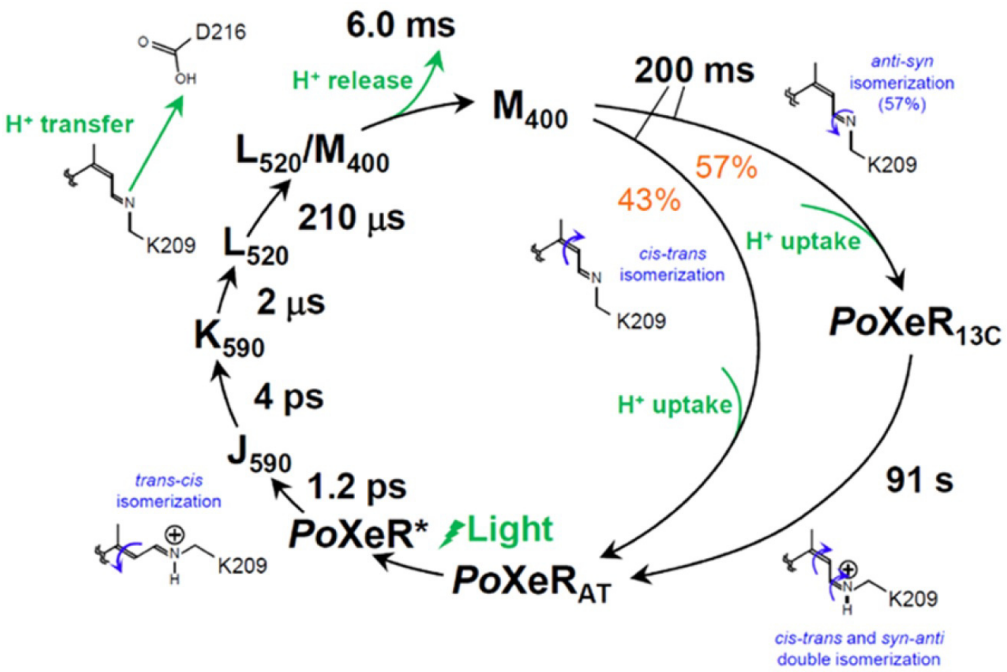

Figure 1.5: Photocycle model for PoXeR suggested by Inoue *et al.* [48].

Two states for L and M are shown with one which is in equilibrium (L/M). The primary proton transfer occurs from the protonated Schiff base to the acceptor Asp216 that was identified by difference FTIR spectroscopy. The proton release to the cytoplasmic side was assigned to the L/M to M transition using the pH sensitive dye pyranine [48]. Proton uptake from the extracellular was likewise attributed to the M decay whereby the proton donor could not be identified. In kinetic isotope effect (KIE) measurements a large effect for the proton release could be observed while the same for the M decay/proton uptake was considerably smaller. Different proton transfer mechanisms for proton uptake and release were concluded. The proton uptake was suggested to be limited by the thermal isomerization of the retinal that regulates the Schiff base pK_a. In the suggested photocycle the M decay is branched with two isomerization patterns from 13-*cis*-15-*anti* to 13-*cis*-15-*syn* and all-*trans*-15-*anti* (Figure 1.5). Similar to the $PoXeR_{13C}$ intermediate (Figure 1.5), in ChR2 a long-lived state P_4 was found that shows only small spectral differences to the ground state [49]. It was suggested that under stationary light the transition from P_4 to the ground state is sped up by the absorption of a second photon [4,49] which could also be the case for PoXeR.
Inoue *et al.* suggest that the vectoriality of the inward proton pump is determined by the interaction between the retinal Schiff base and its counterion. In outward proton pumps like BR two negative charges are located on the extracellular side of the Schiff base (Asp85 and Asp212). In XeRs Asp212 is replaced by a proline which leads to a weaker coupling between the Schiff base and the counterion Asp74 since the pK_a of Asp74 cannot be raised by a second negative charge [50].

1.3.3 *Rubricoccus marinus* Xenorhodopsin

The marine bacterium *Rubricoccus marinus* SD-29^T found in the western north Pacific carries the gene of the inward proton pump RmXeR. Inward proton pumping was verified by light-induced pH measurements of *E. coli* suspensions expressing RmXeR [37]. Similar to PoXeR a light-dark adaptation of the isomer distribution of all-*trans* and 13-*cis* retinal was observed with 75% all-*trans* in the dark- and 45% in the light-adapted state. From pH titration experiments and mutational studies the pK_a of the retinal Schiff base and the counterion Asp75 were estimated to 11.1 and 2.1, respectively. The maximal absorption wavelength of RmXeR (559 nm for 100% all-*trans*) was blue-shifted upon acidification of the medium which is opposed to the red-shift in BR wild type [51] and other outward pumps.
The photocycle of RmXeR shows three intermediates L, M and O (Figure 1.6). Inoue *et al.* [37] propose that upon M formation the retinal Schiff base it deprotonated to an

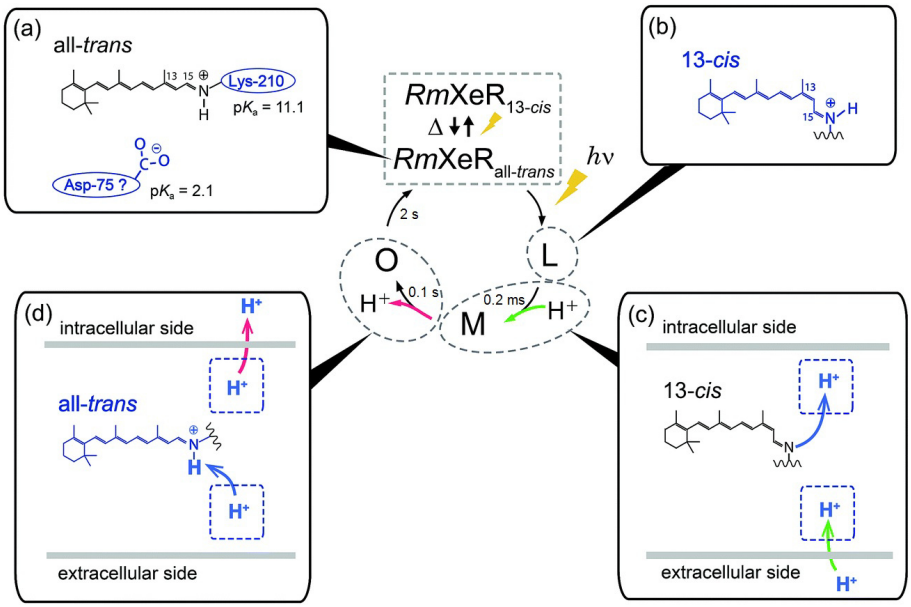

Figure 1.6: Photocycle model for RmXeR suggested by Inoue *et al.* (figure modified after [37]).

intracellular acceptor with Asp217 as a likely candidate. The M decay is accompanied by the reprotonation of the Schiff base from an unidentified transient H^+-binding site on the extracellular side. Due to an absorption increase and decrease of the pH sensitive dye pyranine with the M rise and decay, respectively, it is proposed that the extracellular H^+-binding site is protonated from the bulk during the L to M transition and Asp217 releases the bound proton to the intracellular during the M decay. The counterion Asp75 is not suggested to act as H^+-binding site since FTIR measurements suggest that Asp75 is in a deprotonated state at the M intermediate.

1.4 Na^+-pumping Rhodopsins

Before the discovery of the first Na^+-pumping rhodopsin from *Krokinobacter eikastus* (KR2) [33] the absence of sodium pumping in MRs was thought to be reasonable due to the positive charge of the transported ion. Cations other than protons were expected to be unstable near the positively charged protonated retinal Schiff base due to electrostatic repulsion.

Meanwhile, several Na^+-pumping rhodopsins (NaRs) could be found that share a common feature of conserved residues in the third transmembrane helix. The residues corresponding to Asp85, Thr89 and Asp96 in BR are replaced by Asn, Asp and Gln in NaRs [33]. The proton donor to the retinal Schiff base Asp96 and the negatively charged acceptor/counterion Asp85 in BR are substituted by neutral amino acids (Gln and Asp, respectively). Only

one carboxylic residue (Asp) remains at the position of Thr89 moving the counterion of the retinal Schiff base one helix turn to the cytoplasmic side in NaRs.
Since 2013, a growing number of family members was discovered [33, 52–57]. While exclusive outward sodium ion pumping is exhibited by e.g. *Gillisia limnaea* rhodopsin (GLR) and *Nonlabens marinus* rhodopsin 2 (NM-R2) [52, 53], also dual sodium ion and proton pumping is found in several NaRs like *Krokinobacter eikastus* rhodopsin 2 (KR2) and *Indibacter alkaliphilus* rhodopsin (IAR) [33, 55].

1.4.1 *Krokinobacter eikastus* Rhodopsin 2

The marine flavobacterium *Krokinobacter eikastus* collected at the Pacific coastline of Japan [58] carries the gene for KR2 that is the first reported outward sodium ion pump among MRs [33]. The above mentioned characteristic NaR residues are Asn112, Asp116 and Gln123 in the case of KR2. Under physiological marine environment sodium ions are transported from the cytoplasmic to the extracellular. KR2 also pumps Li^+ and protons when presented with salts of larger cations [33]. The successful inhibition of action potential firing in neurons proves the applicability of KR2 as an optogenetic tool [59, 60].

KR2 Structure

The first crystal structures of KR2 in the non-illuminated state were solved using crystals initially grown at a non-physiological acidic pH of 5.6 and lower. Two groups obtained highly similar monomeric structures from crystals grown at pH 4.3 and 4.0 [59, 61]. Since the physiological conditions for the KR2 pump activity are alkaline (pH 8 and 500 mM NaCl), approaches were made to solve the structure at a more neutral pH with contradicting outcomes for the SB region. Gushchin *et al.* raised the precipitant solution to 4.9 and 5.6 and firstly got crystals of KR2 assembled in pentamers [61]. It is assumed that the pentamer is the physiological oligomerization state as it was formed in biological membranes under acidic and neutral conditions confirmed by high-speed atomic force microscopy and dichroism spectroscopy measurements [62]. It was suggested that the monomeric form is a crystallization artifact.

Most recently, the KR2 pentamer ground state structure at 2.2 Å was obtained with crystals grown at pH 8.0 [63] that will be described in the following. The overall structure of KR2 resembles the classical MR fold of seven transmembrane helices with a retinal in the all-*trans* configuration that is bound to Lys255 in the seventh helix. Special features of KR2 are a short N-terminal α-helix and an elongated loop between helix two and three that forms a β-hairpin [59, 61, 63] (Figure 1.7). Inside the protein three cavities were resolved that are suggested to make up the ion translocation pathway: the ion uptake cavity

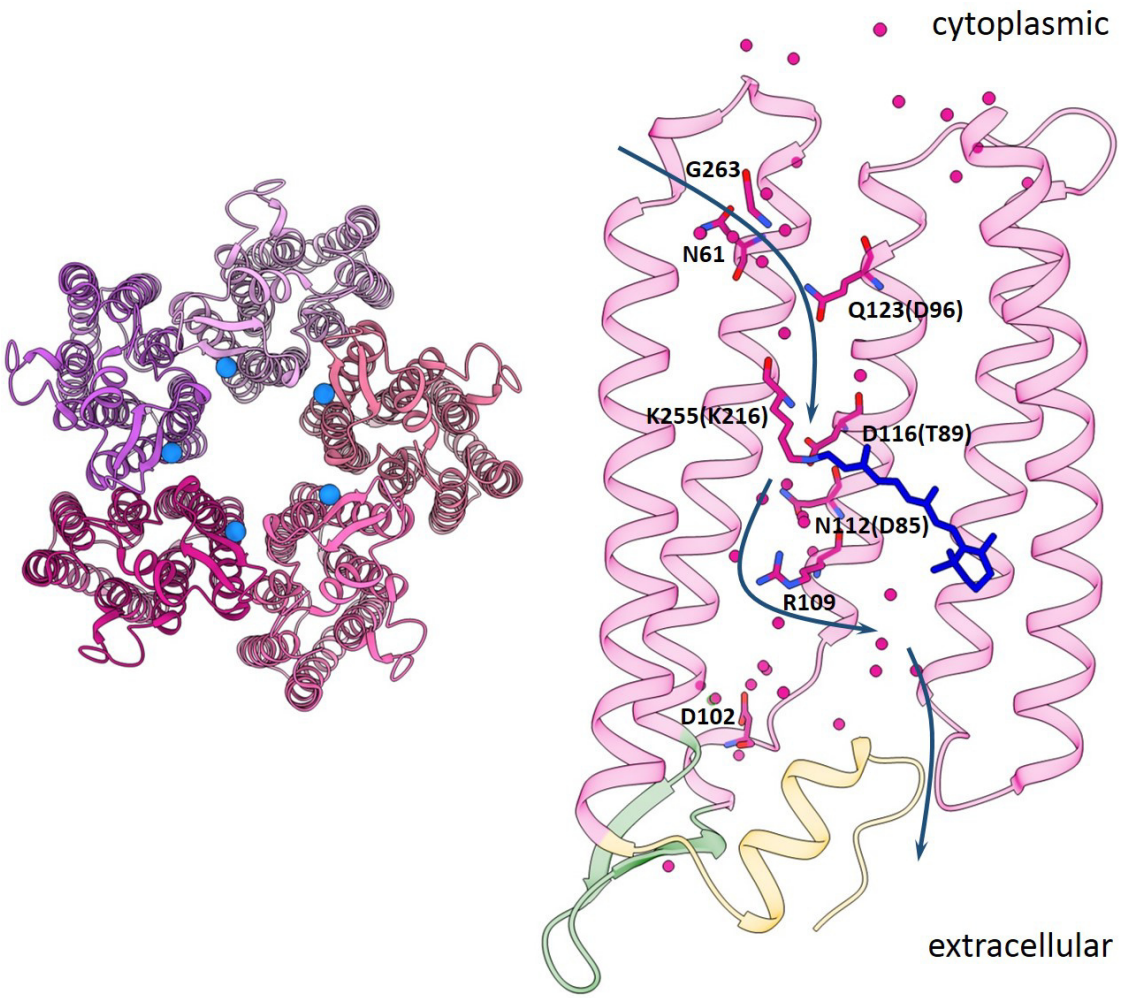

Figure 1.7: Structure of the KR2 pentamer (left) and protomer (right) at pH 8.0 (PDB ID: 6rew). The sodium ions bound at the oligomerization interfaces of the pentamer are indicated by blue spheres (view from the extracellular side). Helices six and seven of the protomer are not shown (right) and water molecules are indicated by pink spheres. Key residues and the all-*trans* retinal chromophore (blue) are shown. The numbers in brackets indicate the corresponding residues in BR. The N-terminal alpha helix and the extracellular β-hairpin are highlighted in yellow and green, respectively. The putative proton translocation pathway suggested by [63] is marked by arrows.

on the cytoplasmic side, the cavity near the retinal Schiff base and the putative ion release cavity.

The uptake cavity is filled with water molecules and reaches from the cytoplasmic protein surface to the residue Gln123 that is located at the level of the hydrophobic membrane core boundary [63]. The cavity is separated from the Schiff base by the hydrophobic residues Val67 and Leu120. The uptake cavity is unexpectedly large and is suggested to make up

the selectivity filter of Asn61 and Gly263 that occupies a position that is taken up by more bulky residues in other MRs. Mutating these residues leads to a gain of K^+- and Cs^+-pumping [59, 61, 64].
The cavity between the retinal Schiff base and Arg109 contains several water molecules and is surrounded by Trp113, Ser70, Asp116, Asp251, Asn112 and Leu74 [63]. Asp116, the primary proton acceptor, is hydrogen bonded to the retinal Schiff base with a distance of 2.6 Å [63]. The rather large size of the cavity is similar to conformations found in all ion-pumping rhodopsins with the ion bound in the active center [65].
The release cavity is separated from the Schiff base region by Arg109 and is capped by the N-terminal α-helix. The polar cavity contains the Glu11, Glu160 and Arg243 triad that was related to structural functions since neutralizing these residues did not abolish the Na^+ transport [33, 59, 61].

Although Na^+-binding in the KR2 ground state could be observed in ATR-FTIR difference spectra between NaCl and KCl [33], no bound sodium ion could be found inside the protein in all crystal structures [54, 61, 63]. In the crystallized KR2 pentamers sodium ions could be resolved at the oligomerization interfaces [61, 63] which explains why sodium binding was not found to be a prerequisite for sodium transport [33]. The extracellularly located Na^+ binding site consists of Asp102 of one protomer, Tyr25' and the main chain oxygens of Phe86' and Thr83' of the other protomer and a water molecule [61, 63].
Alterations of the interactions at the sodium binding site and the oligomerization interface around His30 were shown to impact the oligomeric assembly, the protein selectivity and the Schiff base Asp116 interaction [33, 66, 67]. A correlation between the ion-pumping activity and the oligomeric state was observed that was explained by the stabilization of the expanded conformation in the Schiff base cavity and the positioning of the cytoplasmic pore in the pentameric crystal structures. Therefore, pentamerization was suggested to be key to the Na^+-pumping activity of KR2 [63].
The crystal structure solved by Kovalev *et al.* at pH 5.0 showed unchanged locations for most residues [63]. Differences are slight displacements of residues 109 to 115 and the increased distance between Asp116 and the retinal Schiff base to 3.2 Å. The maximum absorption of KR2 crystals shifts from 528 nm to 550 nm with the pH change from 8.0 to 5.0 which indicates the protonation of Asp116. The weakened interaction between the SB and its counterion in solid-state NMR measurements was observed at pH 5.0 and similarly assigned to the protonation of Asp116 [68]. An additional difference is the positioning of Leu74 and Asn112 that occupy two alternative conformations. One is similar to the structure at pH 8.0, the other reduces the size of the Schiff base cavity similar to the compact conformation that was described in [65]. Kovalev *et al.* suggest that the protonation of Asp116 acts as the switch between the sodium and the proton pumping conformation of

KR2 [63] that is characterized by an expanded or compact Schiff base cavity. Alternatively, the low-pH form might be completely inactive which could be concluded from the abolished pump activity in D116N [33] if the compact Schiff base cavity corresponds to the protonated Asp116.

KR2 Photocycle and Transport Mechanism

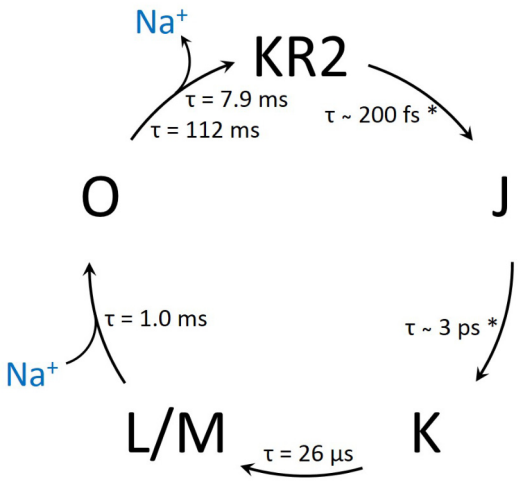

Figure 1.8: Scheme of the KR2 photocycle under sodium pumping conditions. Na^+ is suggested to be taken up upon O formation and released upon O decay. Time constants are taken from [33] except for the ones marked with * which were taken from [69].

The KR2 ground state has a maximum absorption wavelength of 526 nm [33] and contains 100% of all-*trans* retinal [66,68]. Upon illumination the retinal isomerizes and under sodium pumping conditions sequential intermediates J, K, L/M and O appear [33, 69] (Figure 1.8). The J and K intermediates are formed with ∼200 fs and ∼3 ps, respectively [69]. The equilibrium state L/M rises with 26 μs and decays with 1.0 ms whereupon the red-shifted O is formed. The retinal reisomerizes with the final transition of O to the ground state that happens with two time constants 7.9 ms and 112 ms [33]. Upon M formation the Schiff base proton is translocated to the acceptor Asp116 and returned from the same residue during the M to O transition [33]. Since the rise of the O intermediate was accelerated by high sodium concentrations it is assumed that Na^+ is taken up upon O rise [33]. As no Na^+ was bound inside the protein in the ground state, Na^+ is suggested to be released upon O decay [63,65].
Under proton pumping conditions the photocycle is considerably slowed down (>10 times slower at pH 8.0) and the accumulation of the O intermediate is significantly decreased [33].

For the sodium transport in KR2 different mechanisms were proposed [59,63,65]. Kato *et al.* suggested that the deprotonation of the Schiff base in M leads to a flipping motion of the protonated Asp116 that was also seen in computational studies [59, 70]. The retinal Schiff base region is proposed to act as switch and gate and a second gate is postulated at Arg109 and surrounding residues [71].
On the other hand, Kovalev *et al.* assume that the Schiff base region does not act as a gate [63]. A gate around Gln123 is suggested to open upon the M to O transition and Na^+ is translocated to the Schiff base cavity where it is transiently bound in the O state [63]. Arg109 is proposed to flip to the extracellular side opening the second gate upon O decay [63].

For the mechanism of dual proton and sodium pumping a switch model was proposed by Kovalev *et al.* as described above [63]. In contrast to that a competitive uptake model of sodium ions and protons was suggested that is based on the dependence of the M decay kinetics on sodium concentrations and pHs [72]. There, the proton pumping mechanism is described by a typical model for proton pumps [71]: the Schiff base proton is translocated to the acceptor Asp116, the retinal Schiff base is reprotonated from the intracellular and the proton bound to Asp116 is released to the extracellular side.

1.4.2 *Gillisia limnaea* Rhodopsin

Gillisia limnaea rhodopsin (GLR) is an example for a sodium ion pump of the NaR family without net proton transport. The sodium ion pump ability and the absence of proton pumping was determined by light-induced pH changes in *E. coli* suspensions as described above [52]. The insensitivity of the absorption spectrum to the Na^+ concentration shows that no sodium ion is bound in the ground state and a transient Na^+ binding site it formed during the photocycle. The NaCl dependence of a long-lived O intermediate reveals the existence of a high affinity Na^+ binding site (K_d = 60 μM) whose state of occupation is declared to act as a switch between a "Na^+-independent" and a "Na^+-dependent" branch of the photocycle [52]. The binding site it proposed to be created at the Schiff base counterion since the perturbation of the region by D251E resulted in the ability to bind Na^+ in the ground state. Candidates for the counterion/acceptor are Asp116 and Asp251. Although protons are not transported they are released and taken up during the photocycle which could be observed using the pH sensitive dye pyranine. Balashov *et al.* propose a tentative scheme for the ion transfer in the sodium dependent and independent photocycle branch (Figure 1.9).
Three binding sites are assumed in the scheme: the retinal Schiff base, a binding site for Na^+ and H^+ that includes the counterion and a release site for H^+ located in the

extracellular half of the protein. The Na^+ dependent branching occurs after the first M intermediate that is characterized by a deprotonated Schiff base and a proton bound to the extracellular release site. Earlier intermediates are Na^+ independent.
In the Na^+-independent branch a second M intermediate accumulates accompanied by a proton release to the extracellular. The reprotonation of the Schiff base limits the rise of the late O intermediate. During the M to O transition two protons are taken up from the extracellular that protonate the counterion site and the vacant release site. In the final transition the counterion is deprotonated again releasing the proton to the extracellular bulk without net proton transport [52].
In the Na^+-dependent branch the second M intermediate does not accumulate. It is suggested that Na^+ is taken up from the cytoplasmic bulk during the M to N transition accelerating the reprotonation of the Schiff base from the counterion. The rapid M to O conversion coincides with proton release and in the final transition to the ground state the sodium ion is released to the extracellular while the proton release site takes up a proton from the bulk [52].

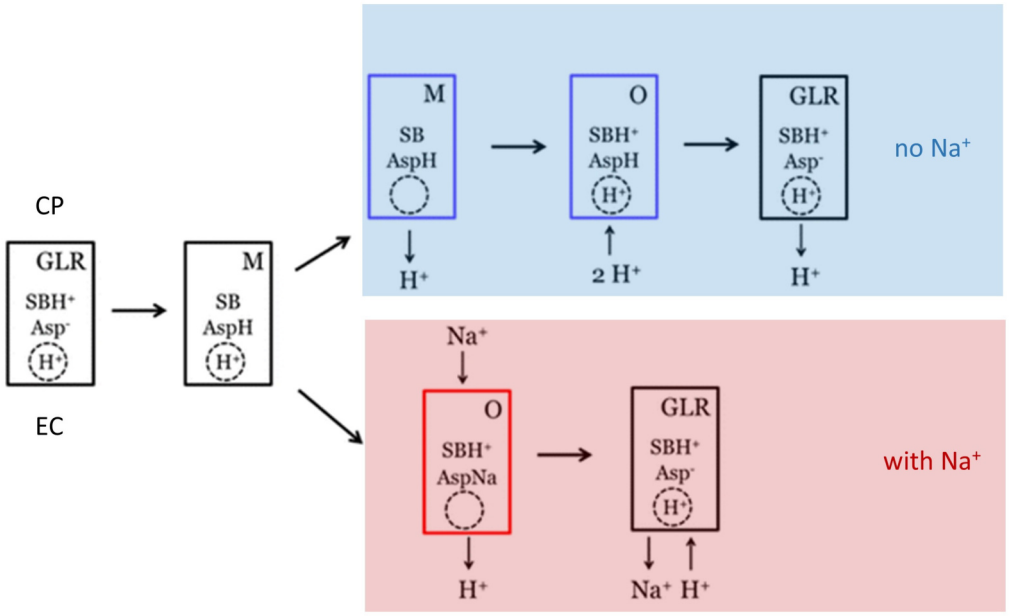

Figure 1.9: Scheme for the internal ion transfer and binding for GLR in the presence and absence of Na^+. SBH^+/SB: protonated/unprotonated retinal Schiff base; Asp: acceptor and ionizable part of Na^+ binding site; dashed circle: proton release site. Figure was altered from [52].

1.5 Blue-Light-Effect

The photocycles of MRs consist of a series of intermediates that differ in their maximal absorption wavelength. The M intermediate with its deprotonated retinal Schiff base is drastically shifted to around 400 nm [34]. Illuminating molecules in the M intermediate with blue light leads to an effect that was first described for BR. The proton transport of BR is inhibited by additional blue light illumination which is known as the quenching effect of blue light [73]. The molecular mechanism that is responsible for that is the photoisomerization of the 13-*cis* retinal to all-*trans* in the M intermediate. The retinal Schiff base is reprotonated from the primary acceptor (Asp85) on the extracellular side which short-circuits the pump cycle without net charge transfer across the membrane. In measurements of the steady-state photocurrents the additional blue light leads to a quenching effect with current amplitudes that are proportional to the amount of M intermediate present [74–76]. In BR the effect is dependent on the applied membrane potential, but the blue-light induced charge transfer is always opposed to the direction of the steady-state currents (Figure 1.10). A blue-light-effect was also observed in e.g. green proteorhodopsin with faster reprotonation kinetics compared to BR [77].

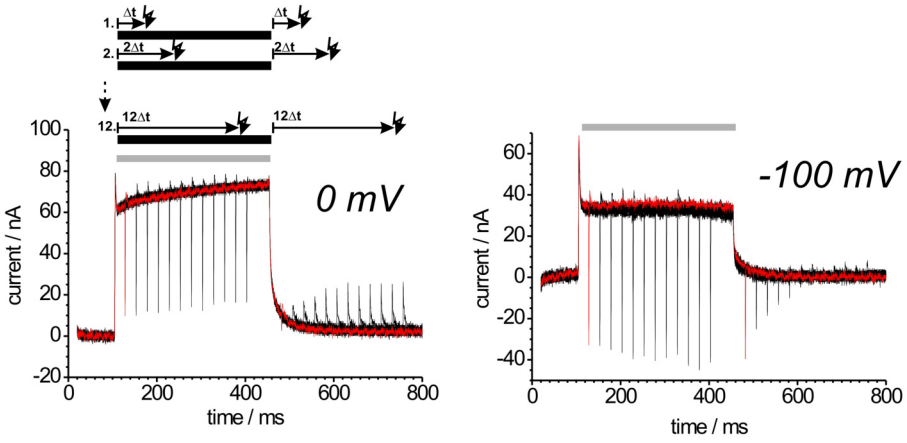

Figure 1.10: Photocurrents of BR expressed in *Xenopus* oocytes in response to continuous green light (grey bar) and additional blue laser flashes as indicated by the scheme. The applied membrane potentials were 0 mV (left) and -100 mV (right) (figure modified after [76]).

1.6 G Protein-Coupled Receptors

With more than 800 members the family of G protein-coupled receptors (GPCRs) make up $> 2\%$ of the total genes encoded in the human genome [78]. Most cellular reponses to hormones and transmitters are mediated by GPCRs which are also responsible for vision,

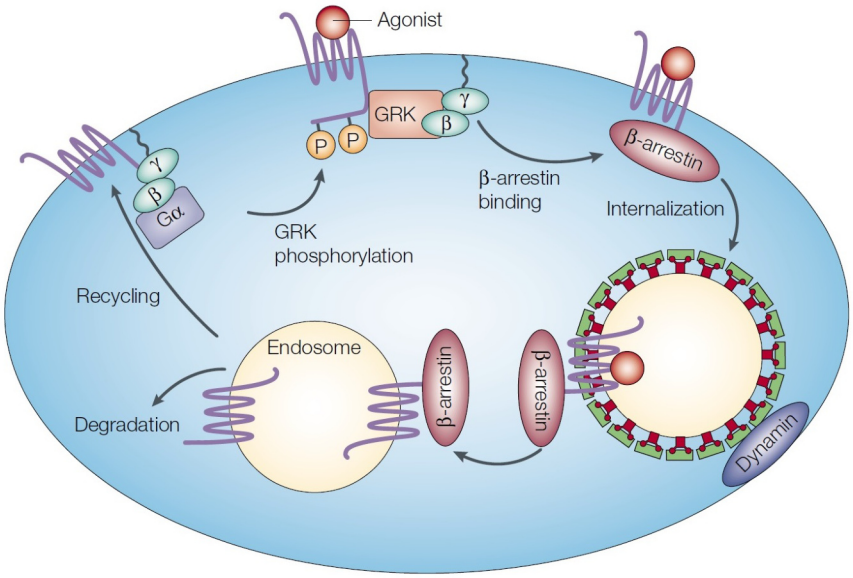

Figure 1.11: Ligand-induced trafficking of G protein-coupled receptors. Upon agonist binding downstream signaling is mediated by interaction with a G protein. The activated receptor is desensitized by G protein-coupled receptor kinase (GRK) phosphorylation that promotes β-arrestin binding. The β-arrestin-receptor complex is targeted to clathrin-coated pits and internalized into endosomes. The receptor is either recycled back to the cell surface or degraded. Figure from [28].

taste and olfaction [79]. Since their dysfunction leads to some of the most common diseases, most therapeutic agents sold worldwide either directly or indirectly target receptors of this family [28].

GPCRs share a structure of seven transmembrane α helices, but are activated by different agonists. Upon activation conformational changes of the receptor [80, 81] allow the interaction of intracellular sites with heterotrimeric G-proteins that contain α, β and γ subunits. The activated receptor catalyzes the exchange of a GDP, that is bound to G_α, for a GTP and the G protein dissociation into the G_α and the tightly linked $G_{\beta\gamma}$ subunit [82]. Both subunits stimulate separate downstream effectors whereby the signaling targets are determined by the coupling specificity between GPCR and G protein [83].
GPCR signaling is regulated by different mechanisms [28]. Fast receptor desensitization is controlled by G protein-coupled receptor kinases (GRKs) [84] by phosphorylation of serine/threonine residues in the intracellular receptor domain [85]. Phosphorylation promotes the binding of β-arrestin [86] which sterically inhibits the interaction between the G protein and the receptor. β-arrestin also targets the receptor to pre-existing clathrin-coated pits that are pinched off the cell surface by the large GTPase dynamin [87, 88]. After internalization into endosomes the receptors are either recycled back to the cell-surface

after ligand displacement and dephosphorylation enabled by endosome acidification [89] or sorted to lysosomes for degradation [90] (Figure 1.11).

1.6.1 C-X-C Chemokine Receptor Type 4

The chemokine receptor C-X-C chemokine receptor type 4 (CXCR4) is a rhodopsin-like GPCR that is involved in many biological processes including hematopoiesis, organogenesis and immune response [91–95]. CXCR4 is activated upon binding its agonist the CXC chemokine Stromal Cell-Derived Factor 1 (SDF1) [96] which occurs in different splicing variants e.g. SDF1α and SDF1β [97]. The predominantly expressed isoform is the 89 amino acid protein SDF1α which is expressed in all organs. SDF1β contains a four amino acid extension at the carboxyl terminus, is more resistant to blood-dependent degradation and is present in highly vascularized organs such as kidney, liver and spleen [97]. Binding of SDF1 is impaired by AMD3100 an antagonist to CXCR4 activation [98].
CXCR4 interacts with G proteins of the G_i subfamily that leads to the downstream regulation of processes like gene transcription, cell adhesion and cell migration [99]. Dysregulation of CXCR4 signaling plays a crucial role in many diseases such as cancer and WHIM syndrome [100]. High levels of CXCR4 in breast, prostate and gastric cancers are reported to promote invasion and correlate with increased metastasis [101–104]. Organs like lymph nodes, lungs and liver that express high levels of SDF1 are the most frequent secondary sites for metastasis which indicates that the CXCR4-SDF1 axis directs the trafficking of cancer cells [105]. CXCR4 was also identified to be a co-factor for the entry of the human immunodeficiency virus (HIV) into CD4+ T cells [106].

1.7 Aim of the Work

The subject of the present work is the characterization of the newly discovered inward proton pump NsXeR and the outward sodium ion pump KR2 that have the potential to extend the optogenetic toolbox with their remarkable ion transport properties. Further, an unconventional optogenetic application is studied with tandem proteins that combine the chemokine receptor CXCR4 with microbial rhodopsins which should allow intracellular activation of the light-sensitive proteins.

The inward proton pumping by NsXeR is an appealing property for a minimally invasive optogenetic tool since compared to the passive transporting channelrhodopsins its dependence on the electrochemical gradient is negligible. Despite first transport assays and structural analysis of NsXeR [32], the underlying mechanism for inward proton transport is still unclear. The aim of this study is the investigation of the molecular mechanism of NsXeR inward proton pumping. In more detail, the determinant of the pump vectoriality shall be researched and the important residues for proton transport identified. Further, the electrogenic steps in the NsXeR proton transport shall be investigated and assigned to the transitions in the NsXeR photocycle. To achieve this, the proton transport will be studied under control of the electrochemical gradient in patch clamp experiments and mutational studies will be performed on the putative proton donor (Asp76), acceptor (Asp220) and proton release group (Glu228-His94). Electrogenic steps will be identified using the black lipid membrane (BLM) technique on NsXeR reconstituted in proteoliposomes.
In situations where chloride and proton gradients should not be altered, the outward sodium ion pump KR2 could be a useful inhibitory optogenetic tool. Despite a number of KR2 Na^+ and H^+ transport studies [33, 54, 60, 61], the mechanism is not fully understood and the proton transport was only stated in *E. coli* assays [33] and BLM measurements on KR2 proteoliposomes [61]. The aim of this work is to extend the understanding of the molecular mechanism of the KR2 pumping by a thorough electrophysiological study. The applicability of KR2 in mammalian cells shall be studied and the active Na^+ and H^+ transport investigated in patch clamp measurements. Further, the kinetics and substrate dependences of the electrogenic steps will be researched in single turnover experiments and matched to the photocycle transitions.

The optochemokine tandems potentially enable intracellular light-activation of MRs. In this study, the remaining functionality of the cation channel CatCh in the tandem shall be shown. Also the internalization of the tandem triggered by the activation of the chemokine receptor CXCR4 will be examined by electrophysiological and imaging methods.

2 Materials and Methods

2.1 Molecular Biology

For the expression in mammalian cell lines the genes of interest were cloned into the pcDNA3.1(-) vector by Invitrogen. The vector provides a Cytomegalovirus (CMV) promoter to obtain high levels of expression. The human codon-optimized KR2 gene (UniProt ID N0DKS8) was amplified from a plasmid kindly provided by Dr. C. Bamann (MPI of Biophysics, Frankfurt am Main) performing a polymerase chain reaction (PCR). A backbone vector kindly provided by Dr. S. Kresak (MPI of Biophysics, Frankfurt am Main) was linearized using BamHI and SacII restriction enzymes and was fused with the KR2 insert by In-Fusion cloning. The final construct carried KR2 together with a membrane trafficking signal [107], a P2A self-cleaving peptide sequence [108] and the red fluorescent protein Katushka [109]. The membrane trafficking signal from the inward rectifying potassium channel Kir2.1 was added to increase the membrane surface expression of KR2 [107]. Preceding experiments revealed that the presence of a C-terminal fluorescent protein impairs membrane trafficking. The introduction of the P2A peptide sequence solved the problem, maintaining the 1:1 stoichiometry between KR2 and Katushka.
For the expression of NsXeR (UniProt ID G0QG75) an analogous construct was used that was kindly provided by V. Shevchenko and Prof. Dr. V. Gordeliy (Research Centre Jülich, Jülich, Germany) and described before [32].
The optochemokine tandems were cloned based on the tandem cassette that was previously described in detail [110]. Feldbauer *et al.* [111] introduced CXCR4 and replaced the fluorescent protein mKate by eYFP. The optochemokine tandems described in this work were combined with the cation channel Channelrhodopsin-2 mutant ChR2(L132C) [112] or the outward proton pump archaerhodopsin-3 Arch [113]. The genes were optimized to human codon usage.
Mutants of the genes were prepared by PCR based site-directed mutagenesis and verified by sequencing (Eurofins Genomics, Germany). Diagrams of the constructs used for expression im mammalian cells are illustrated in Figure 2.1.

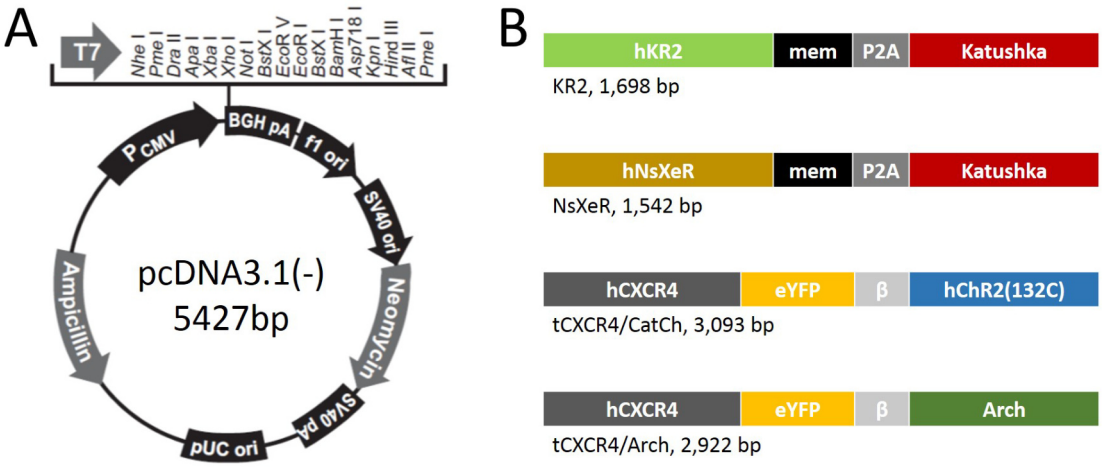

Figure 2.1: Vector and constructs used for heterologous expression in mammalian cells. (A) Expression vector pcDNA3.1(-) with multiple cloning site for the gene of interest under the CMV promoter (modified from the Invitrogen manual). (B) Diagrams of constructs used for this work. mem is a membrane trafficking sequence from Kir2.1 [107], P2A a self-cleaving peptide [108] and β, the β helix from the rat gastric H^+,K^+-ATPase β subunit [110].

2.2 Cell Culture

For the heterologous expression of the constructs the mouse neuroblastoma x rat glioma hybrid cell line NG108-15 was cultured. Cells were grown in small culture flasks containing 5 ml of the growth medium that consisted of Dulbecco's modified eagle's medium (DMEM) supplemented with 9 % fetal bovine serum (FBS) and 1% penicillin/streptomycin (100X). The NG108-15 cells were stored in an incubator at 37°C and 5% CO_2 until the confluency reached 80-90%. Twice a week the cells were subcultured and seeded in 24-well plates for transient transfection. The constructs described above were transfected by lipofection using the reagents Lipofectamine 2000 or LTX according to the instruction manuals. 1 μM all-*trans* retinal was added to the growth medium and the cells were incubated for 24-48 hours until the expression of the gene of interest was at a maximum.

2.3 Patch Clamp Technique

The electrophysiological properties of biological membranes can be studied using the patch clamp technique. The method, which is based on voltage clamp, was developed by B. Sakmann and E. Neher and first presented in 1976 [115]. The high background noise of former systems was reduced by an improved seal resistance between cell membrane and pipette tip allowing the direct measurement of single ion channel currents in the membrane of

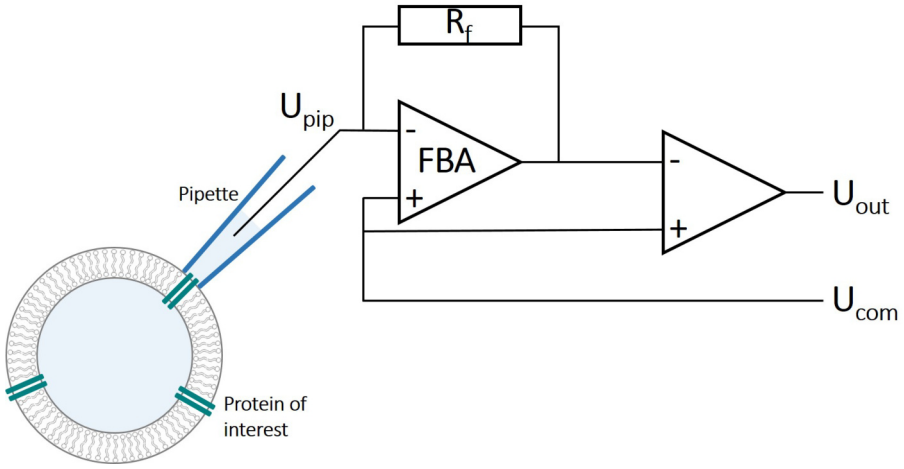

Figure 2.2: Simplified circuit diagram of a patch clamp amplifier. FBA: feedback operational amplifier, R_f: feedback resistor, U_{pip}: pipette potential, U_{com}: command potential, U_{out}: output potential. Image based on Figure 3.1 in [114].

living cells [115]. Further increase of the seal resistance up to 100 GΩ lead to a current resolution in the pA range [116]. In patch clamp measurements, the membrane potential is controlled by the injection of a compensational current through a negative feedback loop. A simplified diagram of the circuit can be seen in Figure 2.2. The central component is an operational amplifier FBA that compares the potential of the pipette U_{pip} and a dictated command potential U_{com} at the inverting and non-inverting inputs. The output of FBA, which is the amplified potential difference, is connected to the inverting input via the feedback resistor R_f. The potential difference between FBAs inverting input and output leads to a current through R_f (with $U_f = R_f \cdot I$) that can only flow into the pipette since the input resistance of FBA is infinite. This compensational current leads to a change of the pipette potential U_{pip} which takes on the value of U_{com}. In this manner, the pipette potential is controlled and the compensational current that is needed to do so can be determined from the proportional voltage U_f. U_f corresponds to U_{out} which is calculated by subtracting U_{com} from the FBA output using a second operational amplifier [114].

The formation of the giga-seal leads to a contact between glass pipette and cell membrane that is electrically tight as well as mechanically stable [116]. Therefore, measuring configurations with isolated patches become possible without losing the giga-seal. The cell-attached configuration is used when an intact intracellular environment is needed. It is also the starting point for the formation of whole-cell, outside-out and inside-out configurations that are depicted in Figure 2.3. The cell-attached configuration is achieved with the establishment of a giga-seal. The application of a suction pulse will break the membrane patch in the pipette and whole-cell measurements can be performed. The cy-

tosol is exchanged with the pipette solution and the macroscopic current of many channels or pumps can be studied. An inside-out patch where the intracellular side is exposed to the bath solution can be produced by pulling the pipette away in cell-attached. Doing the same with whole-cell as a starting point will lead to an outside-out patch with the extracellular side facing the bath solution [114, 116].
In this work, measurements are mainly performed in the whole-cell configuration in order to study the macroscopic currents under controlled intra- and extracellular solutions. Cell-attached is the configuration of choice for internalization experiments on the tandem constructs.

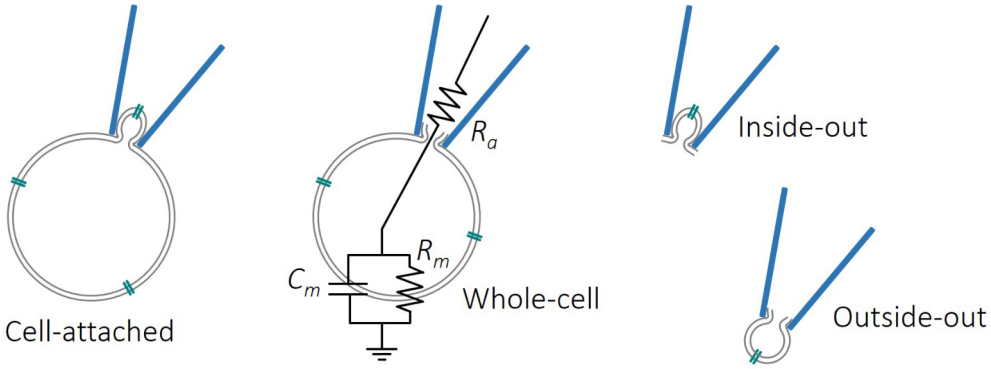

Figure 2.3: Patch clamp recording configurations with the equivalent circuit for whole-cell. Image based on Figure 9 in [116]. R_a = access resistance, C_m = membrane capacitance and R_m = membrane resistance.

2.3.1 Setups and Procedures

For the patch clamp measurements different setups were used (instruments summarized in Table 2.4), but the fundamental components and work flows were identical. The setups were equipped with an Axiovert microscope holding the measurement chamber on a vibration-damped table that allowed the optical control of the cells and the patch-pipette. The patch clamp headstage that holds the patch pipette was mounted on an electrical micromanipulator which was connected to an Axopatch 200B amplifier. The amplifier in turn was connected to a computer equipped with the pCLAMP software via a digitizer. The measurement chamber was filled with the bath solution (Table 2.2) and was in contact to the external Ag/AgCl electrode by the use of a salt bridge filled with 1.5% agarose in 150 mM KCl. The table holding the microscope was surrounded by a Faraday cage in order to reduce electrical noise in the recordings.
Light pulses were produced by laser systems and guided to the measurement chamber with fiber optics. In the case of continuous illumination measurements, the pulse duration was regulated by electrically controlled shutter systems. For the patch clamp measurements

the NG108-15 cells were placed on cover slips that were positioned in the measurement chamber. Thin-walled borosilicate glass capillaries were used to prepare patch pipettes with resistances between 2-5 MΩ for whole-cell and 1-2 MΩ for cell-attached measurements. The pipettes were carefully filled with pipette solution (Table 2.2) and mounted onto the headstage. A positive pressure was applied to the pipette while is was brought into contact to the bath solution. The pipette was positioned close to a cell that was singled out based on its fluorescence and the zero potential was corrected so that no current flow between bath and pipette was measured. Upon first contact between pipette and cell a negative pressure was applied to facilitate the formation of a giga-seal. When the cell-attached configuration was obtained, the cell was detached from the cover slip and repositioned in front of the light fiber. In case of cell-attached measurements the recordings could be started. A short pressure pulse was applied in order to break through the membrane patch in the pipette before the whole-cell recordings were performed. The membrane capacitance and resistance as well as the access resistance were noted. The access resistance R_a and the cell capacitance C_m (Figure 2.3) act as a lowpass filter with a corner frequency of $f_c = 1/(2\pi R_a C_m)$ limiting the time resolution of the measurements. The recordings selected for analysis had an access resistance of $R_a < 10$ MΩ. In continuous illumination measurements, the closing time of the shutter between 0.5 and 0.8 ms further affected the time resolution of the current decay kinetics.

In measurements on NsXeR expressing NG108-15 cells, membrane potentials between -100 mV and +60 mV with an interval of Δ+20 mV were applied. At each membrane potential the cells were illuminated for 450 ms at a wavelength of 561 nm with a saturating light intensity of 23 mW/mm^2. The current traces were sampled at 100 kHz and filtered at 5 kHz with a lowpass Bessel filter.
In pulsed illumination measurements, the cells were illuminated with a 7 ns light pulse at an intensity of 10^{20} photons/m^2. The traces were recorded with a sampling rate of 20 kHz and filtered at 5 kHz.

Recordings on KR2 expressing cells were performed in whole-cell configuration only. Membrane potentials between -120 mV and +60 mV were applied (Δ+20 mV) and the cells were continuously illuminated for 250 ms at a wavelength of 532 nm with a light intensity of $>$ 16 mW/mm^2. The signals were sampled at 100 kHz and filtered at 5 kHz.
In single turnover measurements, the cells were illuminated with a 20 ns light pulse at 532 nm with a light intensity of 10^{20} photons/m^2. A sampling rate of 200 kHz was used and the signals were filtered at 10 kHz. In order to improve the signal to noise ratio, up to 10 current traces were averaged. For the analysis of the exponential currents decays (Figure 2.4) the current was logarithmically reduced.

The internalization measurements on tCXCR4/CatCh expressing NG108-15 cells were performed in a temperature-controlled measurement chamber at 34°C. The membrane potential was set to -100 mV and the cells were illuminated for 100 ms at a wavelength of 473 nm at light intensities of > 10 mW/mm^2. Upon forming of the giga-seal the photocurrents were measured every 2 min. The whole-cell measurements on tCXCR4/CatCh and CatCh were performed at room temperature. Membrane potentials between -100 mV and +40 mV were applied (Δ+20 mV) and the cells were illuminated for 450 ms. The currents were digitized at a sampling rate of 100 kHz and low-pass filtered at 5 kHz.

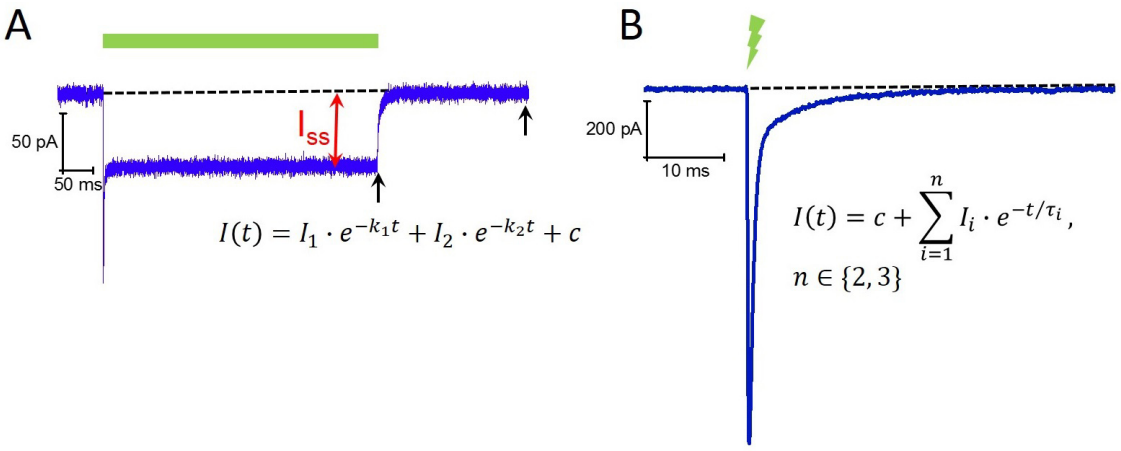

Figure 2.4: Example for the signal analysis from continuous (A) and pulsed illumination (B) measurements in patch clamp recordings on NsXeR. (A) The green bar indicates the illumination period. The steady-state photocurrents I_{ss} are indicated as the difference between the constant currents under illumination and the dark currents. The current decay after the end of the illumination (black arrows) was fitted with a biexponential function. (B) The green flash indicates the pulsed illumination. The current decay in these kind of measurements was fitted with an exponential fit function with two of three components.

The analysis of the patch clamp recordings was performed as indicated in Figure 2.4. The steady-state photocurrents were determined by subtracting the dark currents (outside of the illumination interval) from the the constant currents during illumination (Figure 2.4 A). The current decay after continuous illumination was fitted with a biexponential function in measurements on both NsXeR and KR2 where the faster component was compromised by the shutter closing time as mentioned above. In pulsed illumination measurements (Figure 2.4 B) the current decay was fitted with an exponential fit function with two or three components in measurements on NsXeR and KR2, respectively. Significance between results were tested using a one-way ANOVA test.

2.4 Atomic Absorption Spectrometry

Flame atomic absorption spectrometry (AAS) was used in order to determine the sodium concentration of sodium "free" patch clamp solutions. The solution to be investigated was atomized using an air/acetylene flame and the atomic absorption of the sample was measured using a sodium hollow cathode lamp and a detector. The absorbance of six standard solutions with known sodium concentrations was used to determine their relation that follows the Lambert-Beer law:

$$A = \epsilon \cdot l \cdot c \tag{2.1}$$

with the absorbance A, the molar extinction coefficient ϵ, the optical path length l and the concentration c. The residual sodium concentration in the bath solutions was < 50 μM and in pipette solutions a residual sodium concentration of ≈ 200 μM was found that can be traced back to the EGTA used (Table 2.2).

2.5 Protein Expression, Solubilization and Purification

The NsXeR protein used in this work was either kindly provided by V. Shevchenko (Institute of Complex Systems, Jülich, Germany) and purified as described in [32] or prepared as follows. C43(DE3) cells were thawn on ice before 50 μl of the cells and 1 μl (10 ng/μl) of the pET-15b vector carrying the NsXeR gene were mixed and put on ice for 30 min. Transformation of the cells was carried out by a heatshock for 45 s at 42°C. The cells were immediately cooled on ice for 2 min before 500 μl of preheated (42°C) NZY-medium was added. The mixture was shaken for 1 h at 225 rpm and after that 150 μl were plated on a LB-ampicillin agar plate. The plate was incubated over night at 37°C. The following day a clone was picked and put in 300 ml LB-ampicillin medium for the preculture that was grown up to an optical density (OD) of 1.5. The preculture was added to six 1 l flasks with M9 mineral medium (Table 2.1) for the main culture that was started with an OD of 0.05. The flasks were shaken at 37°C until an OD 0.8, then 0.5 mM IPTG and 5 μM all-*trans* retinal were added. The temperature was reduced to 30°C and the cells were left to shake over night.

The next day, the cells were centrifuged at 4°C and 5000 rpm and the pellet was solved in the breaking buffer (Table 2.1) with 1 mM PMSF (a protease inhibitor) and 2 μM all-*trans* retinal. After addition of DNase the mix was stirred for 30 min at 4°C, filtered through gauze and again 1 mM PMSF was added. The cells were disrupted using a microfluidizer and then centrifuged for 15 min at 4°C and 4700 rpm. The supernatant was again centrifuged at 100 000g and 4°C for 1 hour and the pellet was resuspended in buffer A (Table

2.1) and homogenized using a potter. 1 mM PMSF was added and the mix was stirred at 4°C before addition of 1% w/v DDM and further overnight stirring at 4°C. The following morning the protein was centrifuged at 100 000g at 4°C and the supernatant was filtered. The protein was purified using the ability of the histidines in the proteins His-tag to coordinate metal ions and, therefore, bind to a carrier material. A 5 ml HisTrap HP column that is packed with Ni Sepharose was mounted to an ÄKTA protein purification system. The column was equilibrated with 5% buffer B + 95% buffer A (5% imidazole) and loaded with the protein suspension. The protein was washed from the column at 50% buffer B and the fractions with enhanced 540 nm absorption were pooled.
The protein was concentrated using an ultracentrifuge filter (50 kDa cutoff) at 1400g for 45 min at 4°C and the imidazole was separated from the protein using a HiTrap Desalting column. The column is packed with Sephadex G-25 Superfine resin that retards the passage of small molecules through the column upon washing with buffer A + 0.03% DDM. The fractions with high 540 nm absorption were again pooled and concentrated to a final concentration of 3 mM. The protein was frozen in liquid nitrogen and stored at -80°C.

2.6 Preparation of Proteoliposomes

For measurements using the black lipid membrane technique, purified NsXeR protein was reconstituted in proteoliposomes. *E.coli* polar lipids were dried under nitrogen atmosphere by rotary evaporation. The dry lipid film was hydrated with a solution containing 100 mM NaCl, 20 mM Hepes, 20 mM H_3BO_3 and 20 mM $C_6H_8O_7$ adjusted to pH 7.4. The lipid suspension was vortexed and agitated during a hydration time of about 30 min. After adding 1.5% Tris-cholate (from a 10% cholate in 265 mM Tris pH 7.4 stock solution) to the suspension, it was left to rest and occasionally vortexed for 30 min until the suspension appeared opalescent. Purified NsXeR protein was added and the mixture was incubated on ice for 10 min. Detergent-absorbing Bio-Beads were added to the mixture in a volume ratio of 1:2 and the preparation was agitated at 4°C over night. The Bio-Beads were removed and the proteoliposomes were stored on ice until use. The usual preparation volume was 600 μl with a lipid concentration of 10 mg/ml and a protein concentration of 10 μM yielding a protein to lipid ratio of 1:40 (w/w).

2.7 UV-Vis spectroscopy

UV-Vis spectra of NsXeR wild type and the mutants D220E/N were measured at different pH values using a Varian Cary 50 Bio UV-Visible Spectrophotometer. The protein was solubilized with 0.05% of the detergent n-dodecyl-β-D-maltoside (DDM) in an aqueous

solution of 100 mM NaCl, 20 mM Hepes, 20 mM H_3BO_3 and 20 mM $C_6H_8O_7$. The solution was adjusted to different pH values by adding small amounts of 1 N NaOH or HCl and the pH was monitored. The measurements were performed at approximately 25°C and the pH was adjusted under room light. By titrating back to the original pH, the reversibility of the spectral changes was checked. For the determination of the retinal Schiff base pK_a, the relative absorbance changes were calculated. The wavelengths of maximal changes were plotted against the pH and fitted using the logistic fit function:

$$\Delta Abs = \frac{A}{1 + 10^{n(pK_a - pH)}} \tag{2.2}$$

with n that can be regarded as the Hill coefficient and the amplitude of absorption change A. The fitted data gave values of n<1. The significance between the maximal absorption wavelengths and the Schiff base pKas was tested using a one-way ANOVA test with a post hoc Bonferroni analysis.

2.8 Black Lipid Membrane Technique

The black lipid membrane (BLM) technique is an electrophysiological method based on a capacitively coupled system that allows the investigation of electrogenic processes in ion pumps and channels with a high time resolution. First described by Mueller *et al.*, black lipid membranes are lipid bilayers spanning a pore in a thin Teflon sheet that separates two electrolyte-filled chambers [117] (Figure 2.5). The addition of proteoliposomes to one of the chambers leads to adsorption to the black lipid membrane. The electrolyte solutions of both chambers are connected to an external circuit. Upon triggering of a charge displacement by the protein of interest, a compensatory charge must move in the external circuit that can be measured as a current or voltage signal.
The measurement of the photovoltage is advantageous since it is directly proportional to the transported charge [118]. In these kind of measurements, the fast transport components are limited by the rise time of the recording system while the measurements of slow transport steps are limited by the passive discharge components of the system. The equivalent circuit indicated in Figure 2.5 can be used to explain the electrical behavior of the system. Assuming that only a very small percentage of the black lipid membrane is covered with proteoliposomes, the following expressions can be derived for the two passive discharge components [118]:

$$k_{sys\,1} = \frac{1}{A \cdot R_s \cdot C_m} \tag{2.3}$$

$$k_{sys\,2} = \frac{G_p}{C_p + C_m} \tag{2.4}$$

A: membrane area, R_s: input resistance of the amplifier, C_m: specific capacitance of the BLM, G_p: specific conductance of the proteoliposomes, C_p: specific capacitance of the proteoliposomes. C_m, G_p and C_p are normalized with respect to the membrane area. While $k_{sys\,1}$ is affected by the input resistance of the amplifier, $k_{sys\,2}$ is only dependent on specific membrane properties. Their amplitude ratio should equal $-k_{sys\,1}/k_{sys\,2}$ [118].

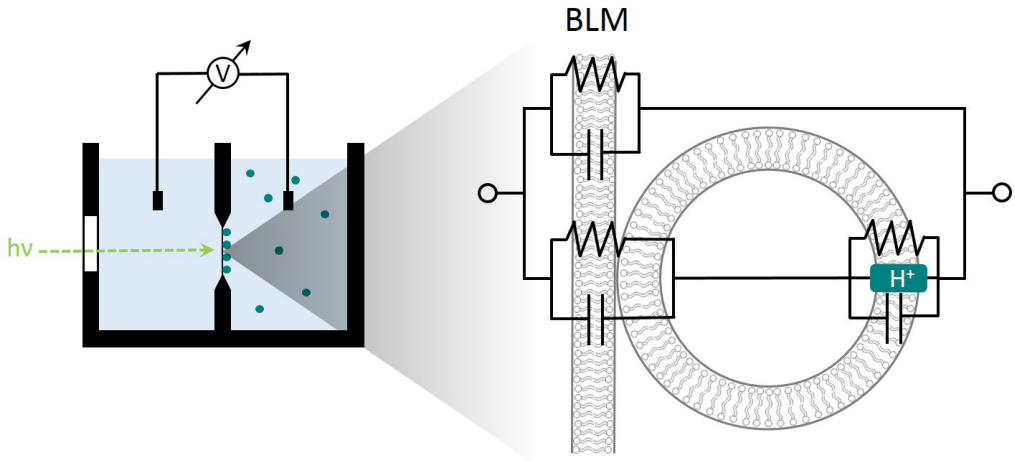

Figure 2.5: Scheme of a BLM setup. The electrolyte-filled chambers of a Teflon cell are separated by a black lipid membrane. Proteoliposomes that were added to the chamber averted to the light adsorb to the BLM. Charge displacements can be measured in an external circuit that is connected to the chambers. The setup can be described by an equivalent circuit as indicated.

2.8.1 BLM Setup and Procedures

For the photovoltage measurements on NsXeR proteoliposomes, a Teflon cell with a 1 mm^2 pore area was used. The pore was impregnated with a solution containing 1,2-diphytanoyl-sn-glycero-3-phosphocholine (DPPC) lipids in hexane before both chambers were filled with 1.3 ml of an aqueous solution of 100 ml NaCl, 20 mM Hepes, 20 mM H_3BO_3 and 20 mM $C_6H_8O_7$ at pH 7.4. The black lipid membrane was prepared using the membrane-forming solution containing 1.5% (w/v) DPPC and 1:60 (w/w) octadecylamine to DPPC dissolved in decane. The membrane properties were checked by application of a triangle potential or potential jumps while measuring the current signal. The membranes used had a capacitance and conductivity of around 2-2.5 nF and 10-100 pS, respectively. The freshly prepared proteoliposomes were sonicated for 1 min and 15 μl was added to the chamber averted to the light source. Magnetic stirrers ensures the even distribution of the proteoliposomes.

After at least an hour of incubation time, 5 μM of monensin were added to both chambers in order to abolish possible proton gradients between exterior and interior of the

proteoliposomes. After at least 30 min the measurements were started. Both chambers of the Teflon cell were connected to the external measuring circuit using salt bridges and Ag/AgCl electrodes. The electrically sensitive parts of the setup were surrounded by a Faraday-cage that was located on a vibration-damped table. The photovoltage signal was amplified by a factor of 66 before it was coupled into a SR560 low noise preamplifier that filtered the signal with a 300 kHz cut-off frequency. The further amplification was usually set to 1. The signal was recorded using a digital oscilloscope that successively wrote the photovoltage with two sampling rates: 1.28 μs and 81.92 μs. The time resolution of the electrical recording system yielded a 10-90 rise time of 3 μs.
The NsXeR proteoliposomes were illuminated through a window in the Teflon cell by 20 ns light pulses at 556 nm using an excimer laser pumped dye-laser. For the pH titration measurements, the electrolyte solutions of both chambers were adjusted to different pH values by addition of small amounts of 1N NaOH or HCl. To make sure that the pH was stable, the measurements were repeated four times at each pH value. The final pH was checked after the titration and the maximal deviation from the intended value found was 0.13.

The sets of data with different sampling intervals were combined and the data density reduced with increasing time using a LabTalk script (written by Dr. C. Bamann, MPI of Biophysics, Frankfurt am Main). The signals were normalized to the maximum value.

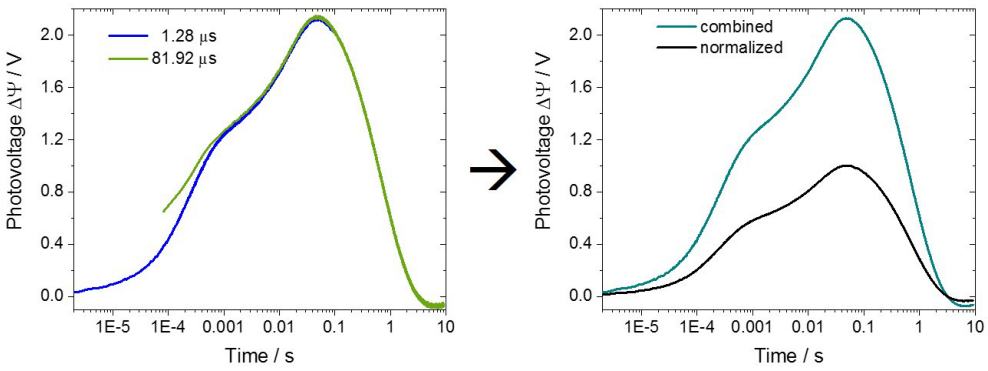

Figure 2.6: Example for the data combination of BLM measurements with different sampling intervals 1.82 μs and 81.92 μs. The signals were logarithmically reduced and normalized.

The photovoltage signal was exponentially fitted including the relaxation of the signal due to the passive system discharge components:

$$\Delta\Psi(t) = \Delta\Psi_I \cdot e^{-t/t_1} + \Delta\Psi_{II} \cdot e^{-t/t_2} + \Delta\Psi_{III} \cdot e^{-t/t_3} + \Delta\Psi_{sys} \cdot e^{-t/t_{sys}} + c \qquad (2.5)$$

$\Delta\Psi(t)$: photovoltage at time t, $\Delta\Psi_i$: amplitude of the photovoltage generated at the i^{th} reaction step with $i \in \{I, II, III\}$, $\Delta\Psi_{sys}$: photovoltage amplitude associated to the passive system discharge components.
At pH values between 4.5 and 7.4 the dissipation of the photovoltage could be fitted with a single system time constant of 0.6 s to 1 s. At higher pH values a second system time constant that ranged between 50 ms and 90 ms had to be introduced into the signal decay. A possible explanation for the occurrence of another system discharge component might be a different degree of proteoliposome coverage of the BLM at the varying pH values. The variable access to the medium might result in different time constants.

2.9 Materials

Solutions, materials and instruments used were summarized in the following tables.

NG108-15 growth medium	450 ml DMEM, 45 ml FBS, 5 ml Penicillin/Streptomycin (final 100 Units/ml Penicillin, 0.1 mg/ml Streptomycin)
LB medium	0.5% Yeast Extract, 1% Tryptone, 1% NaCl pH 7.0
M9 mineral medium	33.7 mM Na_2HPO_4, 22 mM KH_2PO_4, 8.55 mM NaCl, 9.35 mM NH_4Cl, 0.4% glucose, 1 mM $MgSO_4$, 0.3 mM $CaCl_2$, 1 μg biotin, 1 μg thiamin, 13.4 mM EDTA, 3.1 mM $FeCl_3$-$6H_2O$, 0.62 mM $ZnCl_2$, 76 μM $CuCl_2$-$2H_2O$, 42 μM $CoCl_2$-$2H_2O$, 162 μM H_3BO_3, 8.1 μM $MnCl_2$-$4H_2O$ pH 7.5
Breaking buffer	50 mM Tris, 5 mM $MgCl_2$ pH 8 HCl
Buffer A	300 ml NaCl, 20 mM Hepes pH 7.4
Buffer B	300 ml NaCl, 20 mM Hepes, 500 mM imidazole pH 7.4
Impregnation solution	0.5% (w/v) DPPC in hexane
Membrane lipid solution	1.5% (w/v) DPPC, 1:60 octadecylamine/DPPC (w/w) in decane
pH titration solution	100 ml NaCl, 20 mM Hepes, 20 mM H_3BO_3, 20 mM $C_6H_8O_7$ pH 7.4

Table 2.1: List of media and solutions.

NsXeR					
Bath	140 mM	NaCl	**Pipette**	110 mM	NaCl
pH 7.4	2 mM	$MgCl_2$	**pH 7.4**	2 mM	$MgCl_2$
	2 mM	$CaCl_2$		10 mM	EGTA
	10 mM	Hepes		10 mM	Hepes
			Pipette	110 mM	NaCl
			pH 4.4/pH 5.4	2 mM	$MgCl_2$
				10 mM	EGTA
				10 mM	$C_6H_8O_7$
			Pipette	110 mM	NaCl
			pH 6.4	2 mM	$MgCl_2$
				10 mM	EGTA
				10 mM	MES
			Pipette	110 mM	NaCl
			pH 8.4	2 mM	$MgCl_2$
				10 mM	EGTA
				10 mM	Tris
KR2					
Bath*	X mM	NaCl	**Pipette***	X mM	NaCl
X mM NaCl	Y mM	NMG-Cl	**X mM NaCl**	Y mM	NMG-Cl
pH 7.4	2 mM	$MgCl_2$	**pH 6.0**	2 mM	$MgCl_2$
	2 mM	$CaCl_2$		10 mM	EGTA
	10 mM	Hepes		10 mM	MES
			Pipette*	140 mM	NMG-Cl
			0 mM NaCl	2 mM	$MgCl_2$
			pH 5.0	10 mM	EGTA
				10 mM	MES
			Pipette*	140 mM	NMG-Cl
			0 mM NaCl	2 mM	$MgCl_2$
			pH 7.4	10 mM	EGTA
				10 mM	Hepes
			Pipette	140 mM	NaCl
			140 mM NaCl	2 mM	$MgCl_2$
			pH 7.4	10 mM	EGTA
				10 mM	Hepes
tCXCR4/CatCh					
Bath	140 mM	NaCl	**Pipette**	140 mM	NaCl
pH 7.4	2 mM	$MgCl_2$	**Cell-attached**	2 mM	$MgCl_2$
	2 mM	$CaCl_2$	**pH 7.4**	2 mM	$CaCl_2$
	10 mM	Hepes		10 mM	Hepes
				50 nM	SDF1β
			Pipette	110 mM	NaCl
			Whole-cell	2 mM	$MgCl_2$
			pH 7.4	10 mM	EGTA
				10 mM	Hepes

Table 2.2: List of solutions used in patch clamp measurements with X = 140, 50, 25, 5, 1 or 0 and X + Y = 140. *Residual sodium concentration in 0 mM NaCl solutions: pipette $\approx$ 200 μM, bath $<$ 50 μM.

Chemicals	
Dulbecco's modified eagle's medium (DMEM)	Sigma-Aldrich
fetal bovine serum (FBS)	Sigma-Aldrich
Penicillin/Streptomycin	PanReac AppliChem
Lipofectamine 2000 or LTX	Thermo Fisher Scientific
All-*trans* retinal	Sigma-Aldrich
NaCl	Carl Roth
$MgCl_2$	Sigma-Aldrich
$CaCl_2$	Merck
NMG-Cl	Sigma-Aldrich
EGTA	Fluka
Hepes	Sigma-Aldrich
Tris	Sigma-Aldrich
MES	Carl Roth
H_3BO_3	Sigma-Aldrich
$C_6H_8O_7$	Sigma-Aldrich
NaOH	Carl Roth
HCl	Carl Roth
IPTG	Carl Roth
PMSF	BioChemica
DNase	F. Hoffmann-La Roche
DDM	GLYCON Biochemicals
Imidazole	Carl Roth
100600 E. coli Extract Polar	Avanti Polar Lipids
Sodium cholate hydrate	Sigma-Aldrich
1,2-diphytanoyl-sn-glycero-3-phosphocholine (DPPC)	Avanti Polar Lipids
Octadecylamine	Sigma-Aldrich
Hexane	Carl Roth
Decane	Carl Roth
Monensin	Sigma-Aldrich
Materials	
In-Fusion HD Cloning Kit	Clontech Laboratories
NG108-15 cells	ATCC
GB150F-8P/F glass capillaries	Science Products
HisTrap HF column	GE Healthcare
HiTrap Desalting column	GE Healthcare
Ultra-15 Centrifugal Filter Unit 50 kDa cutoff	Amicon
Bio-Beads SM-2 Resin	Bio-Rad

Table 2.3: List of chemicals and materials and their manufacturers.

NsXeR Patch clamp	
Axopatch 200B Amplifier	Axon Instruments
CV 203BU Headstage	Axon Instruments
Digidata 1440A	Axon Instruments
DPSS Laser MLL-FN-561	PhotonTec
LS2 2mm Laser Shutter	Vincent Associates
Opolette 355 Tunable Laser	Opotek
NsXeR BLM	
SR560 Low Noise Preamplifier	Stanford Research Systems
ADC-212 Digital Oscilloscope	Pico Technology
COMPex 102 Excimer Laser (Rhodamine 6G 556 nm)	Lambda Physik
KR2 Patch clamp	
Axopatch 200B Amplifier	Axon Instruments
CV 203BU Headstage	Axon Instruments
Digidata 1550	Axon Instruments
532 nm-DPSS Laser	Pusch OptoTech
Uniblitz LS6ZM2 Laser Shutter	Vincent Associates
COMPex 102 Excimer Laser (Coumarin 153 532 nm)	Lambda Physik
Tandem Patch clamp	
Axopatch 200B Amplifier	Axon Instruments
CV 203BU Headstage	Axon Instruments
DigiData 1322A	Axon Instruments
473 nm-DPSS Laser	Pusch OptoTech
LS2 2mm Laser Shutter	Vincent Associates
RC6 Waterbath	Lauda
Pump	Rietschle Thomas
Software	
Axon pCLAMP 10.4	Molecular Devices
PicoScope6	Pico Technology
Origin 2018b	OriginLab
Other	
Axiovert Microscopes	Zeiss
P-1000 Micropipette Puller	Sutter Instruments
Cary 50 Bio UV-Vis Spectrophotometer	Varian
AAnalyst 200 Atomic Absorption Spectrometer	PerkinElmer
Lab850 pH-meter	SI Analytics
ÄKTApurifier 100	GE Healthcare
LSM 700 Laser Scanning Confocal Microscope	Carl Zeiss

Table 2.4: List of Instruments and Software.

3 Results Part I: Characterization of NsXeR

3.1 pH Dependence of Absorption Spectra

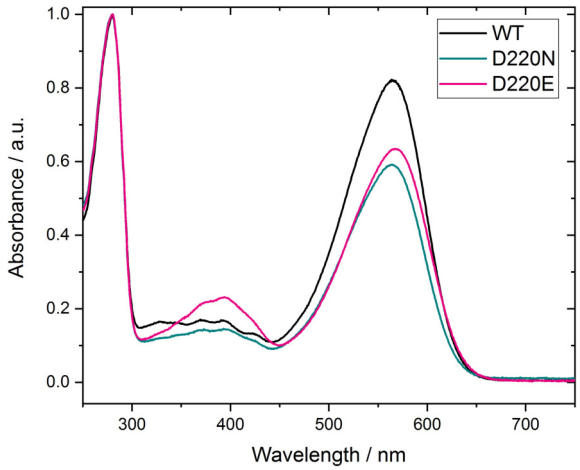

Figure 3.1: UV-Vis absorption spectra of NsXeR wild type and mutants D220N and D220E. The protein was solubilized in 0.05% DDM at pH 7.2 and the spectra were normalized to the absorbance at 280 nm.

An important feature in the proton pump mechanism of microbial rhodopsins is the protonation and deprotonation of the retinal Schiff base and different residues that change their pK_a in the course of the photocycle [51].
In order to investigate the retinal Schiff base pK_a of the wild type (WT) and the influence of the mutations D220E and D220N, UV-Vis spectroscopy measurements were performed. The purified protein was solubilized in 0.05% DDM at pH 7.2 and absorption spectra were taken at different pH values. At pH 7.2 the wild type exhibits a maximal absorbance at 565 nm (Figure 3.1 and Table 3.1) which is in agreement with previous reports [32]. The D220N mutant has no influence on the absorbance maximum, but in the case of D220E it is slightly but significantly red-shifted to a wavelength of 568 nm (with $p < 10^{-3}$). Since the neutralization of the putative acceptor group in D220N has no influence on the maximal absorbance wavelength, Asp220 does not seem to be a part of the counter ion complex to the protonated Schiff base in NsXeR. This result is in line with the structural data and the relatively large distance of 12 Å between Asp220 and the Schiff base [32].

	λ_{max} at pH 7.2 / nm	Schiff base pK_a	WT	D220N	n
WT	565.56 ± 0.18	9.56 ± 0.06			3
D220N	565.02 ± 0.35	9.84 ± 0.19	$p < 0.01$		4
D220E	568.13 ± 0.70	8.43 ± 0.12	$p < 10^{-9}$	$p < 10^{-11}$	3

Table 3.1: Absorption maximum and Schiff base pK_a of NsXeR WT, D220N and D220E in solubilized form. Retinal SB pK_a values are significantly different, p values are given in columns 4 and 5. Results are given as mean ± SD.

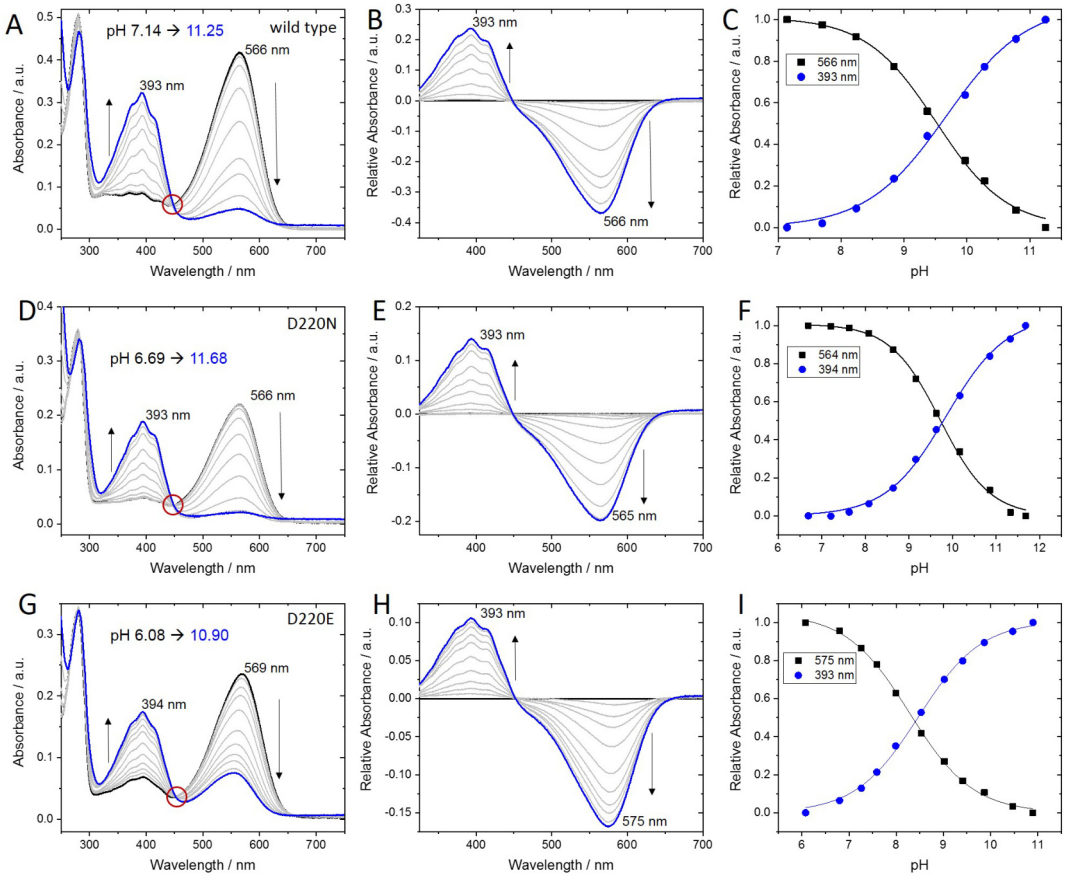

Figure 3.2: pH titration experiments in UV-Vis spectroscopy of NsXeR WT (A-C), D220N (D-F) and D220E (G-I). (A, D and G) Changes of UV-Vis spectra induced by pH titrations. The red circle marks an isosbestic point. (B, E and H) Difference spectra were calculated by subtracting the spectrum at the initial pH from each spectrum. (C, F and I) pH dependence of the relative absorbance changes of the peak wavelengths from B, E and H. The data was fitted with a logistic function $\Delta Abs = A/(1 + 10^{n(pK_a - pH)})$ (n<1) and the apparent pK_a of the retinal Schiff base for the WT and mutants D220E and D220N was determined.

The pH dependence of the spectra was investigated by titration experiments that were summarized in Figure 3.2. The absolute and relative absorption spectra show major changes for the WT and both mutants. The main absorption bands at neutral pH are reduced upon alkalization and an increase of absorbance can be observed around 390 nm. The fine structure that appears in the band around 390 nm is characteristic for the MI intermediate in the NsXeR WT photocycle [32]. The spectral changes indicate the titration of the retinal Schiff base from a protonated to a deprotonated species which is also confirmed by the appearance of an isosbestic point (447 nm for the WT). The relative absorbance at the wavelengths of maximal change was plotted against the pH and the data was fitted with a logistic function in order to determine the apparent pK_a values (summarized in Table 3.1). The reversibility of the spectral changes was verified by titrating back to the original pH which lead to a decrease of the absorbance around 390 nm and an increase of the original main absorption band.
The NsXeR wild type has a Schiff base pK_a of 9.56 which is slightly lower than what was reported for BR ($\sim$ 13.3 [119]). For D220N the pK_a is significantly higher, but only by a ΔpH of 0.28. The neutralization of the Asp220 residue does not seem to have a strong influence on the electronic environment of the Schiff base cavity. The D220E mutation on the other hand causes a significant drop of the pK_a to 8.43. The increased absorbance around 390 nm for D220E compared to the wild type can already be observed at pH 7.2 (3.1). Asp220 is located at a distance of 12 Å away from the Schiff base and they are connected via a water molecule [32]. Compared to aspartate glutamate has a longer side chain by one methylene moiety. Also the average proton affinity for glutamate is higher compared to aspartate (pK_a of glutamates 4.1 versus $\leq$ 3.4 for aspartates [120]). A tentative explanation for the Schiff base pK_a drop in D220E might be a long range change of interactions close to the retinal Schiff base caused by the mutation to glutamate.

Taking a closer look at the absorption band of the protonated Schiff base of the mutant D220E in Figure 3.2 G and H, the pH dependence of the absorption maximum (568 nm at pH 7.2) is striking. To visualize the pH dependence the maximal wavelength was plotted against the pH values and depicted in Figure 3.3. For the NsXeR WT a pH independence was reported for the solubilized protein between pH 4.5 and 9.0 [32]. The results in Figure 3.3 A show a slightly different behavior. While the absorption maximum is indeed pH independent at higher values, it changes reproducibly in the region between pH 4 and 8 (green diamonds). Fitting the data with a logistic function yielded an apparent pK_a value of 5.48 ± 0.10 ($n = 4$). The red-shift of the maximum at high proton concentrations suggests the protonation of a residue in the environment of the retinal Schiff base. At the same time the interaction seems to be rather weak as the amplitude of the change is only about 2.5 nm.

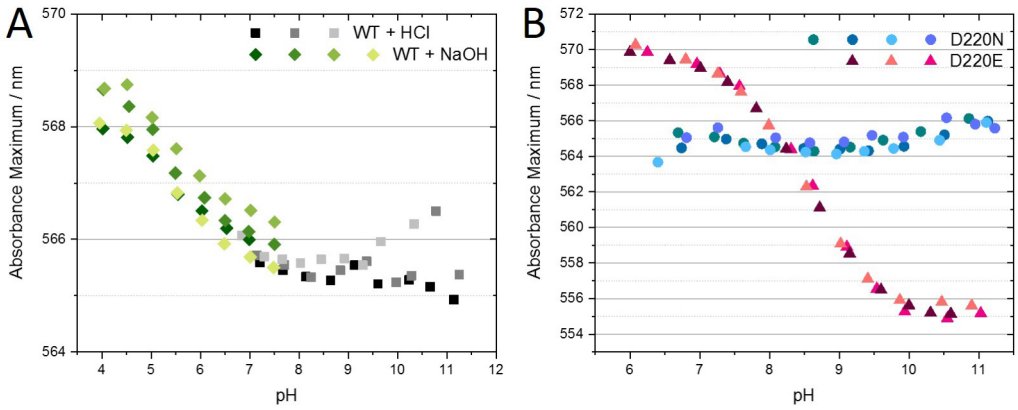

Figure 3.3: pH dependence of the absorption maxima of the protonated Schiff base band for NsXeR WT (A) and the mutants D220E and D220N (B). Titrations were started at neutral pH and continued to acidic or alkaline pH values by adding 1 N HCl or NaOH, respectively.

In Figure 3.3 B the mutations are shown. While the neutralization of Asp220 to Asn shows no pH dependent changes of the absorption maximum, the mutation to Glu has a striking effect, as was mentioned before. The absorption wavelength of the protonated Schiff base shows a blue shift by about 15 nm upon reduction of the proton concentration from pH 6 to 11. The analysis with a logistic fit function resulted in an apparent pK_a of 8.51 ± 0.09 ($n = 3$).

3.2 Inward Pump Currents and Intracellular pH Dependence

In order to directly investigate the proton pump vectoriality and the dependence on the intracellular pH, the patch clamp technique was used. The heterologous expression of NsXeR in NG108-15 cells ensures the right-side out orientation of the proteins in the cell membrane and the whole-cell configuration allows for the control of the intra- and extracellular (IC and EC) solutions.

In continuous illumination measurements NsXeR shows a fast inward transient that decays into an inward steady-state current which in turn stays stable until the end of the illumination. A typical current measurement at different membrane potentials is illustrated in Figure 3.4 A. The steady-state currents decay back to the dark currents when the illumination ends. NsXeR causes inward currents at all measured membrane potentials whereby the current decreases at more positive ones. This would be expected, because the pump is working against a higher electrochemical load.

The voltage dependence of the steady-state current densities can be taken from Figure 3.4 B.

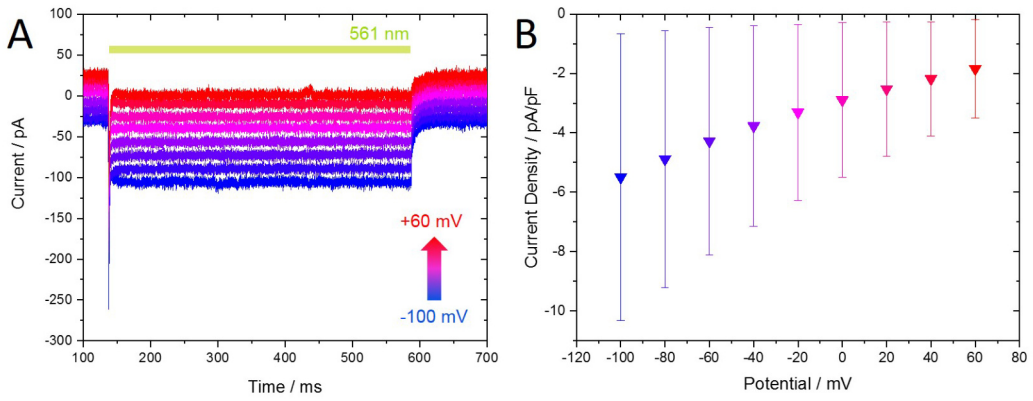

Figure 3.4: Patch clamp data from continuous illumination measurements at IC = EC = pH 7.4 on NsXeR expressing NG108-15 cells. (A) Current traces at different membrane potentials with Δ 20 mV. The green bar indicates the illumination period with 561 nm light. (B) The steady-state currents were divided by the cell capacitance and the current density was plotted against the applied membrane potential. The mean current densities of n = 9 cells were evaluated. The measurements were performed by M. Breyer under my supervision.

The respective dark currents were subtracted from the steady-state currents and the differences in cell size were taken into account by dividing the current by the cell capacitance, which is approximately proportional to the cell surface. Despite this adjustment the standard deviations are quite big, which can be explained by the rather strong variations in expression levels for the single cells. Nevertheless, in agreement with published data [32] a more or less linear voltage-dependence of the currents was observed.

The influence of the intracellular pH on the steady-state currents and the pump kinetics was investigated by measurements at different pH gradients and by the analysis of the steady-state off-kinetics. While the IC pH was varied the EC pH was kept at 7.4. Similar to the data in Figure 3.4 B, the standard deviations of the current densities at different pH gradients were quite big (not shown). No significant differences could be found which might be caused by an IC pH independence or the high expression variations. For a better comparison the steady-state currents were normalized to the current at 0 mV and their absolute values were plotted versus the membrane potential (Figure 3.5 A). The data was linearly fitted and the apparent potentials of zero current E_0 were extrapolated. The results are summarized in Table 3.2. With a single exception of a significant difference between the values at pH 4.4 and 8.4 ($p < 0.009$), the determined E_0's show no significant differences.

	pH 4.4	pH 5.4	pH 6.4	pH 7.4	pH 8.4
E_0 / mV	103 ± 13	113 ± 10	117 ± 13	118 ± 6	135 ± 14

Table 3.2: Apparent potentials of zero current E_0 extrapolated from linear fits of the current versus voltage plots in Figure 3.5 A. The only significant difference could be found between the values at pH 4.4 and 8.4 with $p < 0.009$.

The decay kinetics of the steady-state currents were analyzed with a biexponential fit. The first rate constant k_1 of about 1000 Hz is influenced by the shutter closing time and cannot be resolved reliably. Regarding the second rate constant k_2, the potential and pH dependencies were analyzed and can be seen in Figure 3.5 B. Similar to the steady-state currents in Figure 3.5 A, k_2 is linearly dependent on the membrane potential with a decrease of the turnover at more positive membrane potentials.

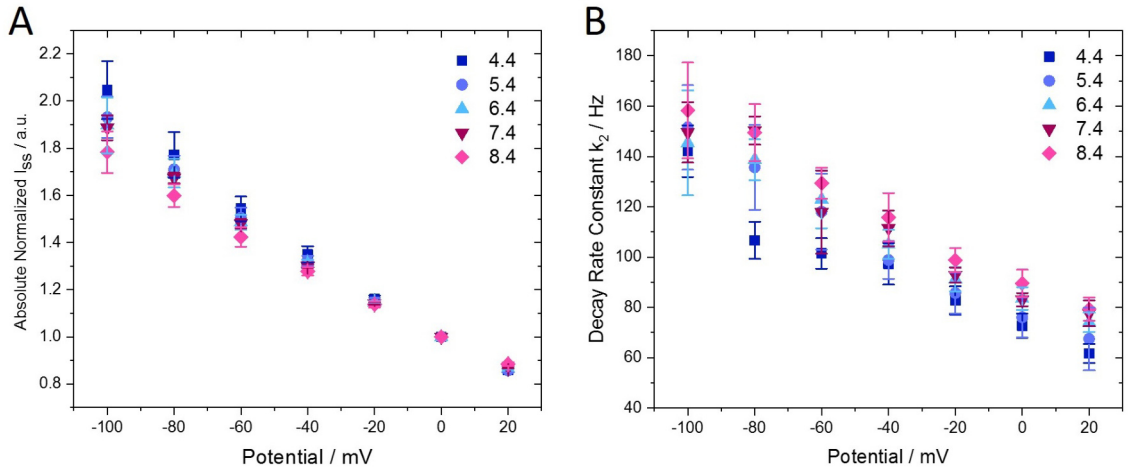

Figure 3.5: Influence of the intracellular pH on the membrane potential dependence of the steady-state currents and their off-kinetics. Measurements were performed at an EC pH of 7.4 and varying IC pH values. (A) The steady-state currents were normalized to the current at 0 mV and their absolute values were plotted versus the membrane potential. (B) The slow decay rate constant k_2 was determined by fitting the steady-state current decay with an exponential fit function $I(t) = I_1 \cdot e^{-k_1 \cdot t} + I_2 \cdot e^{-k_2 \cdot t} + c$. The means of n = 4 (pH 4.4), 4 (pH 5.4), 4 (pH 6.4), 3 (pH 7.4) and 5 (pH 8.4) cells were evaluated. The measurements were performed by M. Breyer under my supervision.

The determined k_2 values do not show a strong variation in dependence of the intracellular pH. Significance tests confirmed that there is no difference between intracellular pH 4.4, 5.4, 6.4 and 7.4 in the potential range between -100 and 0 mV. The only exception is the outlier at the IC pH 4.4 and -80 mV which is significantly different to every other value. The results at IC pH 8.4 diverge from the ones at pH 4.4 (from -80 mV to 20 mV) and pH 5.4 (0 mV and 20 mV) at the $\alpha < 0.05$ level.

As mentioned earlier, the steady-state currents I_{ss} (Figure 3.5 A) as well as the decay rate constants k_2 (Figure 3.5 B) show a linear voltage dependence. Comparing the currents at -100 mV and 20 mV, a current decrease by a factor of 0.46 (pH 7.4) can be observed. k_2 decreases by a factor of 0.52 (pH 7.4) in the same range. For a more thorough analysis the decay rate constants were also normalized to the value at 0 mV and linear fits were performed to determine the slopes. The slopes of the normalized steady-state currents and rate constants are the same at every IC pH (at the $\alpha < 0.05$ level). In addition the slopes of the normalized rates are equal at every IC pH. Hence, the lower I_{ss} can be explained by a lower turnover of the pump.

The inward pump currents of NsXeR in response to a ns light pulse illumination were also investigated. In contrast to the continuous illumination measurements, the pumps are not repeatedly excited but undergo a single pump cycle in which they are synchronized.

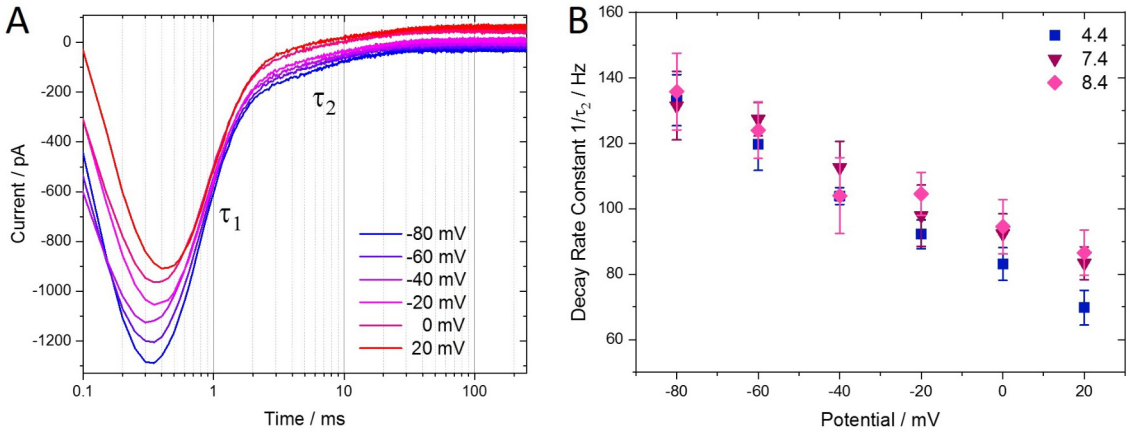

Figure 3.6: Patch clamp data from ns light pulse illumination measurements at 561 nm on NsXeR expressing NG108-15 cells. (A) Inward transient pump currents at membrane potentials between -80 mV and 20 mV. The time axis was shifted in a way that the light pulse occurs at the time 0. (B) Membrane potential dependence of the decay rate constant $1/\tau_2$ at different intracellular pH values (EC pH 7.4). $1/\tau_2$ was determined by fitting the transients decay with a biexponential fit function $I(t) = I_1 \cdot e^{-t/\tau_1} + I_2 \cdot e^{-t/\tau_2} + c$. The means of n = 4 (pH 4.4), 5 (pH 7.4) and 3 (pH 8.4) cells were evaluated. The measurements were performed by M. Breyer under my supervision.

A typical example for the resulting current transients is illustrated in Figure 3.6 A. The peak decay kinetics were analyzed using biexponential fits. Although the time resolution was not impaired by a mechanical shutter, the rate constant $1/\tau_1$ could not be reliably resolved due to the low pass filter behavior of the access resistance R_a and the cell capacitance C_m in most measurements. An access resistance of 10 MΩ and a cell capacitance of 15 pF would lead to a RC filter with a corner frequency of $f_c = 1/2\pi R_a C_m = 1.1$ kHz.

At a membrane potential of 0 mV $1/\tau_1$ was 2.2 kHz at pH 7.4 for two cells. $1/\tau_2$ on the other hand could be well resolved and was plotted against the applied membrane potential in Figure 3.6 B. Again, the kinetics show a linear potential dependence and are not influenced by intracellular pH changes. Only the outlier at IC pH 4.4 is significantly different at 20 mV. The slow decay kinetics from ns light pulse and continuous illumination measurements (Figure 3.5 B) are in the same range (k_2 = 83 Hz and $1/\tau_2$ = 92 Hz at EC = IC = pH 7.4 and 0 mV). The charge Q_2, that was transported in the transition step described by $1/\tau_2$, was calculated according to $Q_2 = I_2 \cdot \tau_2$ and normalized to the charge at 0 mV. It was found that the amount of transported charge Q_2 is independent of the applied membrane potential (Figure 3.7).

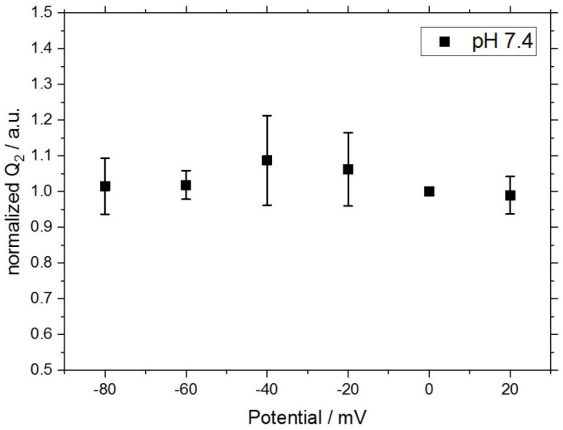

Figure 3.7: Charge Q_2 that was transported in the transition step described by $1/\tau_2$ from nanosecond flash illumination experiments at IC = EC = pH 7.4. It was calculated according to $Q_2 = I_2 \cdot \tau_2$ and normalized to the value at 0 mV. The measurements were performed by M. Breyer under my supervision.

The results indicate that the steady-state currents as well as the slow decay kinetics are independent of the intracellular pH. Furthermore, the voltage dependence of the pump currents correlates perfectly with the voltage dependence of the slow decay rate constant k_2.

3.3 Mutational Studies on Putative Transport Involved Residues

The influence and importance of different residues in relation to the transport mechanism of NsXeR can be investigated by selective mutational studies. From the published structural data on NsXeR several residues were suggested to be involved in the protonation and deprotonation processes. In the proton release region the Asp220-His48 pair was suggested to act as the proton acceptor. A second pair Glu228-His94 is located at the very interface to the cytoplasm. It is suggested to serve as a proton release group. An important residue

in the proton uptake region is the putative donor and counter ion Asp76 [32].
For the following section site-directed mutagenesis was performed on the charged residues mentioned above. Transiently transfected NG108-15 cells were used for patch clamp measurements with continuous illumination at 561 nm. Due to the cleavage of the fluorescent protein from NsXeR the membrane localization cannot be assessed.

3.3.1 Glu228 of the Putative Release Group

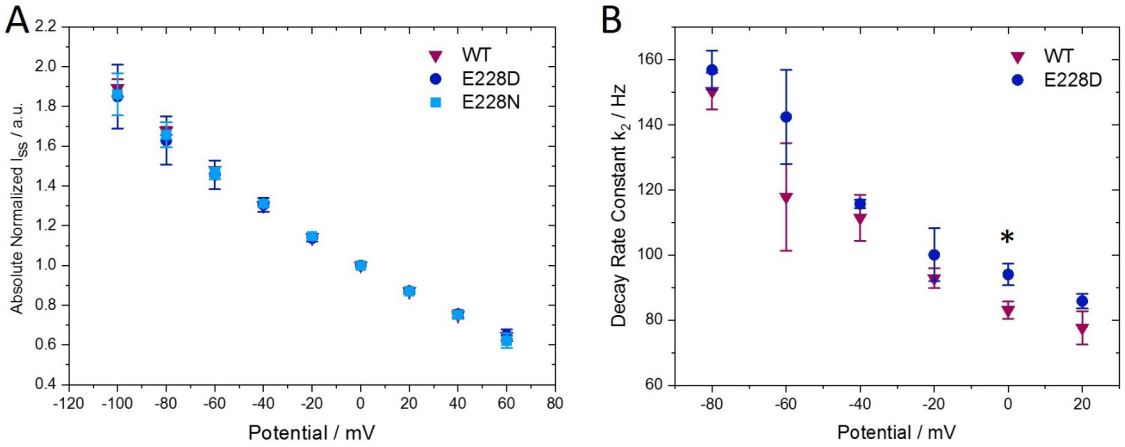

Figure 3.8: Patch clamp measurements on NsXeR E228D and E228N. Bath and pipette solutions were adjusted to pH 7.4 and the cells were continuously illuminated with 561 nm. (A) The steady-state currents were normalized to the value at 0 mV and their absolute values were plotted versus the applied membrane potential. The means of n = 3 (WT), 8 (E228D) and 4 (E228N) cells were evaluated. (B) The slow decay rate constant k_2 was determined as described earlier (Figure 3.5). The means of n = 3 (WT) and 3 (E228D) cells were evaluated. * marks a significant difference with $p < 0.011$. The measurements were performed by M. Breyer under my supervision.

The role of Glu228, which is part of a putative proton release group at the intracellular side, was studied by replacing it with a shorter but charged side chain in NsXeR E228D and a non charged residue in NsXeR E228N. The mutants showed similar steady-state current densities compared to the WT (-2.9 ± 2.6 pA/pF (WT, n = 9), -2.0 ± 2.1 pA/pF (E228D, n = 17) and -1.7 ± 1.2 pA/pF (E228N, n = 5)). Again, the currents were normalized to 0 mV and their absolute values were plotted in Figure 3.8 A. The linear dependence on the applied membrane potential is congruent with the wild type currents for both mutants. The decay kinetics of the steady-state currents were evaluated for a possible increase or decrease of the turnover rate due to the mutation of Glu228. The plot of the decay rate constant k_2 in Figure 3.8 B shows that no influence could be found, viewing the difference at 0 mV as an outlier.

Since the mutations of Glu228 did not have an effect on the decay kinetics, the Glu228-His94 pair is either not crucial for the proton transport or the proton release under the present conditions is not rate limiting. Further investigations for example at different IC pH values could give additional inside to the role of the Glu228-His94 pair.

3.3.2 Asp220 of the Putative Proton Acceptor Pair

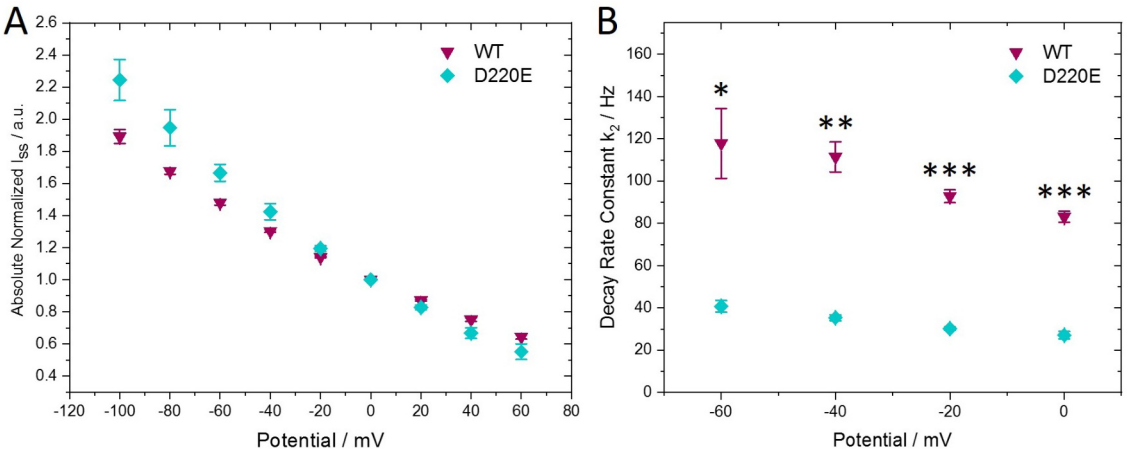

Figure 3.9: Patch clamp measurements on NsXeR D220E. Bath and pipette solutions were adjusted to pH 7.4 and the cells were continuously illuminated with 561 nm. (A) The steady-state currents were normalized to the value at 0 mV and their absolute values were plotted versus the applied membrane potential. The means of n = 3 (WT) and 10 (D220E) cells were evaluated. (B) The slow decay rate constant k_2 was determined as described earlier (3.5). The means of n = 3 (WT) and 3 (D220E) cells were evaluated. The differences in k_2 between the wild type and D220E were significant with: * $p < 0.002$, ** $p < 10^{-4}$ and *** $p < 10^{-5}$. The measurements were performed by M. Breyer under my supervision.

The important position of the proton acceptor was suggested to be taken up by the Asp220-His48 pair in NsXeR. Indeed, mutations of the Asp220 residue caused changes compared to the wild type. The D220N mutant that abolishes the carboxylic acid group did not show any measurable photocurrents upon illumination. The loss of pump activity in this mutant is in agreement with assays that monitored light-induced pH changes of *E. coli* suspensions [32].

The conservative D220E mutation was fully functional in the same assays. In line with these findings, inward pump currents were measured with a current density of -1.2 ± 1.0 pA/pF at 0 mV (n = 14). Comparing the current densities of D220E with the wild type, no significant differences could be found. But taking a closer look at the normalized steady-state currents in Figure 3.9 A, a difference in the potential dependence

becomes obvious. The slopes of the linear relations are different with $p < 10^{-4}$ which underlines that the D220E pump currents are more sensitive to the applied membrane potential. The influence of D220E on the kinetics of the steady-state current decay is shown in Figure 3.9 B. The rate constant k_2 was reduced compared to the wild type which means that the pump cycle was slowed down. At 0 mV, the corresponding turnover rate was reduced by a factor of 3 (down to 27.1 ± 1.8 Hz) compared to the wild type (83.1 ± 2.6 Hz). The results show the importance of a charged residue at position 220 for the proton transport in NsXeR. Assuming that Asp220 indeed is the proton acceptor, the loss of function in D220N could be simply explained by the inability of the protonated retinal Schiff base to transfer its proton to another residue. D220E on the other hand is still able to accept a proton and, therefore, does not impair the pump function. Nevertheless, the pump cycle is slowed down for D220E which suggests that the wild type with Asp220 is more effective and optimized for proton transport.

3.3.3 Asp76 the Putative Proton Donor

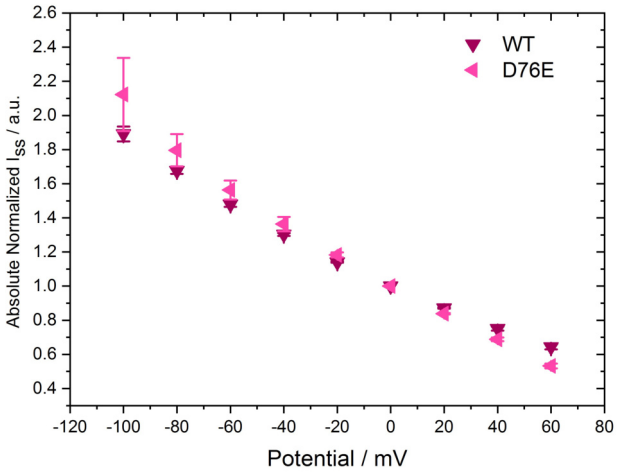

Figure 3.10: Normalized steady-state photocurrents from continuous illumination patch clamp measurements. Bath and pipette solutions were adjusted to pH 7.4. Cells were illuminated at 561 nm. Currents were normalized to the value at 0 mV. The means of n = 3 (WT) and 5 (D76E) cells were evaluated. The measurements were performed by M. Breyer under my supervision.

Asp76 is located at the position corresponding to the acceptor Asp85 in BR and was suggested to act as a proton donor in NsXeR [32]. Mutations of this residue did not yield correctly folded proteins as reported by Shevchenko *et al.* [32]. Indeed, NG108-15 cells transfected with the NsXeR D76N gene did not show any photocurrents upon illumination. Also adding 20 mM of sodium azide could not establish light induced pump currents. From the measurements it cannot be decided if the protein is not folded or not active.

The transfection of cells with the D76E gene lead to inward pump currents upon light-activation, despite the observation of non colored cells for the mutant in previous studies [32]. Due to inconsistencies in reproducibility of the photocurrent signals the results on this mutant are treated as preliminary data that require further investigation. The normalized steady-state photocurrents of D76E are shown in Figure 3.10. Similar to the wild type the photocurrents are linearly dependent on the applied membrane potential. The analysis of kinetic parameters showed a discrepancy between measurements under continuous and nanosecond flash illumination. While the slow decay of steady-state currents under continuous illumination was in the range of the wild type with $1/k_2 = 11.4 \pm 2.7$ ms (pH 7.4, 0 mV, n = 3), the second time constant from flash illumination measurements was significantly faster with $\tau_2 = 2.8 \pm 0.3$ ms (pH 7.4, 0 mV, n = 8).

3.4 Blue-Light-Effect

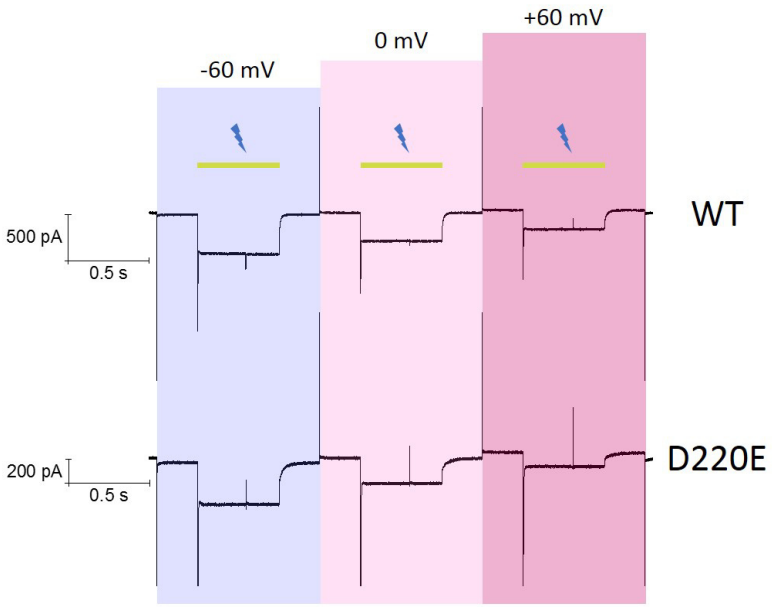

Figure 3.11: Blue-light-effect in NsXeR wild type and mutant D220E. The raw patch clamp data traces were measured at pH 7.4 and three membrane potentials were applied as indicated. Inward steady-state currents were evoked by continuous 561 nm illumination (green bar). Additional nanosecond light pulses at 355 nm (blue flash symbols) caused transients of varying vectoriality.

The blue-light-effect observed in BR was described in Section 1.5. The effect of blue light illumination on NsXeR molecules in the M intermediate was investigated by patch clamp measurements on NsXeR expressing NG108-15 cells with continuous 561 nm illumination

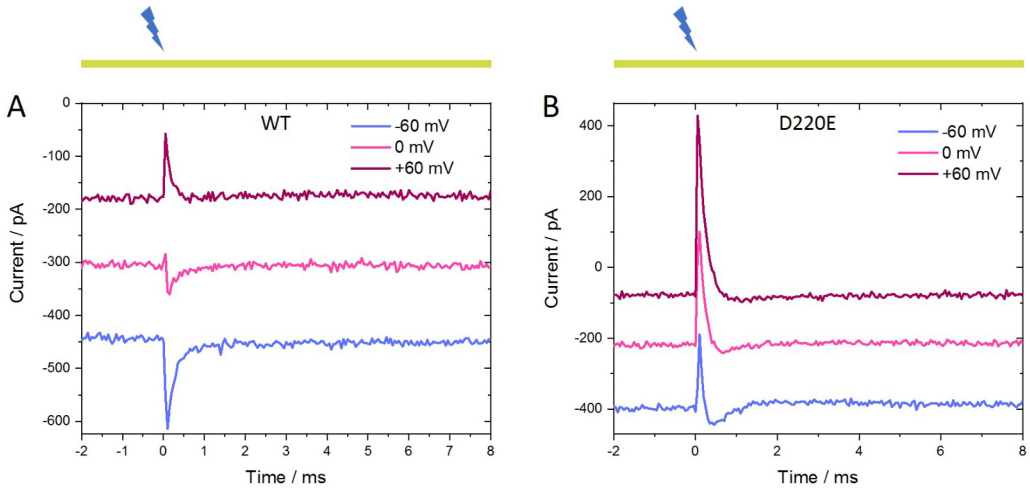

Figure 3.12: Blue light induced current transients in NsXeR wild type (A) and mutant D220E (B). The blue light induced current transients with 561 nm background illumination from Figure 3.11 are displayed larger and the time axis is shifted for a better comparison. Green bars and blue flash symbols indicate the illumination with continuous 561 nm light and 355 nm light pulses, respectively.

and additional nanosecond light pulses at 355 nm. Different membrane potentials were applied during the measurement protocol which can be seen in Figure 3.11. The blue light causes fast transients of varying vectoriality for the wild type and the D220E mutant.
A closer look on the wild type measurements can be taken in Figure 3.12 A. At -60 mV the blue light causes a fast negative current transient which adds onto the inwardly directed pump current that is induced by the green background illumination. The transient is diminished at 0 mV and even changes its vectoriality at a positive membrane potential of 60 mV. The direction of the blue light induced currents in NsXeR wild type strongly depends on the applied membrane potential.

A different behavior was observed looking at the D220E mutant in analogous measurements (Figure 3.12 B). At all applied membrane potentials the inward pump currents are quenched by outward current transients. This suggests that the regular pump cycle is short-circuited by a reprotonation of the retinal SB from the release side. At -60 mV a small overshoot appears that might be explained by quenched molecules reentering the pump cycle (similar to BR [76]). In contrast to the wild type, only the amplitudes and not the vectoriality of the blue light induced current transients are dependent on the membrane potential in D220E.

A blue light effect with a voltage dependent vectoriality of the transients is a new situation compared to the quenching effect in BR. The results indicate that the accessibility

of the retinal SB to a reprotonation from the intracellular or extracellular side is influenced by the applied membrane potential. Also the presence of different blue-light absorbing intermediates can be concluded.

3.5 pH Dependence of Blue Light Induced Current Transients

The measurements described in section 3.4 were performed with continuous 561 nm illumination which leads to an accumulation of the blue absorbing M intermediates in the NsXeR molecules and a depopulation of the ground state. Leaving the background light away, only the ground state is populated and excitable by the 355 nm light pulses. In Figure 3.13 A the wild type expressing cells were measured at pH 7.4 and current transients of inward proton transport can be observed at the applied membrane potentials that are similar to the transient currents evoked by 561 nm light pulses in Figure 3.6. Fitting the relaxation of the peak currents with a biexponential function gave a slow time constant $\tau_{2,355}$ of 12.2 ± 0.3 ms (0 mV, n = 4) which is in agreement with the analogous time constant $\tau_{2,561} = 10.9 \pm 0.7$ (0 mV, n = 5) from 561 nm flash measurements (Figure 3.6 B). Therefore, it is suggested that the transients in Figure 3.13 A are caused by residual blue light absorption of the NsXeR ground state resulting in a regular pump cycle which was also concluded for BR in comparable measurements [75, 76].
At pH 7.4 the behavior of the D220E mutant is quite similar (Figure 3.13 B). The transients of inwardly directed currents relax with a slow decay time constant $\tau_{2,355}$ of 43.7 ± 5.3 ms (0 mV, n = 3) which is a factor of ~ 3.6 slower compared to the wild type. Since a similar value was determined in 561 nm illumination measurements (slowed down by a factor of 3, Figure 3.9) it is concluded that the transients in Figure 3.13 B arise from residual blue light absorption of the ground state.

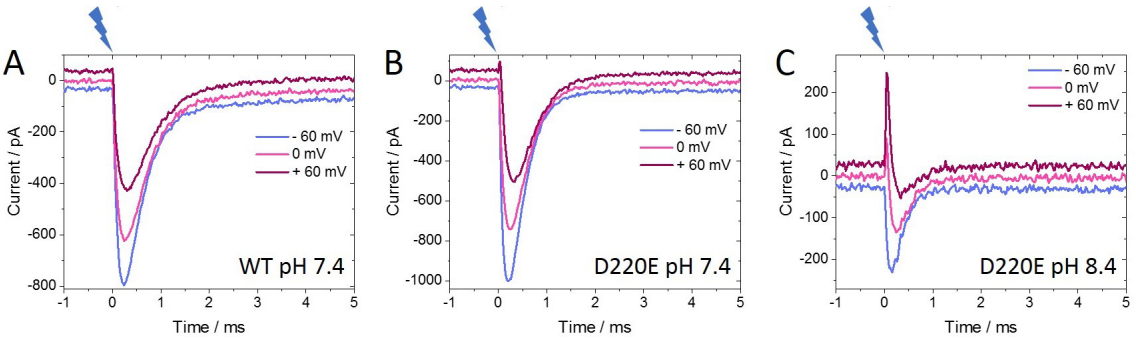

Figure 3.13: NsXeR transient photocurrents induced by 355 nm light pulses. Patch clamp measurements on NsXeR wild type (A) and mutant D220E (B and C) expressing NG108-15 cells without background illumination. The pH was set to 7.4 (A and B) or 8.4 (C) without a proton gradient between the intra- and extracellular solution.

The measurements were repeated at a pH of 8.4 which did not lead to a changed behavior for the wild type. In contrast to that, the blue light induced transients in D220E gained a component of fast outward directed currents that are also dependent on the applied membrane potential (see Figure 3.13 C). At pH 8.4 the blue light pulses seem to excite a population of D220E molecules that do not perform the regular pump cycle. Since the pK_a of the retinal SB of D220E was reduced to 8.43 in detergent (see section 3.1) this population might well be a blue absorbing ground state species with a deprotonated SB that could already be observed in the absorbance spectra of D220E at pH 7.2 (Figure 3.1). This blue absorbing ground state seems to be sensitive to the membrane potential. Patch clamp measurements at a higher pH were not performed due to changes in the cell properties that would make the results questionable.

3.6 pH Dependent Photovoltage of NsXeR Proteoliposomes

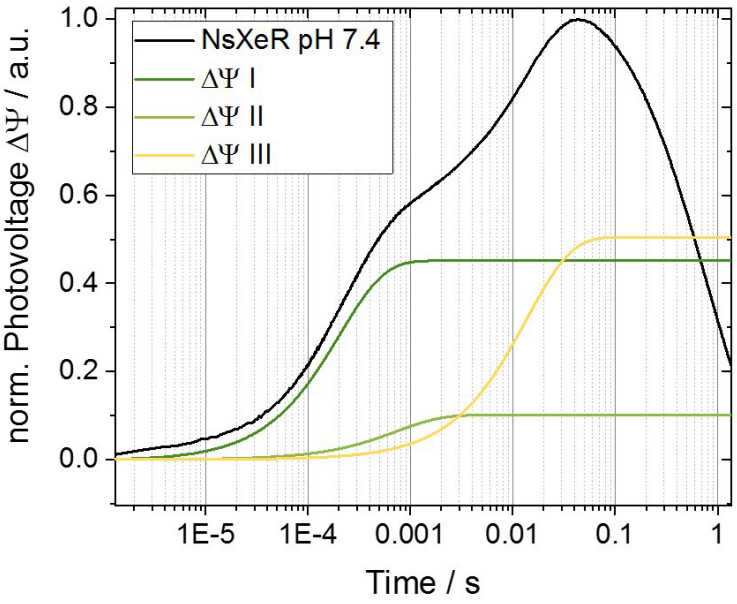

Figure 3.14: Photovoltage $\Delta\Psi$ of NsXeR proteoliposomes. NsXeR proteoliposomes attached to a black lipid membrane were illuminated with a nanosecond light pulse at 556 nm. Measurements were performed at pH 7.4 in presence of 5 μM monensin. The signal was normalized to the maximum (black line) and the fitted with an exponential function (Equation (2.5)). The three resulting components in the signal build-up are indicated by colored lines.

For a more detailed investigation of the electrogenic processes the purified NsXeR wild type protein was reconstituted into proteoliposomes which were attached to a black lipid

membrane. A typical voltage signal that was caused by the illumination of the proteoliposomes can be seen in Figure 3.14. The photovoltages are directly proportional to the charge displacement and allow for a better time-resolution than the current measurements in the patch clamp experiments [118]. From the sign of the voltage signal it was concluded that the reconstitution yielded a predominant amount of inside-out oriented molecules. To abolish possible proton gradients between interior and exterior of the vesicles, 5 μM monensin was added to the medium. As can be seen in Figure 3.14 the photovoltage first builds-up as a response to the transported charge by NsXeR, reaches a maximum and then decays again as a consequence of the passive discharge components of the system [118]. From the kinetic analysis three successive steps in the signal generation were identified with time constants of approximately 220 μs, 0.9 ms and 15 ms whose contributions accounted for 42%, 10% and 48% of the overall charge displacement, respectively. The decay of the photovoltage signal took place with a time constant of 0.6 s.

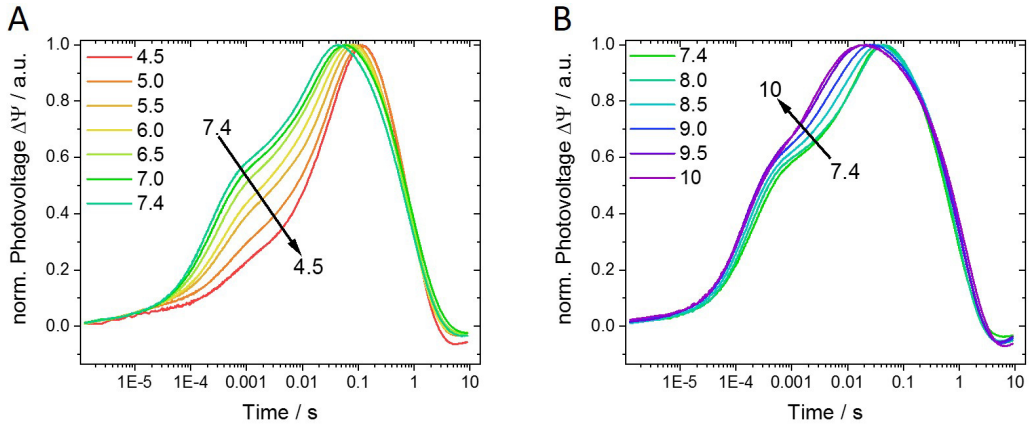

Figure 3.15: pH dependence of NsXeR photovoltage signal. The medium in BLM experiments was either acidified (A) or alkalified (B) starting at pH 7.4. The signals in A and B were measured on a single membrane, respectively. The photovoltages were normalized to the maximum.

Titration experiments were carried out in order to investigate the pH dependence of the photovoltage signal. All titrations started at a pH of 7.4 and the medium was either acidified or alkalified which lead to changed voltage signals that can be seen in Figure 3.15 A and B, respectively. In more acidic medium a delayed build-up of the voltage is observable and the maximum is reached at a later time. The opposite is true for the photovoltages measured at more alkaline pH values where the build-up is faster and the maximum reached earlier. The voltage signal relaxed with a slow time constant of 0.6 s to 1 s. A second decay time constant between 50 ms and 90 ms had to be introduced for pH values of 8.0 and higher. The relaxation with an additional time constant might be explained by different degrees of proteoliposome coverage of the membrane.

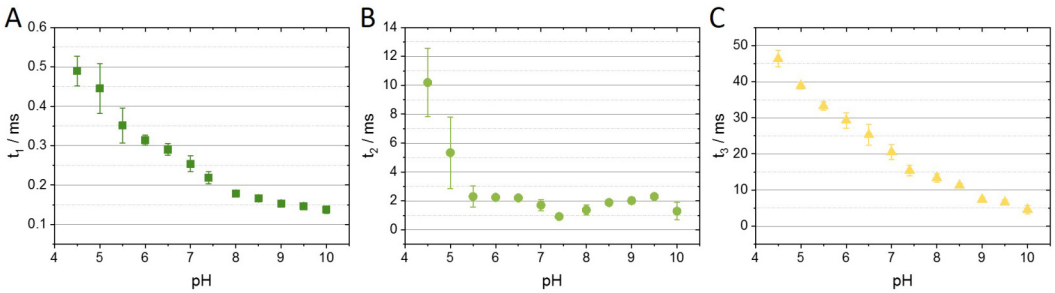

Figure 3.16: pH dependence of NsXeR photovoltage generation kinetics. The medium in BLM experiments was either acidified or alkalified and the photovoltage signals were exponentially fitted. The results are shown as mean ± SD of n = 3 membranes.

In Figure 3.16 the pH dependence of the three step photovoltage generation is summarized. With increasing pH values the time constants t_1 and t_3 (Figure 3.16 A and C) show a distinct pH dependence where both steps are accelerated in an almost linear fashion. t_3, which describes the slowest contributing step, is accelerated from 46.4 ms to 4.6 ms between pH 4.5 and 10 while t_1 is accelerated from 0.480 ms to 0.138 ms in the same pH range. The second time constant t_2 on the contrary is pH independent at values between 5.5 and 10. A deceleration of t_2 can be observed at pH 4.5 and 5.0.

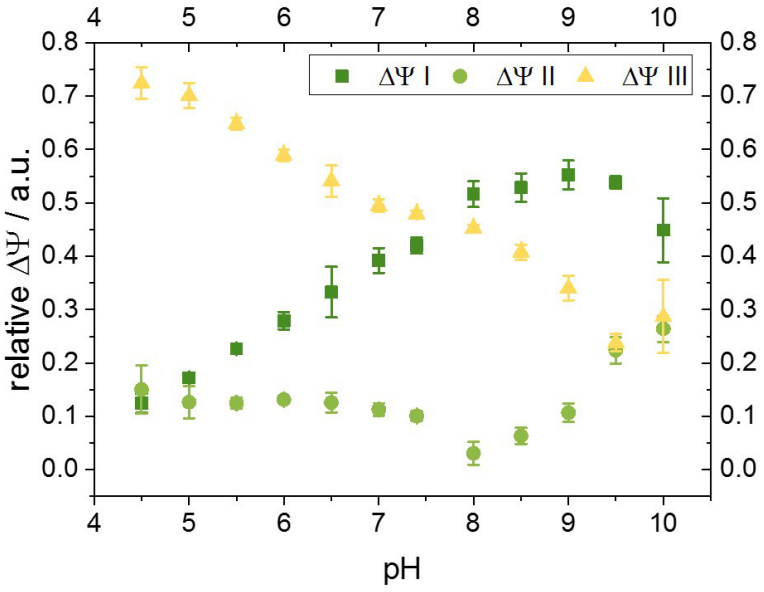

Figure 3.17: pH dependence of relative contributions in NsXeR total photovoltage generation. The amplitudes of the three exponential photovoltage build-up components are given relative to the overall generated voltage ΔΨI + ΔΨII + ΔΨIII. The results are shown as mean ± SD of n = 3 membranes.

The contributions to the overall photovoltage generation, which is proportional to the transferred charge, were also looked at and their pH dependences illustrated in Figure 3.17. The contribution of $\Delta\Psi$I increases between pH 4.5 and 9.0, from 12.5% to 55.3%. At pH 9.5 and 10 a stagnation and a small reduction are observable. The relative contributions of $\Delta\Psi$II between pH 4.5 and 7.4 are quite stable at approximately 12%, but with higher values an increase can be observed up to 26% at pH 10. The relative $\Delta\Psi$III has a quite strong pH dependence similar to $\Delta\Psi$I only that the decrease of the relative $\Delta\Psi$III takes place with increasing pH. The share of transferred charge attributed to the slowest step is reduced from 72.5% to 28.7% between pH 4.5 and 10. The only outlier in this trend is the value at pH 9.5 with 23.8%.

The single turnover experiments on NsXeR wild type reconstituted in proteoliposomes determined a slow transition step with t_3 (15.4 ± 1.5 ms, pH 7.4, n = 3) which is in agreement with the slowest current decay in patch clamp single turnover experiments ($\tau_2 = 10.9 \pm 0.7$, pH 7.4, 0 mV membrane potential, n = 5) in Section 3.2 (Figure 3.6).

4 Discussion Part I: Characterization of NsXeR

4.1 pH Dependence of NsXeR Inward Proton Pumping

The inward proton pump currents of NsXeR were investigated in whole-cell patch clamp measurements on NsXeR expressing NG108-15 cells under continuous 561 nm illumination. At all applied membrane potentials and pH gradients inward pumping could be observed proving that NsXeR is a potent proton pump that can work against high electrochemical loads.

The steady-state photocurrents followed a linear potential dependence as well as the decay rate constants k_2 (Figure 3.5) which indicates that the photocurrents are mainly kinetically limited by a photocycle transition step that is described by k_2. A comparison of k_2 and the photocycle kinetics in Figure 1.8 allows the conclusion that the transition step limiting the photocurrents is the MII decay (k_2 = 83 Hz at pH 7.4 and 0 mV versus $1/\tau_{MII} = 1/(27\text{ ms}) = 37$ Hz) as was previously suggested by Shevchenko *et al.* [32].

The intracellular pH was varied in order to further investigate the character of the rate-limiting transition. With minor exceptions neither the decay rate constants k_2 nor the apparent potentials E_0 derived from the steady-state currents showed a significant dependence on the intracellular pH (Figure 3.5 B and Table 3.2). Since the MII decay was assigned to the reprotonation of the retinal Schiff base from Asp76, located in the extracellular half of the protein, and an extracellular proton uptake, the results are in line with the proposed photocycle model [32] (Figure 1.4). In that case, rather than an intracellular an extracellular pH dependence would be expected. Indeed, the extracellular pH has an influence on the steady-state currents as well as the decay kinetics as was found by T. Wießalla [121] (Figure 4.1). Upon reduction of the extracellular pH the steady-state photocurrents were reversibly reduced by a factor of 0.68 (at 0 mV) (Figure 4.1 A) which is in the same range as the reduction of k_2 (0.63 at 0 mV) (Figure 4.1 B). Therefore, the reduced steady-state photocurrents can be explained by a slowed down MII decay. If the MII to ground state transition was ruled by a reprotonation from the extracellular bulk solution the opposite pH dependence would be expected [122].

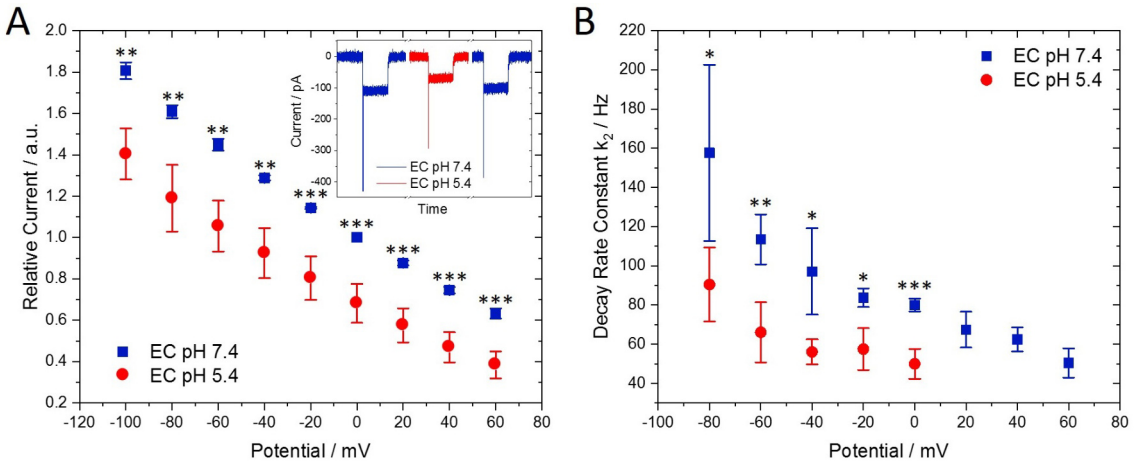

Figure 4.1: Potential dependence of relative steady-state photocurrents (A) and the second decay rate constant k_2 (B) from continuous 561 nm illumination measurements at IC pH 7.4 and EC pH 7.4 and 5.4. (A) Steady-state photocurrents were rundown corrected and normalized to the current at pH 7.4 0 mV. The inset shows the reversible reduction of the photocurrents upon extracellular pH change from 7.4 to 5.4 and back to 7.4. The differences were significant with: * $p < 0.05$, ** $p < 10^{-3}$ and *** $p < 10^{-4}$ (with $n = 5$). Data was taken from [121].

In the BLM measurements on NsXeR proteoliposomes, the pH was changed in a symmetrical manner and three electrogenic steps were identified (Figure 3.14). The kinetics of the third electrogenic step correlate with the second decay rate constants from the patch clamp measurements (Table 4.1). Therefore, this step is likewise assigned to the MII decay and due to the results in the patch clamp measurements it can be assumed that its pH dependence is mainly based on the pH of the proton uptake side.

pH	**Flash photolysis**	**BLM**	**Patch clamp**	**Patch clamp**
	$\tau_{MII \rightarrow GS^*}$	t_3	$1/k_2$	τ_2
7.4	36 ms	15 ms	12 ms	11 ms
9.0	14 ms	7 ms	-	-

Table 4.1: pH dependence of the slowest electrogenic step from patch clamp and BLM measurements and decay time constant of the MII decay from flash photolysis measurements (done by C. Boumrifak, Wachtveitl Group, Goethe Universität Frankfurt). Flash photolysis measurements were performed on the solubilized protein. GS* is a long-lived ground state like intermediate that seems to be excitable like the ground state. In BLM measurements NsXeR proteoliposomes were used and illuminated with a ns light pulse. In patch clamp experiments NsXeR expressing NG108-15 cells at IC = EC pH 7.4 were illuminated continuously ($1/k_2$ from Figure 3.5 B) or with a ns light pulse (τ_2 from Figure 3.6 B).

The third electrogenic step is accelerated at high pH values (Figure 3.16 C) which was also found for the MII decay in flash photolysis measurements on solubilized NsXeR protein (done by C. Boumrifak, Wachtveitl Group, Goethe Universität Frankfurt) (Table 4.1). As mentioned earlier, the pH dependence of the MII decay excludes a direct reprotonation of the retinal Schiff base from the extracellular bulk. Shevchenko *et al.* [32] proposed that the SB is reprotonated from a donor group (Asp76) which would explain a pH independence. The acceleration at high pH values actually suggests that the limitation is caused by a deprotonation reaction. The intracellular proton release from the putative acceptor D220 can be excluded as a limitation since the pH dependence only occurs for the extracellular side and measurements of pyranine fluorescence indicate that the MII decay is accompanied by a proton uptake and the MI rise by proton release (personal communication, C. Boumrifak, Wachtveitl Group, Goethe Universität Frankfurt). The protonation state of a group near the active center could possibly have an influence and block the SB reprotonation at lower pH values. It is further possible that the reprotonation of the retinal Schiff base is limited by a reisomerization that might be dependent on the protonation state of that group.
Similar to the present data an acceleration of the SB reprotonation at higher pH values was also found for the inward proton pump PoXeR [38] and the XeR homolog ASR [123]. In the case of PoXeR, it was suggested that the SB reprotonation is limited by the thermal isomerization of the retinal rather than a proton transfer step due to a negligible kinetic isotope effect [48]. In order to further investigate the mechanism of the SB reprotonation in NsXeR, H_2O/D_2O exchange measurements would give further insights.

4.2 Mutations of Residues in the Putative H^+ Transfer Pathway

Insights into the overall pump mechanism can be provided by mutational studies on side chains that are putatively part of the H^+ transfer pathway.
The results on the Asp220 mutants revealed the central importance of the group for inward proton pumping. The neutralization of the side chain in D220N impaired proton pumping further confirming its role as an acceptor to the retinal SB proton as was suggested by Shevchenko *et al.* [32]. The UV-Vis absorption spectrum of D220N shows no influence on the maximal absorbance wavelength compared to the wild type which indicates that Asp220 does not act as a counterion to the retinal SB (Figure 3.1 and Table 3.1). Flash photolysis measurements on the D220N mutant (done by C. Boumrifak, Wachtveitl Group, Goethe Universität Frankfurt) revealed a photocycle with two L and a single M intermediates with a $\tau_{LII\rightarrow M}$ time constant of 26 ms. The appearance of this long-lived L intermediate suggests that the deprotonation of the SB is disturbed due to the neutral-

ization of the proton acceptor which is in line with the previous findings [32].
In patch clamp measurements, the kinetics of the rate-limiting step were reduced by a factor of 3 upon exchanging the ionizable residue of the acceptor in D220E (Figure 3.9). Similarly, the MII decay was slowed down by a factor of 2.5 (from 36 ms to 89 ms) in flash photolysis measurements (done by C. Boumrifak, Wachtveitl Group, Goethe Universität Frankfurt). A possible explanation for this behavior could be a deceleration of the intracellular proton release. If the proton release was retarded due to a probably higher H^+ affinity of Glu compared to Asp [120], the release step might have become rate-limiting. On the other hand, the reprotonation of the retinal Schiff base might still be the rate-limiting step that is altered due to the influence of D220E on the electronic environment of the active center. In UV-Vis spectroscopy pH titration measurements, a lowering of the SB pK_a from 9.6 to 8.4 was observed for the D220E mutant compared to the wild type (Table 3.1). Therefore, the reprotonation of the retinal SB might have slowed down due to a lowered proton affinity of the SB in the ground state.
Glu228 of the putative proton release group His94-Glu228 was exchanged for Asn and Asp, but no influence of the mutations could be observed at pH 7.4. Either the His94-Glu228 pair is not part of the proton release pathway or proton release at pH 7.4 is not rate-limiting for the mutants E228N and E229E. The absence of the proton release group in E228N might be compensated through a direct release from Asp220 to the intracellular bulk.

For more insights on the nature of the rate-limitation in the D220E mutant and the role of Glu228, patch clamp measurements at more extreme intracellular pH values would be valuable. If rate-limiting steps involve proton exchange with the intracellular lumen an intracellular pH dependence should become visible. Fourier-transform infrared spectroscopy (FTIR) measurements could give further information on the protonation states of the residues during the photocycle.
In contrast to the primary proton acceptor Asp85 in BR, Asp220 in NsXeR is not part of the counterion complex to the protonated retinal Schiff base. Mutating Asp85 in BR to Glu accelerates the M formation 10-fold [124], but the higher pK_a of > 7 of the acceptor group prevents the deprotonation of the SB under standard conditions causing loss of proton translocation [125, 126]. Mutants lacking the proton acceptor Asp85 (D85N, D85T) have a red-shifted absorbance maximum and a reduced SB pK_a of 8.6-8.9 [127]. As described above, a similar influence of D220N could not be found which can be explained by the large distance of 12 Å between Asp220 and the Schiff base [32].

4.3 Blue-Light-Effect

In NsXeR the application of blue light in addition to continuous 561 nm illumination leads to current transients of potential dependent vectoriality (Figure 3.12 A) which is a new observation for microbial rhodopsins. The blue-light-quenching (BLQ) effect observed for BR and PR always features a reprotonation of the retinal Schiff base from the primary proton acceptor inverting the previous charge transfer [77, 128, 129]. Since a switch of the retinal SB accessibility is expected while the Schiff base is deprotonated, M intermediates before and after a switch can be excited by blue light. For BR it was suggested that the absorption of a second blue photon either takes place before the switch (MI excited, access to extracellular) or a fast switch occurs after blue light absorption but before a proton transfer (MII excited, access to cytoplasmic) to account for the uniform reprotonation from the primary proton acceptor Asp85 [130]. In studies of the BLQ process in PR, Eckert *et al.* similarly proposed a switch of the SB orientation upon blue light absorption of the M intermediate. The resulting proton transfer then takes place from the primary proton acceptor Asp97 and not Glu108, the proton donor in the regular photocycle [77].

In contrast to BR and PR the NsXeR photocycle features two distinct M intermediates MI and MII with a transition time in the millisecond time range (Figure 1.4). It was proposed that the SB accessibility switches from the cytoplasmic to the extracellular (Figure 4.2 A) during this transition [32]. In continuous 561 nm background illumination it is expected that both intermediates accumulate and can be excited by blue ns light pulses. To account for the potential dependent switch and blue-light induced current transients in NsXeR a simplified photocycle model is proposed (Figure 4.2 B).
At a membrane potential of 0 mV the blue light induced current transient is biphasic and very small (Figure 3.12 A). Assuming that upon blue light absorption the retinal SB of molecules in the MI intermediate are reprotonated from Asp220, an outward current would be expected. The Schiff base reprotonation in MII from Asp76 would result in an inward current (Figure 4.2). Under the assumption that the absolute value of transported charge upon reprotonation from Asp220 and Asp76 is nearly equal, the almost complete cancellation of the transient signal at 0 mV indicates that the MI and MII intermediates are accumulated to nearly equal parts. In order to achieve that an equilibrium has to be postulated between the MI and MII intermediates since otherwise a majority of the population would be expected to accumulate in MII. The potential dependent change of the current transients vectoriality suggests a potential sensitive ratio of the MI and MII populations that can be probed by blue ns light pulses.
At +60 mV membrane potential the rate-limiting transition step from MII to the ground state is slowed down which results in reduced inward steady-state photocurrents at 561 nm

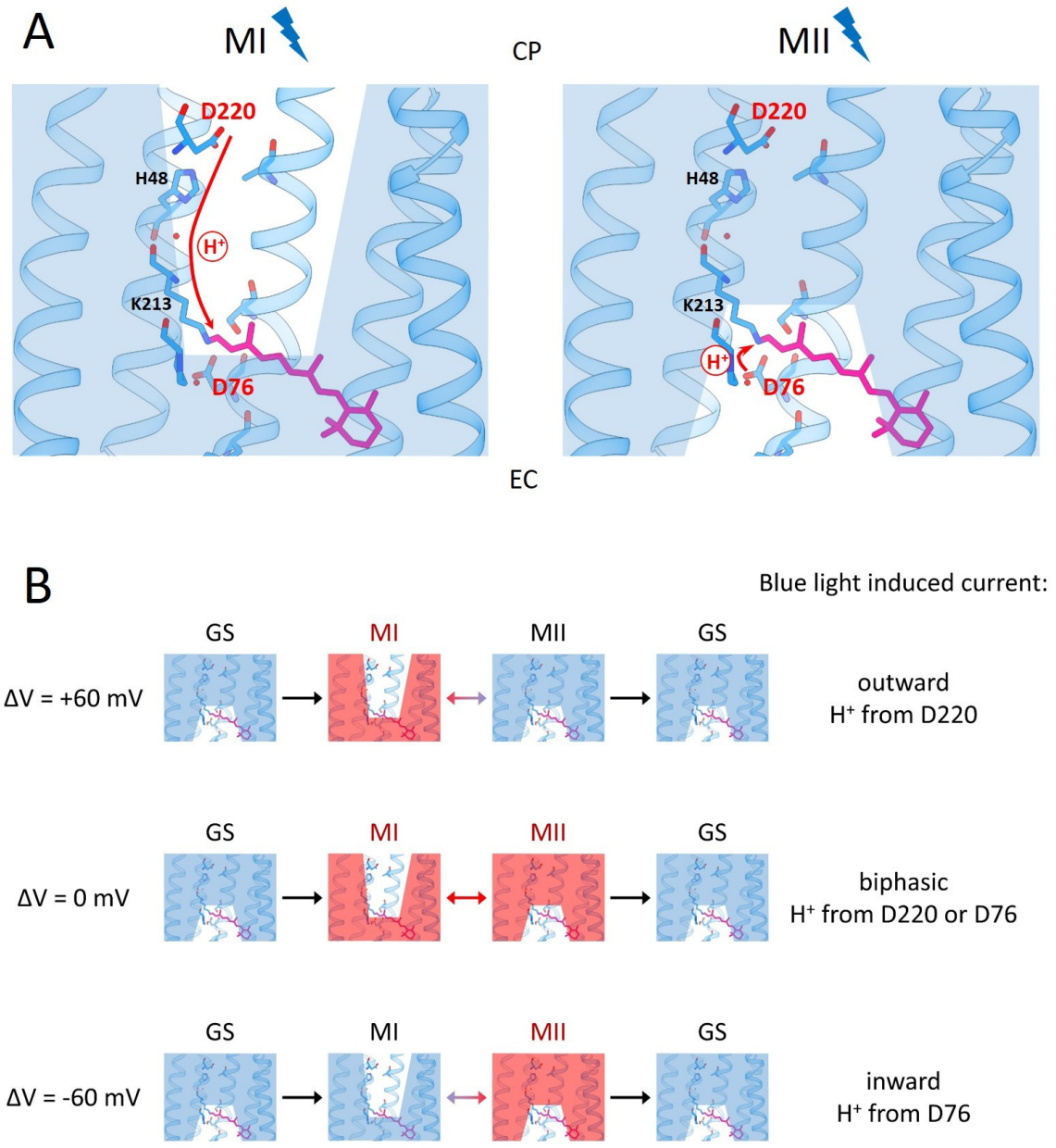

Figure 4.2: (A) Scheme for the retinal Schiff base accessibility in the MI and MII intermediate for NsXeR and the suggested proton transfer events to the SB upon absorption of a second blue photon by those intermediates. The primary proton acceptor Asp220 and the putative proton donor Asp76 are labeled in red. The retinal chromophore is illustrated in pink and the red arrows indicate the proton transfer steps. The scheme is based on the ground state NsXeR structure (PDB ID: 6eyu) [32]. (B) Scheme for the potential sensitive MI/MII ratio and the blue light induced transient currents in NsXeR. MI and MII are equally populated at 0 mV. At +60 mV and -60 mV the equilibrium is shifted to MI and MII, respectively.

illumination (Figure 3.5). The potential dependence of other electrogenic steps in the NsXeR photocycle could not be studied, but the existence of at least three was determined in the BLM measurements (Figure 3.14). As mentioned above, the third electrogenic step can be assigned to the MII decay. The first and second steps with the decay time constants 220 μs and 0.9 ms (at pH 7.4) correlate with the L to MI (290 μs) and MI to MII (2.5 ms) transitions from flash photolysis measurements (done by C. Boumrifak, Wachtveitl Group, Goethe Universität Frankfurt), respectively. Since the charge transport of all three steps is inwardly directed, it can be assumed that a positive potential acts decelerating on the related photocycle transitions. Then, the MI to MII transition would be decelerated and the reverse MII to MI accelerated. Therefore, at +60 mV the ratio of accumulated molecules during the steady-state is shifted to MI which results in a blue-light induced outward current transient due to a reprotonation of the Schiff base by Asp220 (Figure 3.12 A). The opposite is the case at -60 mV where the ratio is shifted to MII causing a reprotonation from Asp76 with inward current transients.
The blue-light effect observed for the mutant D220E exclusively shows outward current transients indicating a reprotonation from the primary proton acceptor Glu220 (Figure 3.12 B). The mutant behaves similar to the wild type at +60 mV. In both cases the MII decay was decelerated causing a shift of the MI/MII equilibrium to the intracellularly accessible MI intermediate.

It would be possible that the variability of the blue-light-effect in NsXeR could be caused by an additional blue absorbing ground state species. In measurements without the 561 nm background illumination the wild type showed inward transient currents when excited with blue light pulses (Figure 3.13 A). Therefore, it can be excluded that a blue absorbing ground state is responsible for the blue-light-effect in NsXeR wild type and the photo excitation of the M intermediates is mainly responsible for the observations as proposed above.
In the case of the D220E mutant a biphasic current transient was observed at pH 8.4 when excited with blue ns light pulses without 561 nm background illumination (Figure 3.13 C). Since the SB pK_a of D220E is lowered to 8.4 compared to the WT at 9.6 (Table 3.1) it can be concluded that the fast outward current occurring at pH 8.4 (Figure 3.13 C) is caused by a ground state species with a deprotonated Schiff base. The vectoriality of the fast outward current proposes a similar situation to the MI intermediate with a proton transfer from Glu220 to the SB (Figure 4.2 A).
The blue absorbing ground state or M-like species of D220E caused by titration seems to be sensitive to the applied membrane potential (Figure 3.13 C) similar to the light-induced M intermediates of the wild type (Figure 3.12 A).

The blue-light-effect in NsXeR shows the different nature of the NsXeR accessibility switch compared to BR. While a potential dependent shift of the equilibrium between M intermediates was also postulated for BR [75], the blue photon absorption of the MI and MII intermediates is followed by a fast proton transfer before the accessibility of the retinal Schiff base can relax to the ground state situation. The blue-light-effect in NsXeR could be a helpful tool in optogenetic applications. The currents induced by 561 nm light illumination could be up- or down-regulated by additional blue light. Experiments with additional continuous blue light illumination would give further insights.

4.4 Extended NsXeR Photocycle

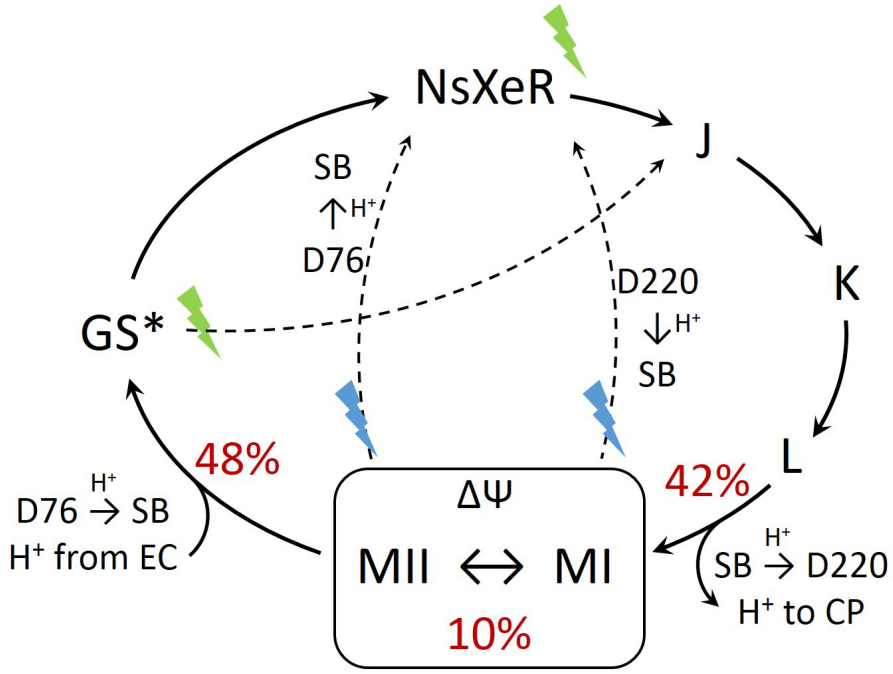

Figure 4.3: Extended photocycle scheme for NsXeR. The given intermediates were identified in flash photolysis measurements on solubilized protein (done by C. Boumrifak, Wachtveitl Group, Goethe Universität Frankfurt). GS* is described as a ground state like intermediate. The green and blue flash symbols indicated the absorption of a green or blue photon, respectively. The intermediates MI and MII are in a potential sensitive equilibrium. The percentages in red indicate the contributions to the overall charge displacement at pH 7.4 as determined in the BLM experiments.

The electrogenic steps determined in BLM and patch clamp measurements were assigned to the transitions in the NsXeR photocycle (Figure 4.3) based on the correlation of the fitted exponential time constants to flash photolysis data (Figure 4.4). As mentioned before,

the fastest component in the BLM measurements with t_1 was attributed to the L to MI transition. It is assumed that in this transition the retinal Schiff base proton is accepted by Asp220 and a proton release to the intracellular side takes place. The acceleration of t_1 with increasing pH values (Figure 3.16 A) supports this view since a proton release is expected to be faster at low proton concentrations. The second electrogenic step with the time constant t_2 is assigned to the MI to MII transition. t_2 is widely pH independent which is in agreement with the assumption that the transition describes a switch of the retinal Schiff base accessibility from the intracellular to the extracellular side [32]. Rather than a proton transfer step, the transition might be ruled by a conformation change that would not be expected to be highly sensitive to pH changes. The third electrogenic step from BLM measurements is attributed to the MII decay as was discussed above. The reprotonation of the retinal Schiff base supposedly occurs from Asp76. Due to its position the residue most likely acts as the counterion to the protonated Schiff base in the ground state (Figure 1.3). Also at different pH values Asp76 seems to stay deprotonated since in the UV-Vis absorption spectrum of NsXeR wild type the absorption maximum of the deprotonated Schiff base is hardly affected by pH changes (Figure 3.3 A). Therefore, in order to act as a donor Asp76 would have to transiently bind a proton in the course of the photocycle.
With the correlation of the electrogenic steps to the photocycle, the contributions to the overall charge displacements can be assigned to the respective transitions (Figure 4.3). The MI to MII transition is responsible for a rather small proportion of charge displacement (10% at pH 7.4) that is rather unaffected by pH changes ($\Delta\Psi$II in Figure 3.17). The small contribution makes sense as no protonation or deprotonation events were attributed to the MI to MII transition. The major charge displacement is split up between the MI rise and the MII decay as would be expected. At pH 7.4 nearly equal charge is transported in each transition, but the contributions are strongly pH dependent (Figure 3.17). An explanation for the pH dependent redistribution of transported charge might be that at low pH the SB is deprotonated, but proton release does not take place and the proton stays bound to Asp220 or another residue. Upon reprotonation of the Schiff base and extracellular proton uptake, the Asp220 bound proton may be simultaneously released with the kinetics of the MII decay. With increasing pH values the immediate proton release during the L to MI transition might become more likely shifting the charge transfer to the earlier transition in the photocycle.

The MII intermediate relaxes to the NsXeR ground state via a long-lived ground state like GS* intermediate that was identified in flash photolysis measurements (done by C. Boumrifak, Wachtveitl Group, Goethe Universität Frankfurt). In patch clamp measurements, robust inward currents of -2.9 ± 2.6 pA/pF (pH 7.4 at 0 mV) were measured that decayed with the kinetics of the MII decay. Also, no current reductions upon repeated

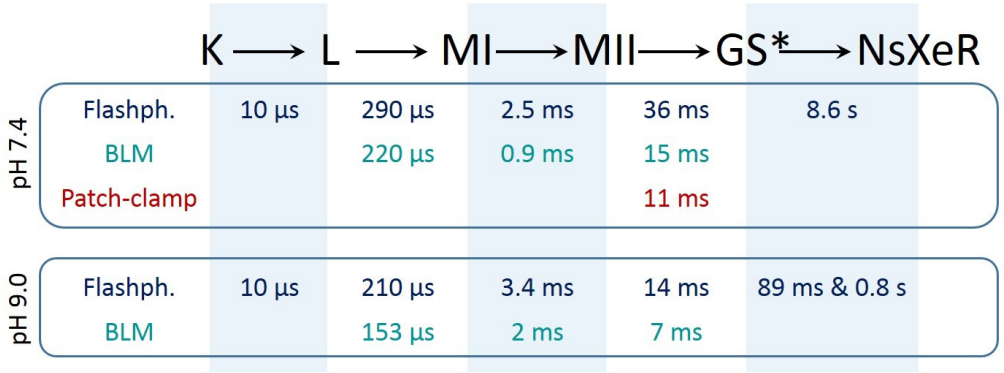

Figure 4.4: Assignment of the exponential time constants of electrogenic steps to the transitions in the NsXeR photocycle. Flash photolysis measurements were performed on solubilized protein (done by C. Boumrifak, Wachtveitl Group, Goethe Universität Frankfurt). Single turnover experiments were performed on NsXeR reconstituted in proteoliposomes in BLM measurements and on NsXeR expressing NG108-15 cells in patch clamp experiments.

illumination could be detected indicating that no proteins were trapped in a long-lived state. Therefore, it is assumed that the GS* state similar to the NsXeR ground state is excitable by green light which induces a regular photocycle.
A short-circuiting of the NsXeR photocycle is possible by the blue light illumination of the M intermediates that are in a potential sensitive equilibrium. Upon the absorption of a blue photon by MI or MII the retinal Schiff base is either reprotonated from Asp220 or Asp76, respectively.

4.5 Vectoriality

The inward proton pumping of NsXeR gives rise to the question for the determinants of the pumps vectoriality that cannot easily be answered. NsXeR is one of the first natural inward proton pumps found among microbial rhodopsins [32], but inward proton pumping was observed before.

The BR wild type acts as a natural outward proton pump, but the transport vectoriality could be inversed in the mutant D85T [127]. The lack of the primary proton acceptor enables inward pumping in a process that requires the absorption of two photons [127]. The outward proton pump proteorhodopsin inverses proton transport in an acidic environment and at hyperpolarizing membrane potentials [131]. It was suggested that the protonation state of the acceptor Asp97 in PR is the key determinant for the transport modes [131]. Both inward and outward pump mechanisms could be explained using the IST model [130]. The three principle events that have to occur according to the model

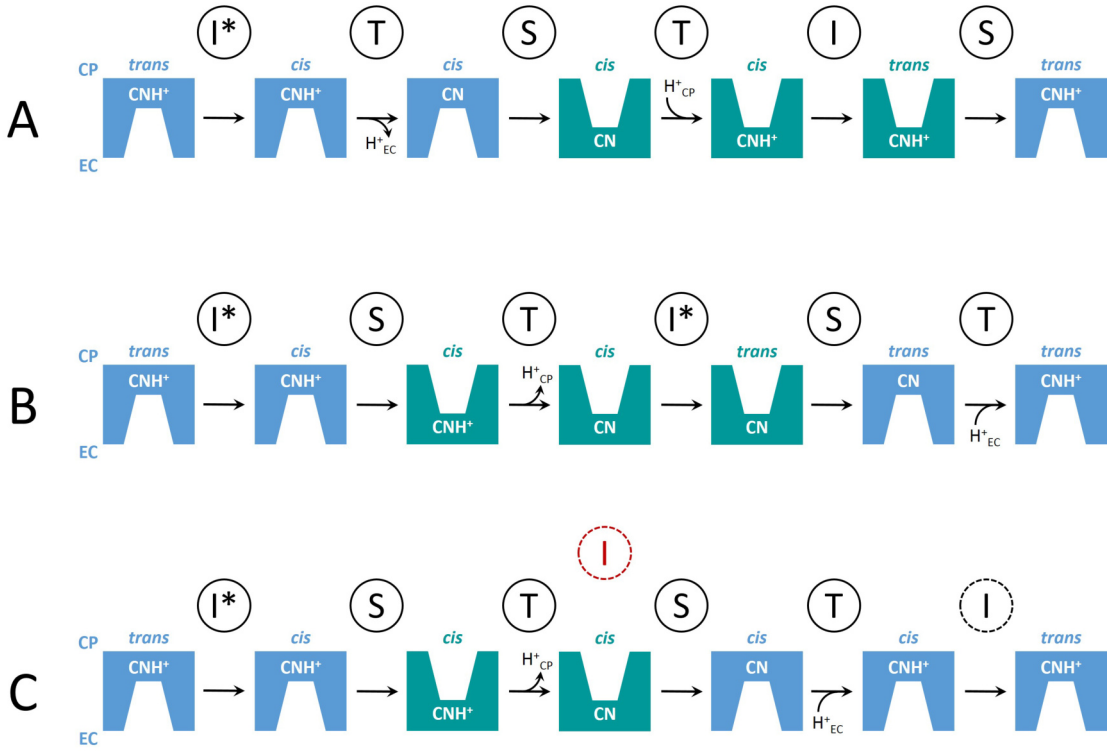

Figure 4.5: IST model for different proton transport reactions [130]. (A) Outward proton transport by BR wild type and by PR at alkaline pH. (B) Inward proton transport driven by the absorption of two photons. (C) Suggested reaction scheme for NsXeR inward proton pumping with a thermal isomerization (I) as final step. The red symbol indicates where the thermal isomerization would have to take place according to the model.

are the isomerization of the retinal (I*), the switch of the SB accessibility (S) and proton transfer steps that protonate or deprotonate the retinal Schiff base (T). Every event has to be reversed for a complete photocycle and the retinal reisomerization can occur thermally (I) or by absorption of a second photon (I*). The switch and the proton transfer steps are assumed to be kinetically independent. The model further postulates that the isomerization state of the retinal directs the accessibility of the SB with all-*trans* to the extracellular and 13-*cis* to the intracellular side. According to the model the outward proton transport of BR and PR can be described by the sequence I*/T/S/T/I/S [130, 131] (Figure 4.5 A). Inward transport follows a different sequence I*/S/T/I*/S/T, where a switch follows after the first retinal isomerization since the proton transfer step is kinetically constrained due to the lack of a proton acceptor (Figure 4.5 B). Applying the model to NsXeR, the first isomerization would have to be followed by a switch before the Schiff base is deprotonated to the intracellular side (Figure 4.5 C). A thermal isomerization would have to occur before the second switch according to the model, but results from IR spectroscopy measurements

point to a later reisomerization of the retinal (personal communication, C. Boumrifak, Wachtveitl Group, Goethe Universität Frankfurt). The second switch is followed by a proton transfer to the SB from the extracellular side and the final reisomerization of the retinal. In contrast to the situation for inward proton transport of BR and PR, NsXeR features Asp76, an ionizable residue close to the Schiff base at the extracellular side. Nevertheless, a fast accessibility switch seems to occur before a proton can be transferred.
In the NsXeR homolog ASR, inward proton transport was created by mutating Asp217 to a Glu residue which acts as a proton acceptor [132]. For the wild type it is proposed that upon M formation the Schiff base proton is transferred inwardly or outwardly, but Asp75 (corresponding to the putative donor Asp76 in NsXeR) is not protonated throughout the photocycle [132, 133]. The inward proton transport of ASR D217E was explained by the high proton affinity of Glu that forces the SB reprotonation from the extracellular side. The proposed proton transport mechanism goes without an accessibility switch for the retinal SB.

A major difference between NsXeR and BR is the absence of a second negatively charged residue located in the extracellular half as Asp212 in BR is replaced by Pro209 in NsXeR [32]. This may be the cause for a different more intracellularly directed orientation of the SB and a more subtle switching mechanism. The different nature of the accessibility switch of NsXeR compared to BR already became visible in the blue-light-effect. While switching is accompanied by conformational changes with helix movements in BR [134–136], the switch in NsXeR might consist of small changes like a rotation change in retinal or a rearrangement of hydrogen bond networks.

5 Results Part II: Characterization of KR2

5.1 Sodium Dependence of Outward Pump Currents

5.1.1 Continuous Illumination Measurements

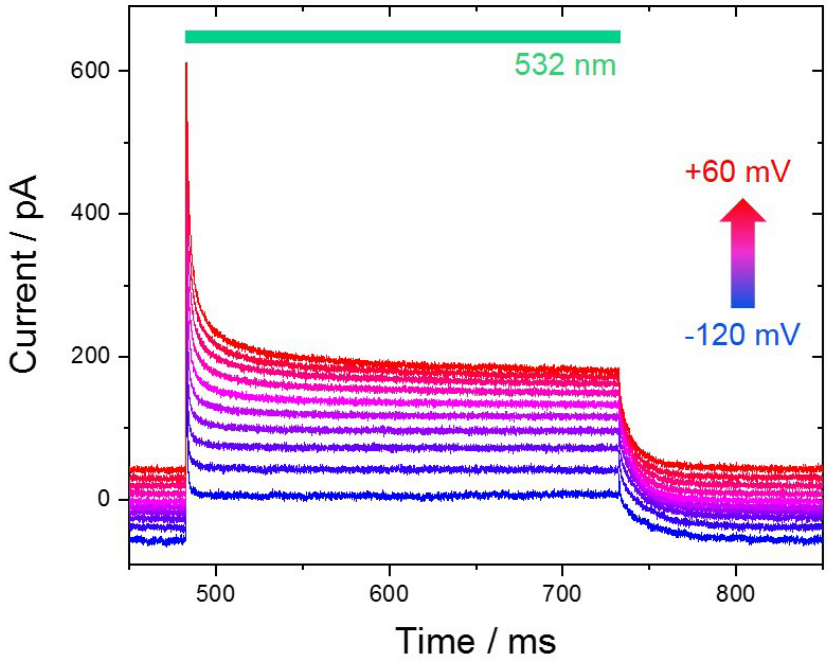

Figure 5.1: Whole-cell patch clamp current measurements of KR2 expressing NG108-15 cells in response to continuous illumination with 532 nm light. The intra- and extracellular solution contained 25 mM NaCl. The pH was adjusted to 6.0 and 7.4 for the intracellular and extracellular solution, respectively. Membrane potentials between -120 mV and 60 mV were applied in 20 mM intervals.

The outward pump currents of KR2 were investigated by voltage clamp measurements of the enzyme heterologously expressed in NG108-15 cells. A typical measurement of the light induced currents can be seen in Figure 5.1. At every applied membrane potential between -120 and 60 mV a positive transient peak current can be observed upon onset of

[Na] in mM	I_{ss}/C_{cell} in pA/pF	n
0	1.9 ± 1.2	11
1	1.3 ± 0.5	9
5	2.6 ± 1.1	9
25	3.0 ± 0.8	7
50	4.3 ± 2.4	11
140	2.1 ± 0.7	6

Table 5.1: Current densities calculated from the steady-state currents I_{ss} of KR2 at 0 mV membrane potential and the cell capacitances C_{cell}. The intra- and extracellular solutions contained the same NaCl concentration. The results are shown as mean ± SD.

the green illumination. The peak currents decay to a stable steady-state level that is dependent on the applied membrane potential. The steady-state currents decay back to the initial dark current levels in the time period of some 10 ms after the end of the illumination. The positive photocurrents indicate a transport of positive ions from the inside of the cells to the outside. The transported ions were shown to be sodium ions and protons in the absence of sodium [33].

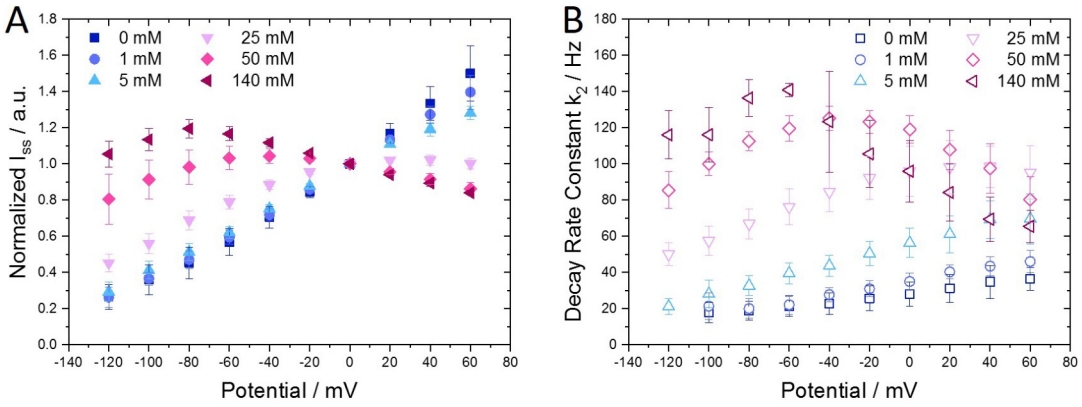

Figure 5.2: Sodium dependence of whole-cell patch clamp measurements on KR2 expressing NG108-15 cells in response to continuous 532 nm illumination. The sodium concentration was changed in a symmetrical manner in the intracellular and extracellular solutions. The pH was adjusted to 6.0 and 7.4 for the intracellular and extracellular solution, respectively. (A) Voltage dependence of the steady-state photocurrents of KR2 at different sodium concentrations. The currents were normalized to the value at 0 mV. The means of n = 11 (0 mM), n = 9 (1 mM), n = 9 (5 mM), n = 7 (25 mM), n = 11 (50 mM) and n = 6 (140 mM) cells were evaluated. (B) The slow decay rate constant k_2 was determined as described earlier (3.5). The means of n = 4 (0 mM), n = 4 (1 mM), n = 5 (5 mM), n = 6 (25 mM), n = 8 (50 mM) and n = 3 (140 mM) cells were evaluated.

[Na] in mM	E_0 in mV	n
0	-151 ± 24	11
1	-157 ± 13	9
5	-174 ± 12	9

Table 5.2: Apparent potentials E_0 of zero current derived from fits of the linear voltage dependence of the steady-state currents I_{ss} from Figure 5.2 A. The results are shown as mean ± SD.

In Na^+ titration measurements the sodium concentration was changed in a symmetrical manner in the intracellular and extracellular solutions. The intracellular was slightly more acidic than the extracellular with pH 6.0 and 7.4. The voltage dependence of the steady-state currents I_{ss} was analyzed at different sodium concentrations depicted in IV plots in Figure 5.2 A. In order to account for different cell sizes and expression levels the currents were normalized to the currents at 0 mV. The current densities I_{ss}/C_{cell} found at 0 mV are summarized in Table 5.1.

The character of the voltage dependences in the IV plots (Figure 5.2 A) is strongly influenced by the amount of the supplied sodium. Up to a concentration of 5 mM NaCl in the solutions, the steady-state currents exhibit a linear voltage dependence. The apparent potentials E_0 (potentials of zero current) can be extrapolated by performing linear fits. The results are summarized in Table 5.2. A significant difference between the E_0 potentials could only be found for 0 mM and 5 mM NaCl, while the other cross comparisons showed no differences. The determined apparent E_0's are less hyperpolarizing than the -220 mV found for bacteriorhodopsin [76] which suggests that the voltage dependence of the ion pumping in KR2 is stronger compared to BR.
Increasing the NaCl concentrations to 25 mM, 50 mM and 140 mM leads to a change of the I_{ss}'s voltage dependence to a rather bell-shaped manner. While the IV curve seems to saturate at membrane potentials above 0 mV for 25 mM NaCl, further increasing the sodium concentration shows that the currents pass a maximum and decrease after a certain membrane potential that is shifted to more negative values with more NaCl supplied. A similar behavior could be observed analyzing the kinetics of the steady-state current decay after the end of the illumination. The decay back to the dark current levels was fitted with two exponentials. The faster component was affected by the shutter closing time of 0.8 ms, but the rate constant of the slower decay k_2 was plotted in Figure 5.2 B. In accordance to the steady-state currents, k_2 is linearly dependent on the applied membrane potential at 0 mM, 1 mM and 5 mM NaCl. Furthermore, k_2 increases with the sodium concentration. The same is true for even higher amounts of sodium in the solutions at membrane potentials of -60 mV and lower.

The appearance of a maximum rate and and a decrease at higher potentials at high sodium

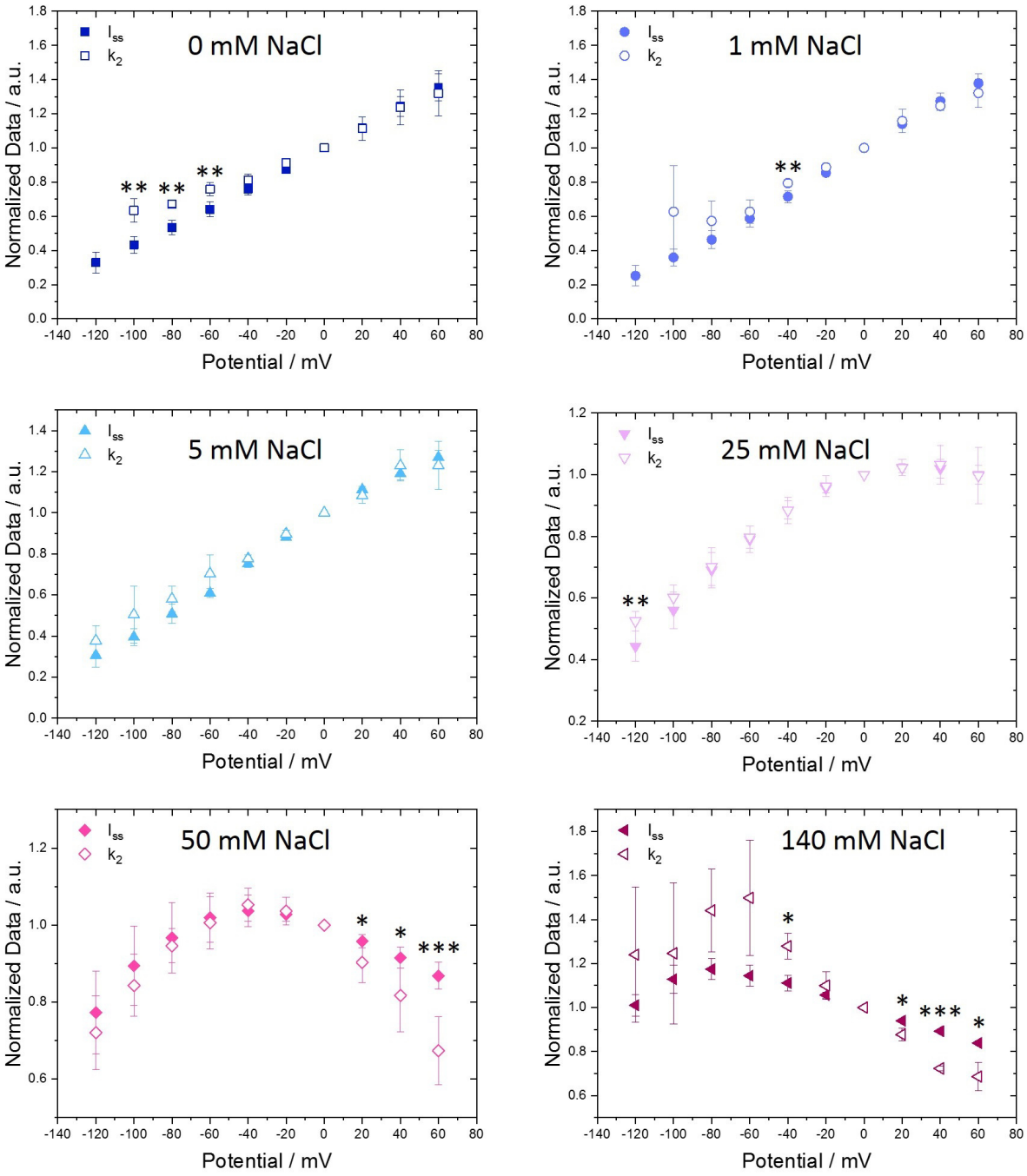

Figure 5.3: Normalized steady-state currents I_{ss} and slow decay rate constants k_2 in dependence of the membrane potential. For the steady-state currents I_{ss} only cells were taken into account whose kinetics (k_2) were analyzable. I_{ss} and k_2 were normalized to the value at 0 mV. Significance tests were performed and differences were marked: *: $p < 0.05$, ** $p < 0.01$ and ***$p < 10^{-4}$. The means of n = 4 (0 mM), n = 4 (1 mM), n = 5 (5 mM), n = 6 (25 mM), n = 8 (50 mM) and n = 3 (140 mM) cells were evaluated.

concentrations can also be observed. In order to check if the potential dependence of I_{ss} and k_2 correspond, k_2 was also normalized to the value at 0 mV and the data was compared in Figure 5.3. It can be seen that the potential dependences of the steady-state photocurrents and the slow decay rate constants are basically in good agreement. At 1 mM, 5 mM and 25 mM NaCl no or only minor deviations can be observed. At 0 mM, 50 mM and 140 mM NaCl more differences could be found, but the overall tendencies still correlate.

5.1.2 Laser Flash Illumination Measurements

Single turnover experiments were performed to resolve the faster photocurrent components. The KR2 expressing NG108-15 cells were illuminated with a light pulse of $\geq$ 10 ns and measured in whole-cell configuration at symmetric sodium conditions and a slightly more acidic intracellular as described in the previous section. The short illumination evoked transient photocurrents of outward sodium transport as depicted in Figure 5.4. The rise of the transients is faster than the time resolution of the system. The decay of the current transients was fitted with a three-phase exponential decay function. While the first component is still affected by the low pass properties of the access resistance and the cell capacitance and could not be well resolved, the voltage and sodium concentration dependence of the second and third components were analyzed.

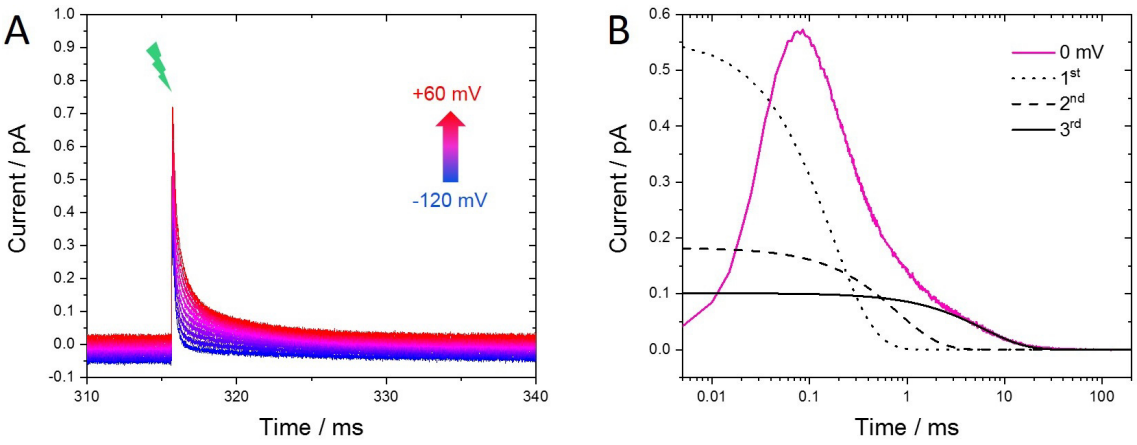

Figure 5.4: Patch clamp single turnover experiments on KR2. NG108-15 cells were illuminated with a $\geq$ 10 ns light pulse of 530 nm at symmetrical 25 mM NaCl conditions. The intracellular and extracellular pH values were 6.0 and 7.4, respectively. (A) Raw whole-cell current measurements at different membrane potentials. (B) Transient at 0 mV after shift of the time axis and reduction of the data density with increasing time. The three exponential components fitted into the current decay are indicated with the dotted (first component), dashed (second component) and solid (third component) black lines.

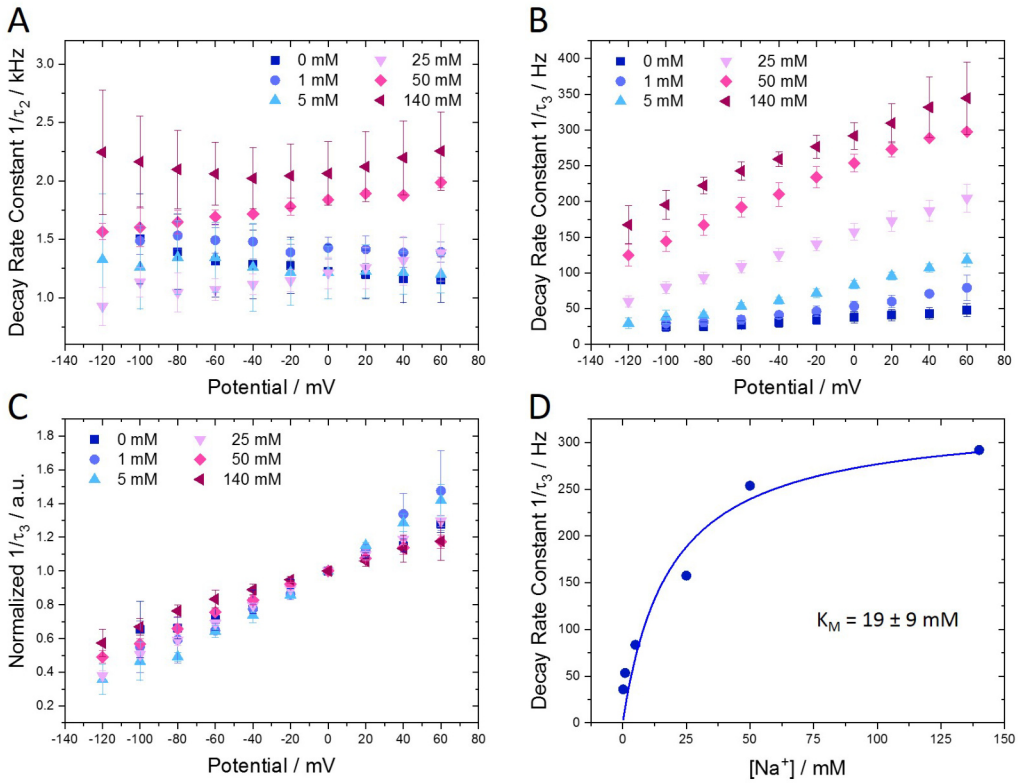

Figure 5.5: Sodium and potential dependence of the KR2 single turnover rate constants. The intracellular and extracellular pH values were 6.0 and 7.4, respectively. Sodium concentrations were varied in a symmetrical manner. In (A) and (B) the absolute rate constants $1/\tau_2$ and $1/\tau_3$ are plotted. (C) $1/\tau_3$ was normalized to the value at 0 mV for each sodium concentration. (D) The $1/\tau_3$ rates were plotted versus the sodium concentration. The line represents a Michaelis-Menten equation that yielded a K_M of 19±9 mM. The means of n = 5 (0 mM), n = 4 (1 mM), n = 6 (5 mM), n = 5 (25 mM), n = 3 (50 mM) and n = 10 (140 mM) cells were evaluated.

In Figure 5.5 A and B the associated decay rate constants were plotted against the potential. The sodium concentrations were varied symmetrically. $1/\tau_2$, the decay rate constant of the second component, shows no or a rather weak dependence on the membrane potential (Figure 5.5 A). Increasing the sodium concentration up to 25 mM does not seem to have a strong influence on the rate constants that range around 1.3 kHz. Higher rates can be observed at 50 mM and 140 mM NaCl, whereby up to 2.3 kHz are reached.
In contrast, $1/\tau_3$ is linearly dependent on the applied membrane potential at all measured conditions (Figure 5.5 B). In order to better compare the potential dependences of $1/\tau_3$ at different sodium concentrations the rates were normalized to the value at 0 mV (Figure 5.5 C). Linear fits of the data were used to determine the apparent membrane potential E_0 at which the rate would drop to 0 Hz. The results are listed in Table 5.3.

[Na] in mM	E_0 in mV	n
0	-248 ± 30	5
1	-178 ± 11	4
5	-172 ± 16	6
25	-198 ± 8	5
50	-249 ± 27	3
140	-315 ± 44	10

Table 5.3: Apparent membrane potentials E_0 at which the rate $1/\tau_3$ would drop to 0 Hz. The results are shown as mean ± SD.

The extrapolated potentials do not show a clear dependence on the sodium concentration between 0 and 50 mM. The only significant differences between these concentrations occurred at 1 mM vs 0 mM, 5 mM vs 0 mM and 50 mM vs 5 mM. Other than that significant E_0 differences were found for every cross-comparison with 140 mM sodium. A systematic dependence on the sodium concentration cannot be concluded for the potential dependence of the rate constant $1/\tau_3$.
Going back to the absolute values in Figure 5.5 B it is clear to see that the rates increase with the amount of sodium provided. For a membrane potential of 0 mV $1/\tau_3$ was plotted against the sodium concentration as can be seen in Figure 5.5 D. The increase of the rate is followed by the onset of a saturation behavior with higher concentrations that was fitted with a Michaelis-Menten equation. A Michaelis constant K_M of 19 ± 9 mM was determined.

Based on the integrals of the fitted components the relative charge transported in the second and third one were calculated. The contribution of the not resolved first component was excluded in the analysis. The potential and sodium dependence of the relative charge contributions Q_2 and Q_3 were analyzed and depicted in Figure 5.6. The summed charge of Q_2 and Q_3 at 0 mV was used as a reference value. A linear potential dependence of the relative Q_2 can be observed at all sodium concentrations with an increase of the charge contribution with more positive potentials. The relative Q_3, on the other hand, changes its potential dependence with the amount of sodium present. While low sodium concentrations like 0, 1 and 5 mM lead to an increase of the transported charge with more positive potentials, a saturation like behavior can be observed at 25 mM. Further increasing the sodium to 50 and 140 mM results in a decrease of the relative Q_3 with more positive potentials. Figure 5.6 shows that up to 25 mM sodium the major share of the transported charge is made up by Q_3 rather than Q_2 at all membrane potentials. Going to 50 and 140 mM sodium, the relative shares of Q_2 and Q_3 become more leveled with increasingly depolarizing potentials. At 140 mM and 60 mV Q_2 is even slightly higher than Q_3.

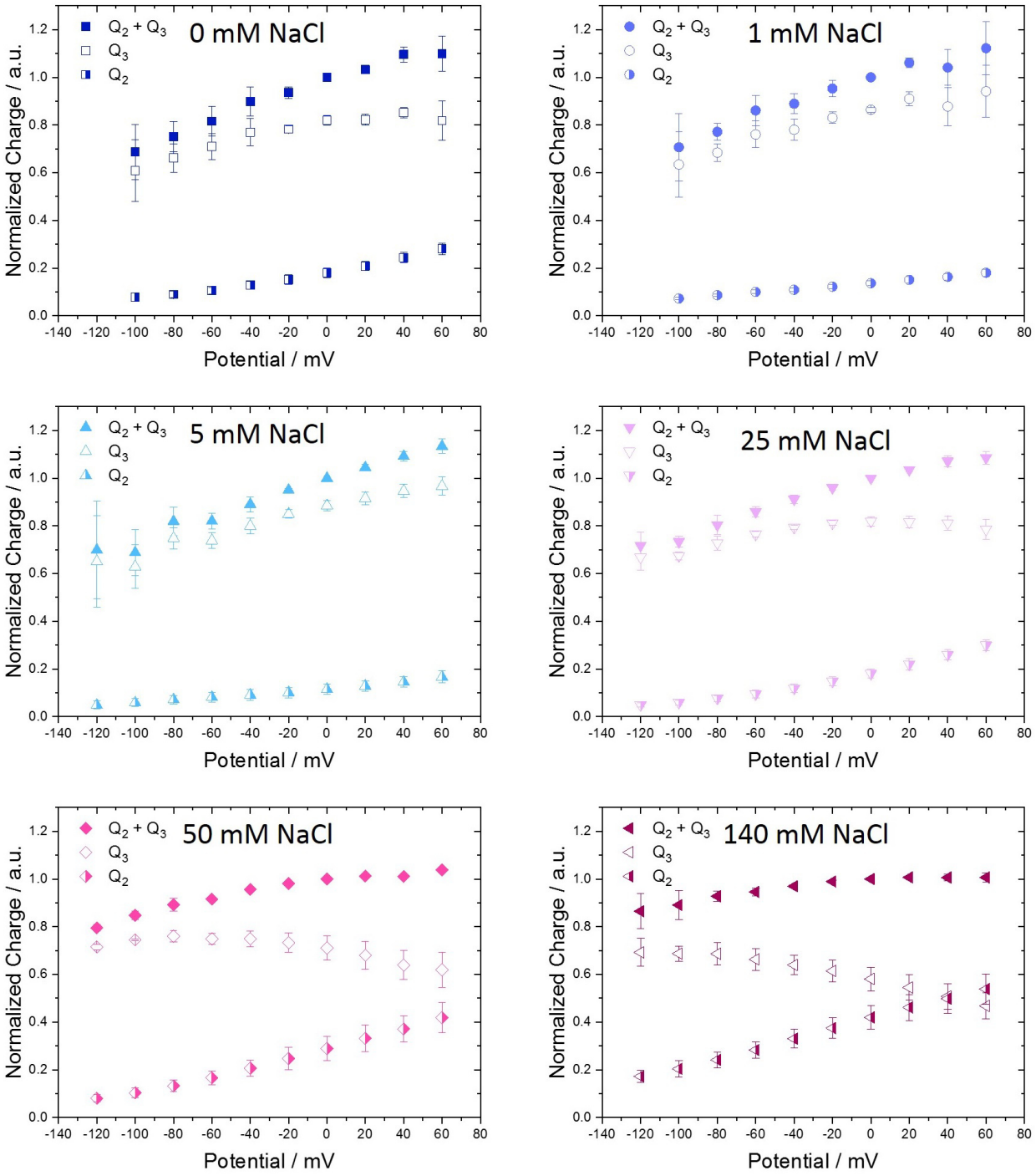

Figure 5.6: Relative charge transported by the second and third exponential decay component in single turnover measurements. Q_2 and Q_3 were determined by integrating the fitted decay components ($Q_i = I_i \cdot \tau_i$). The data was normalized to the value of $Q_2 + Q_3$ at 0 mV. The means of n = 5 (0 mM), n = 4 (1 mM), n = 6 (5 mM), n = 5 (25 mM), n = 3 (50 mM) and n = 10 (140 mM) cells were evaluated.

[Na] in mM	Q_2/Q_3 at 0 mV	n
0	0.22 ± 0.03	5
1	0.16 ± 0.01	4
5	0.13 ± 0.02	6
25	0.22 ± 0.02	5
50	0.41 ± 0.08	3
140	0.72 ± 0.10	10

Table 5.4: Ratio of the transported charges of the second and third exponential decay components.

The ratio of Q_2 and Q_3 at 0 mV was calculated and the results summarized in Table 5.4. The increase of Q_2/Q_3 at high sodium concentrations is a measure for the redistribution of the transferred charge that was described above. In measurements by Grimm *et al.* the ratios came to 0.16 and 0.74 at low and high sodium concentrations, respectively [60], which is in agreement with the present results.

5.2 pH Dependence of Outward Proton Pump Currents

5.2.1 Continuous Illumination Measurements

In the absence of sodium (or lithium) ions KR2 reportedly converts into an outward proton pump [33]. In order to investigate the proton pump currents, intracellular pH values were varied and the NaCl in bath and pipette solutions was replaced by NMG-Cl, which has a similar osmotic activity. A residual sodium concentration of about 0.2 mM in the pipette solutions was determined by atomic absorption spectroscopy. The continuous illumination of the KR2 expressing NG108-15 cells evoked outward pump currents as described earlier (Figure 5.1). The potential dependence of the steady-state current densities I_{ss}/C_{cell} at an extracellular pH of 7.4 and varying intracellular pH values is shown in Figure 5.7 A. At intracellular pH 5 and 6 a linear voltage dependence of the photocurrents was observed. Extrapolating to the potential of zero current yielded apparent potentials E_0 that are summarized in Table 5.5.

IC pH	E_0 in mV	n
5	-186 ± 30	9
6	-152 ± 24	11

Table 5.5: Apparent potentials of zero current E_0 derived from fits of the linear voltage dependence of the steady-state current densities I_{ss}/C_{cell} from Figure 5.7 A. The extracellular pH was kept at 7.4 while the intracellular pH was varied. The results are shown as mean ± SD.

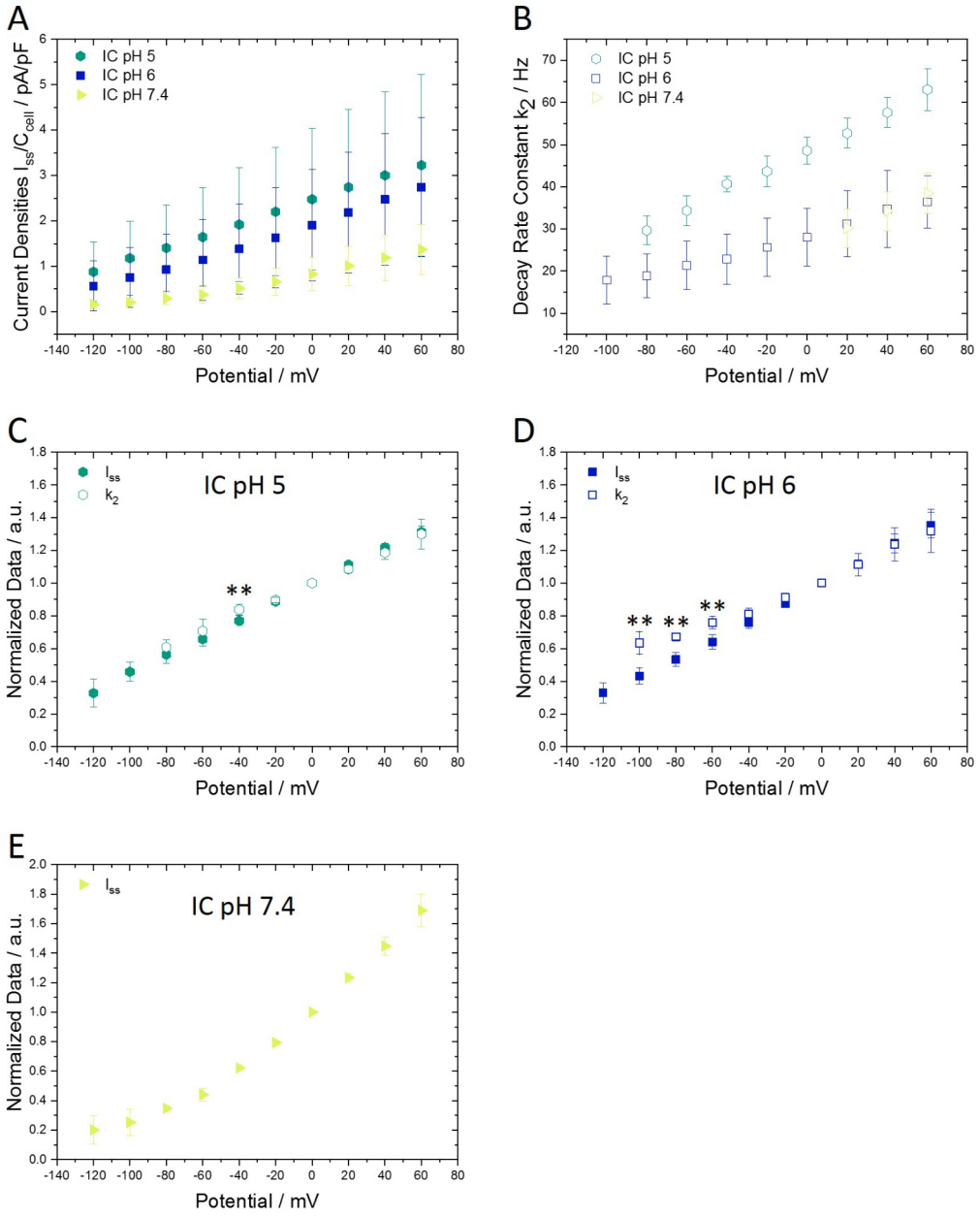

Figure 5.7: pH dependence of whole-cell patch clamp measurements on KR2 expressing NG108-15 cells in response to continuous 532 nm illumination in the absence of sodium. The intracellular pH was changed while the extracellular pH was kept at 7.4. (A) Potential dependence of the steady-state current densities with n = 9 (IC pH 5), n = 11 (IC pH 6) and n = 6 (IC pH 7.4). (B) Slow decay rate constant k_2 of the steady-state photocurrents with n = 5 (IC pH 5), n = 4 (IC pH 6) and n = 2 (IC pH 7.4). The steady-state currents and decay rates for the intracellular pH 5 (C), 6 (D) and 7.4 (E) were normalized to the value at 0 mV. ** indicate a significant difference with $p < 0.01$.

The changed pH gradient across the membrane caused a significant E_0 shift of 34 mV that is smaller than the expected 59 mV derived from thermodynamic principles. In the case of an intracellular pH of 7.4 the linearity is only observed at more positive potentials, whereas the current densities decrease in a non-linear fashion at more negative potentials. This behavior can also be seen in the normalized steady-state photocurrents in Figure 5.7 E. Assuming that a reversal of the KR2 photocurrents and an inversion of the photocycle cannot occur, a non-linear but monotonous decrease of the currents with more negative potentials can be expected similar to BR [76].
The slow decay rate constants k_2 of the steady-state photocurrents were analyzed and depicted in Figure 5.7 B. A linear dependence of the decay rate constants on the membrane potential can be observed at intracellular pH 5 and 6. Due to the small signal sizes at intracellular pH 7.4 only few cells at positive potentials could be evaluated. The correlation of the I_{ss} and k_2 potential dependence was checked by analyzing the normalized data in Figure 5.7 C and D for IC pH 5 and 6, respectively. At IC pH 5 a correlation could be observed between the kinetics and photocurrents. Therefore, it can be assumed that the kinetics of the rate limiting step mainly cause the potential dependence of the steady-state photocurrents. At IC pH 6 differences were observed at more negative potentials with a weaker potential dependence of the rate constant k_2. Nevertheless, the potential dependence of I_{ss} can predominantly be attributed to the kinetic limitation at pH 6.
Looking at the decay rate constants in Figure 5.7 B a significant increase of k_2 can be observed at all potentials lowering the intracellular pH. At 0 mV k_2 amounts to 28 ± 7 Hz at IC pH 6 versus 49 ± 3 Hz at IC pH 5. The rate-limiting step in the photocycle is dependent on the intracellular pH value with an acceleration of the associated transition at low pH.

5.2.2 Laser Flash Illumination Measurements

The single turnover experiments in the absence of sodium led to similar transient peak currents as described earlier in the presence of sodium (compare Figure 5.4). The current decay was analogously fitted with a three step exponential decay function in measurements were the intracellular pH was varied. While the first component was again not properly resolved, the potential dependences of the rate constants from step two and three were plotted in Figure 5.8 A and B. Due to the small signals obtained at a symmetrical pH of 7.4, only values at more positive potentials could be evaluated. The second rate constant $1/\tau_2$ does not show a clear dependence on the applied membrane potential or the intracellular pH (Figure 5.8 A). Values range between 1 and 1.5 kHz for $1/\tau_2$. $1/\tau_3$ shows a linear potential dependence with increasing rates at more positive potentials (Figure 5.8 B). The decrease of the intracellular pH value leads to an increase of the rates. At 0 mV $1/\tau_3$

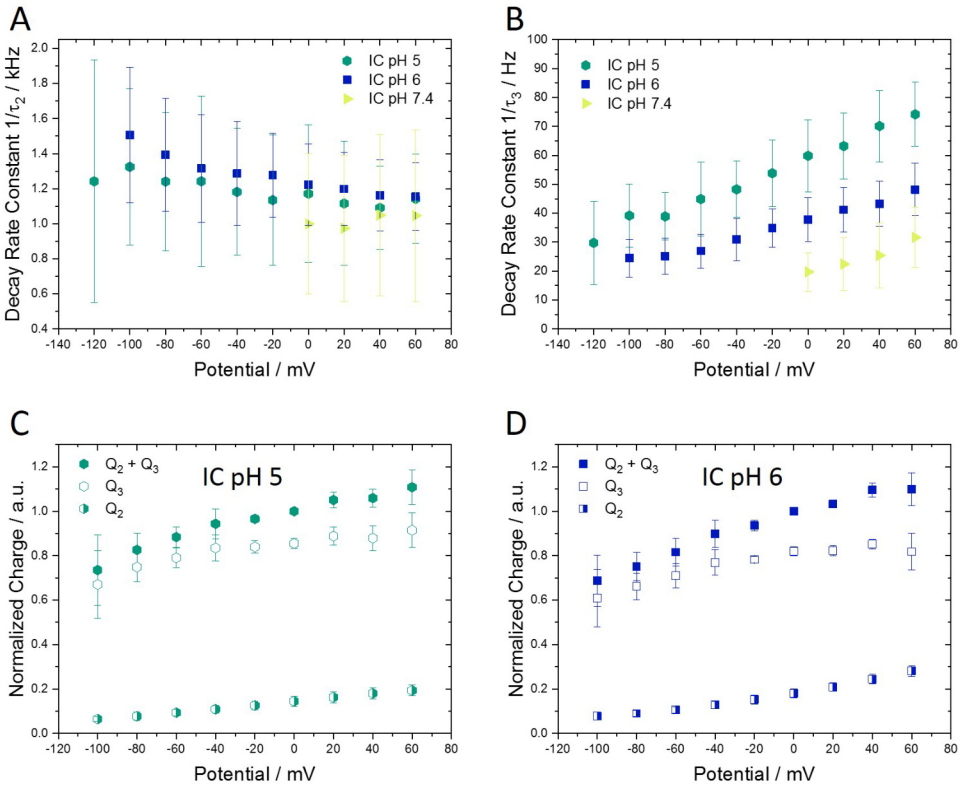

Figure 5.8: Potential and intracellular pH dependence of the KR2 single turnover rates and relative charge displacements. NG108-15 cells were illuminated with a $\geq$ 10 ns light pulse of 530 nm at symmetrical 140 mM NMG-Cl conditions. The intracellular pH was changed while the extracellular pH was kept at 7.4. The decay of the transient single turnover photo current was fitted with three exponential components. (A & B) Potential dependence of the rate constants of the second and third component $1/\tau_2$ and $1/\tau_3$. (C & D) Relative charge transported by the second and third exponential decay component normalized to the value of Q_2+Q_3 at 0 mV. The means of n = 7 (IC pH 5), n = 5 (IC pH 6) and n = 5 (IC pH 7.4) cells were evaluated.

increases from 20 ± 7 Hz at pH 7.4, over 38 ± 8 Hz at pH 6 to 60 ± 12 Hz at an intracellular pH of 5. The rates are significantly different from one another at the $\alpha < 0.05$ level.
The potential dependence of the relative charge associated to the second and third decay components was depicted in Figure 5.8 C and D. As described earlier, the major share of the charge is made up of Q_3 at intracellular pH 6 and low sodium concentrations (compare with Figure 5.6). The same is true when the intracellular pH is lowered to 5 (Figure 5.8 C) which can also be seen looking at the Q_2/Q_3 ratio that is 0.17 ± 0.03 at 0 mV.
In agreement with the continuous illumination measurements an acceleration of the slowest electrogenic transition in the photocycle could be observed. The clear dependence on the intracellular pH in indicates the conversion of KR2 to proton transport.

5.3 pH Dependence of KR2 Pump Currents in the Presence of Sodium

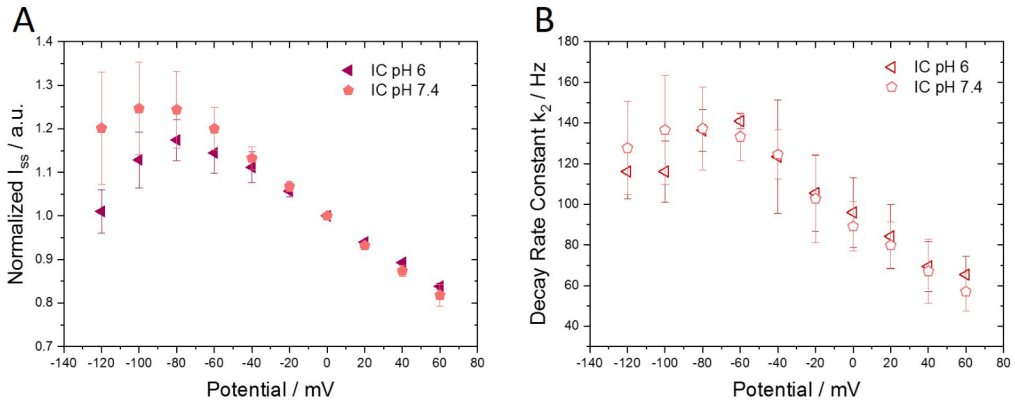

Figure 5.9: pH dependence of KR2 photocurrents in the presence of sodium. Intra- and extracellular solutions contained 140 mM NaCl and the extracellular pH was kept at 7.4 while the intracellular pH was changed. (A) Potential dependence of the normalized steady-state photocurrents from continuous 532 nm illumination. (B) Slow decay rate constant k_2 fitted into the steady-state photocurrent decay after the illumination. The means of n = 3 (IC pH 6) and n = 8 (IC pH 7.4) cells were evaluated.

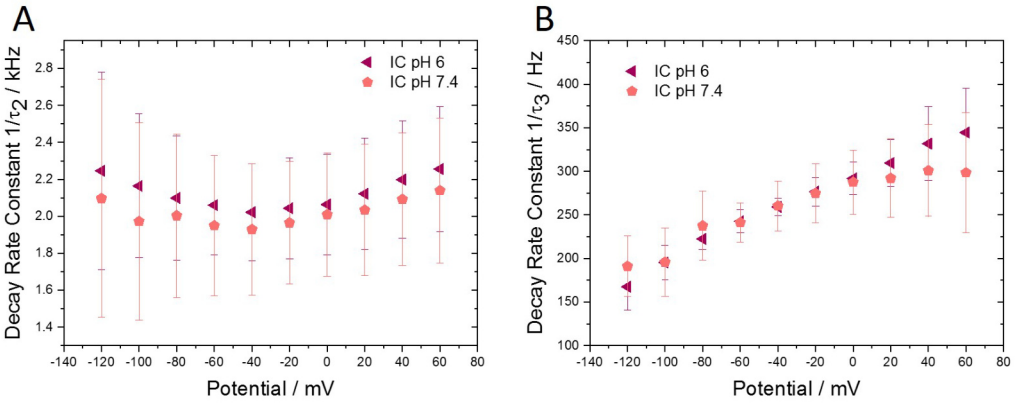

Figure 5.10: Potential and intracellular pH dependence of the KR2 single turnover rates in the presence of 140 mM NaCl. The extracellular pH was kept at 7.4. The means of n = 10 (IC pH 6) and n = 12 (IC pH 7.4) cells were evaluated.

Changing the intracellular pH in the absence of sodium (IC pH < 0.2 mM) showed significant changes in the kinetics of the rate-limiting transition of the photocycle. The influence of the intracellular pH in the presence of sodium was investigated at an intra- and extracellular sodium concentration of 140 mM while the extracellular pH was kept

at 7.4. In continuous illumination experiments the 0 mV current densities of the steady-state photocurrents were 2.1 ± 0.7 (n = 6) and 2.3 ± 1.8 (n = 11) at an IC pH of 6 and 7.4, respectively. The potential dependence of the normalized steady-state currents and the slow off kinetics is shown in Figure 5.9. An influence of the intracellular pH on the potential dependence of the steady-state currents cannot be concluded. Only minor deviations at very hyperpolarizing potentials can be observed. The decay rate constants of the steady-state currents in Figure 5.9 B further confirm that the intracellular pH has no influence in the presence of high sodium concentrations.

Looking at the single turnover transient photocurrents a similar conclusion can be drawn. The decay rate constants $1/\tau_2$ and $1/\tau_3$ of the second and third decay components are independent of the intracellular pH.

6 Discussion Part II: Characterization of KR2

The application of KR2 as an optogenetic tool requires a good membrane expression which is rather poor for the KR2 wild type in mammalian cells [57,60,137]. In order to optimize the membrane expression for the present work common strategies were tested like the addition of targeting sequences [107]. Sufficient membrane expression levels for the characterization could be obtained using a construct that includes a P2A self-cleaving peptide sequence [108] that separates KR2 from the fluorescent protein (Figure 2.1).
KR2 was electrophysiologically characterized to gain further insights into the sodium and proton pump mechanism. In order to study the active transport of Na^+ and H^+, KR2 was heterologously expressed in NG108-15 cells and measured in patch clamp experiments. For the identification of the electrogenic steps of the photocycle, single turnover measurements with nanosecond laser flash illumination were performed. The results and their implications for the pump mechanism are discussed in the following.

6.1 Sodium Transport

Outward pump currents were triggered under continuous illumination similar to measurements in other cell lines [59,60]. The active character of the transport can be concluded from the absence of current inversion at all applied potentials (Figure 5.2) and the determined apparent potentials of zero current E_0 that are strongly hyperpolarizing (Table 5.2). Under the conditions in Figure 5.2 passive Na^+ currents would lead to a current inversion at 0 mV. The proton gradient due to the intracellular pH 6.0 and the extracellular pH 7.4 would lead to a zero current potential of −83 mV after Nernst assuming passive proton transport which was considerably exceeded with −174 mV at an intra- and extracellular NaCl concentration of 5 mM.
Increasing the sodium concentration of the surrounding medium lead to an increase of the decay rate k_2 (Figure 5.2 B) which indicates that the limiting transition in the cycle is accelerated by the presence of sodium. Due to the acceleration of the step it is concluded that sodium uptake from the intracellular is the limitation. Only recently a structural

study of the KR2 O intermediate identified a Na^+ inside the protein [138] confirming that KR2 is indeed a Na^+ pump and not for example a proton pump that is stimulated by sodium ions.

In continuous illumination measurements, the sodium concentration has a distinctive influence on the shape of the potential dependence of the pump currents. Kato *et al.* reported a potential independence of the steady-state photocurrents [59] and Grimm *et al.* found linear potential dependencies with positive and negative slopes in a confined potential range [60]. Here, at low sodium concentrations a linear potential dependence can be observed similar to IV curves that were found in other ion pumps like BR [75, 76] and proteorhodopsin [131]. At 25 mM intra- and extracellular NaCl concentration a saturation like behavior can be observed at depolarizing potentials but higher concentrations lead to a bell-like shape (Figure 5.2). The relative decrease of the steady-state currents at depolarizing potentials might be explained by a potential dependent amount of protein that does not contribute to the current anymore due to e.g. a trapping in a photocycle intermediate. Since the potential dependencies of the steady-state currents and the decay rate constants k_2 correlate (Figure 5.3), this possibility is excluded. In general, the steady-state currents in KR2 seem to be kinetically limited. If the potential dependence of the currents is ruled by the kinetics of a single potential dependent reaction, it may be accelerated till it saturates at high depolarizing potentials. The negative slopes in the IV curves suggest that more than one reaction step is involved and that at least one of those has a reverse potential dependence [139]. With more positive potentials such a reaction step might decelerate and take the place of the sodium uptake as the new rate-limiting step.

A reaction step that might become rate-limiting is the extracellular Na^+ release which should decelerate with higher NaCl concentrations. This could lead to a self-blockade for Na^+ transport that may instead be compensated by proton transport that works at a lower rate. Another possibility might be that the transition that becomes rate-limiting is ruled by the thermal reisomerization of the retinal chromophore that could only occur when the Na^+ leaves the cavity close to the retinal Schiff base. A potential dependence of the reisomerization is imaginable if the position of the N-H dipole changes in the electric field.

For the Na^+/K^+-ATPase a negative slope of the IV curve at positive potentials was found at low extracellular K^+ concentrations [140]. A potential dependent K^+-binding step was suggested to be involved in the pump mechanism [140]. In the sodium pump GLR, H^+ release and uptake steps were suggested to take place during the sodium pump cycle [52]. In KR2, similar charge transfer/binding steps might account for the observed steady-state potential dependence.

6.2 Proton Transport

In *E. coli* assays, KR2 was reported to pump protons in the absence of Na^+ and Li^+ [33], but expressed in neuronal ND7/23 cells no systematic dependence of the pump currents on the intracellular pH could be detected [60]. The proton transport and its dependence on the intracellular pH was investigated in continuous illumination measurements. Due to the reduced current amplitudes in sodium "free" measurements, the measurable conditions were limited and a residual Na^+ concentration of ∼0.2 mM in the pipette solution remained. Nevertheless, a distinct acceleration of the decay rate k_2 could be observed at an intracellular pH of 5 compared to IC pH 6 and 7.4 (Figure 5.7 B). The apparent potential E_0 was significantly shifted to more hyperpolarizing potentials when the IC pH was lowered (Table 5.5). This indicates that the measured steady-state currents under this conditions were carried by proton transport to a non-negligible degree.
Similar to the low sodium measurements, a linear potential dependence of the steady-state currents was observed and the overall correlation to the decay rate constant k_2 (Figure 5.7 C and D) suggests that for the proton transport the steady-state currents are kinetically limited as well.
At high sodium concentrations, an influence of the intracellular pH could not be determined (Section 5.3) which suggests that at 140 mM NaCl the steady-state photocurrents are mainly carried by sodium pumping and the proton transport is insignificant.

6.3 Electrogenic Steps of a Single Turnover

In measurements where the KR2 expressing cells were only illuminated by a nanosecond light pulse, the photocycles of the excited proteins are synchronized and only run trough a single cycle. The kinetic analysis of the KR2 induced photocurrent transients identified three electrogenic steps that occur under high and low sodium conditions (Figure 5.4 B and Section 5.2.2). Three electrogenic steps were also reported in other cell lines and systems with time constants that are in agreement with the present data [60, 141].
For the second time constant τ_2 in the range of ∼ 0.4-1 ms, no systematic dependence on the sodium concentration could be determined which indicates that the associated transition is not involved in the displacement of Na^+ ions (Figure 5.5 A). The independence of τ_2 on the intracellular pH under sodium "free" conditions (Figure 5.8 A) also suggests that no proton is taken up with this time constant. From the results, it can be concluded that the second electrogenic step does not describe the translocation of the transported ion. Another charge transfer has to be accountable for τ_2. A proton transfer between the retinal Schiff base and D116 might be a possible source. Looking at the relative positions

of the retinal Schiff base and the acceptor D116 [63] (Figure 1.7), only a small contribution to the overall charge transfer would be expected. The transfer of a compensatory charge as observed in GLR [52] could be another reason for an observed electrogenic step that is not connected to the translocation of the transported ion. Under the different ionic conditions, the applied membrane potential did not show a clear influence on τ_2. A charge transfer in an electric field would be expected to be accelerated or decelerated in response to membrane potential changes. Possibly the transition is limited by another process that is potential independent like the reisomerization of the retinal or a conformational change which could also contribute to a net charge transfer if a charged residue is moved in the electric field.
The third electrogenic step is described by the time constant τ_3 which ranges between ~ 3 and ~ 50 ms (Figure 5.5 B and 5.8 B). It is accelerated by the increase of the surrounding sodium concentration, the decrease of the intracellular pH and more positive membrane potentials. These findings suggest that the associated charge transfer step includes the uptake of the transported ion from the intracellular bulk.

For the transported charge in a single turnover, it is assumed that only a single charged ion is transported across the membrane from the intracellular to the extracellular under all experimental conditions. The relative transported charges Q_2 and Q_3 attributed to the time constants τ_2 and τ_3, respectively, show a distinct dependence on the applied membrane potential and the surrounding Na^+ concentration (Figure 5.6). At 0 mV the ratio Q_2/Q_3 increases with the amount of surrounding Na^+ (Table 5.4) which might be understood if the distance of charge displacement was dependent on the sodium concentration. Similarly, the displacement distance would have to be dependent on the applied membrane potential. This would mean that the sodium ion does not bind to a certain position but can be located in various continuous depths in the protein which is considered to be rather unlikely.
Another possible explanation for the observed sodium ion and potential dependence of Q_2/Q_3 might be a charge displacement of a positive charge that is not transported similar to the compensatory proton uptake and release suggested for GLR [52]. The shift of a compensatory charge transfer from an earlier to a later transition in the photocycle might account for the observed relative increase of Q_2 and reduction of Q_3. A more detailed description of this suggestion is given with the assignment to the photocycle intermediates below.

6.4 Assignment of Electrogenic Steps to the KR2 Photocycle

The assignment of the electrogenic steps to the transitions of the KR2 photocycle in Figure 1.8 leads to discrepancies that are discussed in the following. Looking at the transition kinetics from the flash photolysis data on KR2 reconstituted into lipid bilayers at 100 mM NaCl the L/M to O and O to KR2 transitions occur with time constants of 1.0 and 7.9 ms, respectively [33] (Figure 1.8). The second and third electrogenic steps with $\tau_2 = 0.485$ ms and $\tau_3 = 3.4$ ms agree with the L/M to O and the O to KR2 transition kinetics. The slight acceleration in the present data could be explained by different experimental conditions in NG108-15 cells and 140 mM NaCl. The first electrogenic step that is compromised by the time resolution in cells could be assigned to an earlier transition like K to L/M. In the flash photolysis data the O rise was significantly accelerated in the presence of sodium, therefore, the sodium uptake from the extracellular was assigned to the L/M to O transition [33]. This strongly contrasts with the sodium dependence of the electrogenic steps in the present work. The second electrogenic step does not show a systematic dependence on the sodium concentration while the third one is significantly accelerated by sodium.

In patch clamp single turnover experiments with a modified KR2 gene eKR2, Grimm *et al.* found similar sodium dependencies for the three electrogenic steps (Table 6.1), but nevertheless matched the second to the L/M to O transition [60]. They further discuss that according to theoretical calculations in the same transition a sodium ion is translocated past the retinal Schiff base [70], but do not explain the lack of the sodium dependent acceleration that was stated before [33].
Solid supported membrane (SSM) measurements of KR2 reconstituted in proteoliposomes were performed by J. Sörmann revealing three electrogenic steps in the photovoltage formation that are in agreement with the present data [141] (Table 6.1). Motivated by the above described discrepancies a new KR2 photocycle model was developed based on the electrophysiological data and flash photolysis measurements (done by P. Eberhardt, Wachtveitl Group, Goethe Universität Frankfurt) that were performed on the same samples. Close

	Patch clamp eKR2 110 mM NaCl pH 7.2	**SSM KR2 50 mM NaCl pH7.4**	**Patch clamp KR2 140 mM NaCl IC pH 6.0**
τ_1	160 μs	49 μs	-
τ_2	650 μs	470 μs	485 μs
τ_3	5.2 ms	5 ms	3.4 ms

Table 6.1: Time constants of electrogenic steps in KR2. Grimm *et al.* performed patch clamp current measurements on eKR2 expressing ND7/23 cells [60]. Photovoltages of KR2 reconstituted in proteoliposomes were measured on solid supported membranes by J. Sörmann [141].

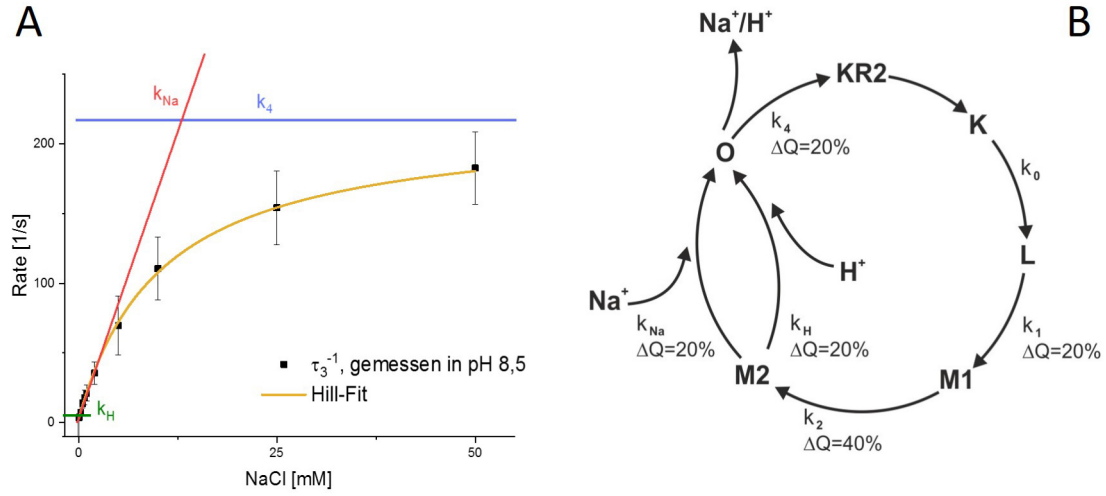

Figure 6.1: KR2 photocycle model proposed by J. Sörmann [141]. (A) Sodium dependence of rate $1/\tau_3$ at pH 8.5 (titration from KCl to NaCl). k_{Na} is determined by a linear fit at low sodium concentrations of 0-2 mM NaCl. The intersection of the linear fit with the Y-axis defines k_H. The data is fitted with a Hill equation that gives a saturation rate which defines k_4. (B) Photocycle model with charge transfer percentages at pH 8.5 and 0 mM NaCl. The rates are k_0 = 50 kHz, k_1 = 20.4 kHz, k_2 = 2.1 kHz, k_{Na} = 16.6·[NaCl] Hz·mM^{-1}, k_H = 5 Hz and k_4 = 217 Hz.

comparison of the transition kinetics revealed that the second electrogenic step takes place during the M intermediate which lead to the introduction of two M intermediates M1 and M2 (Figure 6.1 B). Based on the sodium ion dependence of the third electrogenic step, two competitive rate constants k_{Na} and k_H and the pH and sodium independent rate k_4 were introduced (Figure 6.1 A) in order to account for the substrate dependent M to O and the final O to KR2 transitions from the spectroscopic data (Figure 6.1 B).

Analyzing the present data by the same method (Figure 6.2) yielded similar rate constants as determined by the SSM measurements (Table 6.2). The relative transported charge of the second and third electrogenic steps derived from the SSM data showed a dependence on

	SSM KR2 NMG-Cl → NaCl pH 6.0	**Patch clamp KR2 NMG-Cl → NaCl IC pH 6.0**
$\mathbf{k_{Na}}$	4.4·[NaCl] Hz·mM^{-1}	(9 ± 2)·[NaCl] Hz·mM^{-1}
$\mathbf{k_H}$	23 Hz	39 ± 6 Hz
$\mathbf{k_4}$	307 Hz	328 ± 45 Hz

Table 6.2: Rates derived from the sodium dependence of $1/\tau_3$ in SSM [141] and patch clamp measurements.

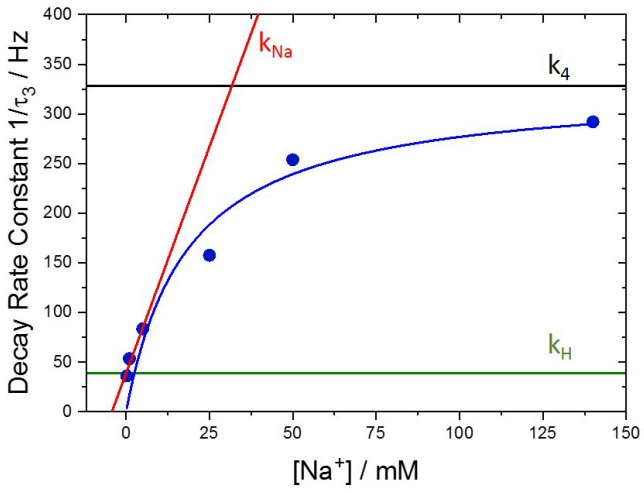

Figure 6.2: Sodium dependence of the rate $1/\tau_3$ of the third electrogenic step in single turnover measurements at 0 mV (blue dots). The data was fitted with a Michaelis-Menten equation (blue line) and a linear function between 0 and 5 mM NaCl (red line). The rate constants k_H, k_{Na} and k_4 were derived as described in Figure 6.1.

the sodium concentration [141]. In the absence of sodium, step two and three are declared to contribute equally with 40% of the overall transported charge (Figure 6.1 B). The contribution of the second step rises with increasing NaCl concentrations while the third steps contribution decreases. The observations are explained by the sodium dependent acceleration of the rate k_{Na} that becomes faster, shifting a part of the transported charge of the M2 decay to the earlier M1 to M2 transition. The ratio of the transported charge in step two and three Q_2/Q_3 showed a qualitatively similar sodium concentration dependence with ratios of 0.16 and 0.72 at 1 mM and 140 mM NaCl, respectively (Table 5.4). The results quantitatively contrast the SSM data, but agree with the findings of Grimm *et al.* who determined ratios of 0.16 (1 mM NaCl) and 0.74 (110 mM NaCl) at pH 7.2 [60]. As mentioned earlier Q_2/Q_3 also shows a membrane potential dependence in addition to the sodium dependence that might be explained by introducing a compensatory charge transfer to the photocycle in Figure 6.1 B.

In Figure 6.3 a reduced KR2 photocycle with the suggested charge transfers is depicted. Upon light absorption the KR2 ground state is excited and the retinal chromophore isomerizes from the all-*trans* to the 13-*cis* form. After passing through the early intermediates the retinal Schiff base is deprotonated with a proton transfer to Asp116 upon the M1 formation which could account for the compromised first electrogenic step. The kinetics of the second electrogenic step $1/\tau_2$ are assigned to the M1 to M2 transition. Due to the potential and substrate independence of the kinetics, the transition is suggested to be ruled

by a conformational change of the protein [142] that might also be responsible for part of the charge transfer signal during this transition. Upon M2 decay, the retinal Schiff base is reprotonated from Asp116 and a Na^+ ion is taken up into the cavity that is surrounded by Asp116, Asn112 and Leu74 (Section 1.4.1). The rate k_{Na} is assigned to this transition. The final O to KR2 transition is accompanied by Na^+ release to the extracellular lumen with the rate k_4. In this scheme, the relative charge transfers Q_2 and Q_3 determined in the single turnover measurements are attributed to the M1 to M2 and the M2 to O to KR2 transitions. It is suggested that a compensatory H^+ release and uptake take place during the photocycle. At more positive potentials, the M1 to M2 transition might be accompanied by a proton release to the extracellular.
A proton would be taken up again upon O decay from the same side resulting in no net proton transport. At more negative potentials, the release of the proton might be decelerated leading to a later release of the proton during the M2 to O transition. This would explain the potential dependence of Q_2 as well as the relatively high share of charge transport compared to Q_3 since in Q_3 an inversed charge transport would take place masking part of the outward charge movement.

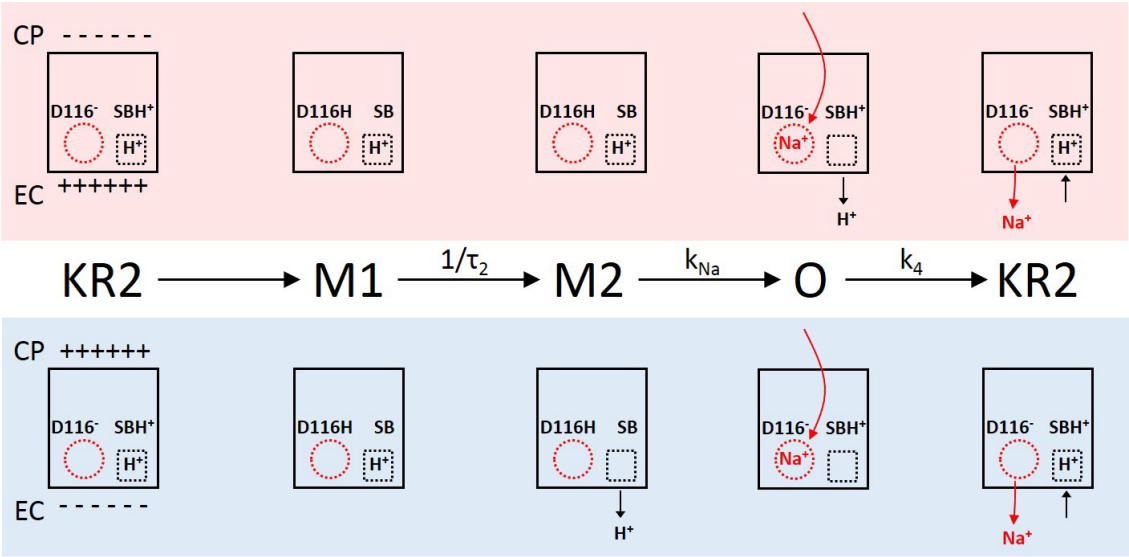

Figure 6.3: Reduced KR2 photocycle scheme for Na^+ transport with membrane potential dependence of a compensatory H^+ release and uptake.

6.5 Potential Dependence in Continuous Illumination and Single Turnover Measurements

In single turnover experiments, the excited proteins pass through the photocycle once and the slowest transition limits the speed of the cycle. The limiting electrogenic step in the present work has the rate $1/\tau_3$ which is linearly dependent on the membrane potential under all conditions (Figure 6.4 filled symbols). Under continuous illumination, the proteins are repeatedly excited and a steady state is reached with temporally constant populations of each intermediate of the photocycle. When the light is turned off, the excited proteins that can populate different states complete their cycle. In this process the slowest current decay k_2 describes the rate limiting step of the pump turnover. The potential dependence of k_2 is strongly dependent on the sodium concentration (Figure 6.4 A empty symbols) with a negative slope occurring at high NaCl concentrations. As suggested above, a compensatory proton uptake from the extracellular lumen in the O to KR2 transition (Figure 6.3) might have an inverse potential dependence becoming the rate limiting step at more positive membrane potentials. In single turnover experiments, the suggested proton uptake would have no influence on the membrane potential dependence of $1/\tau_3$. In order to clarify this discrepancy more experiments are needed.

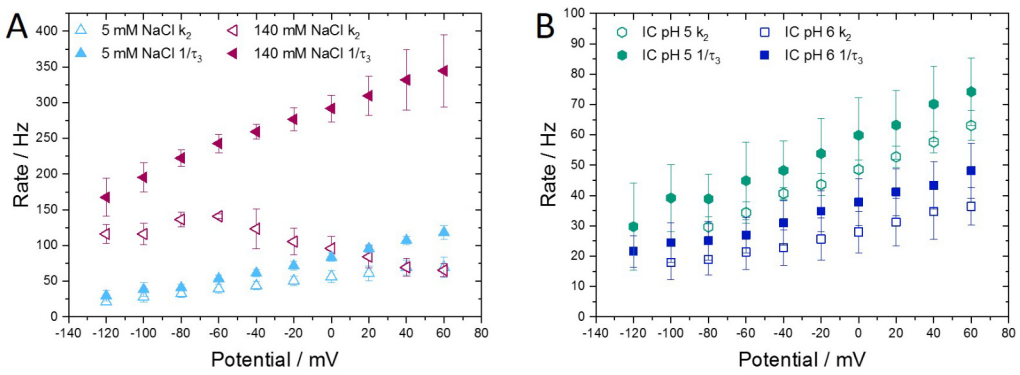

Figure 6.4: Membrane potential dependence of the slow decay rate constant k_2 in continuous illumination measurements (empty symbols) and the rate of the third electrogenic step $1/\tau_3$ in single turnover experiments (filled symbols). (A) Symmetrical NaCl concentrations and IC pH 6 and EC pH 7.4. (B) A residual IC sodium concentration of ∼0.2 mM and an EC pH of 7.4.

Upon changing the intracellular pH linear potential dependences were observed when illuminated continuously or by a light flash (Figure 6.4 B). Either the effect could not be observed because the substrate uptake was still rate limiting or the mechanism of proton transport in KR2 differs and maybe can do without a compensatory charge transfer at

the extracellular side. Then the retinal Schiff base would be simply reprotonated from the intracellular upon the M2 decay and the D116 proton is released in the final O to KR2 transition.

For the further investigation of the KR2 pumping mechanism, patch clamp measurements with sodium gradients would be of interest in order to elucidate the influence of the intra- and extracellular sodium concentrations on the photocurrents and their membrane potential dependence. In order to test the suggested compensatory H^+ transfer one could lower the extracellular pH under sodium conditions and check whether the rate-limiting step in continuous illumination measurements was accelerated. Mutating putative proton binding sites at the extracellular might similarly give further insights.

7 Results Part III: Optochemokine Tandems

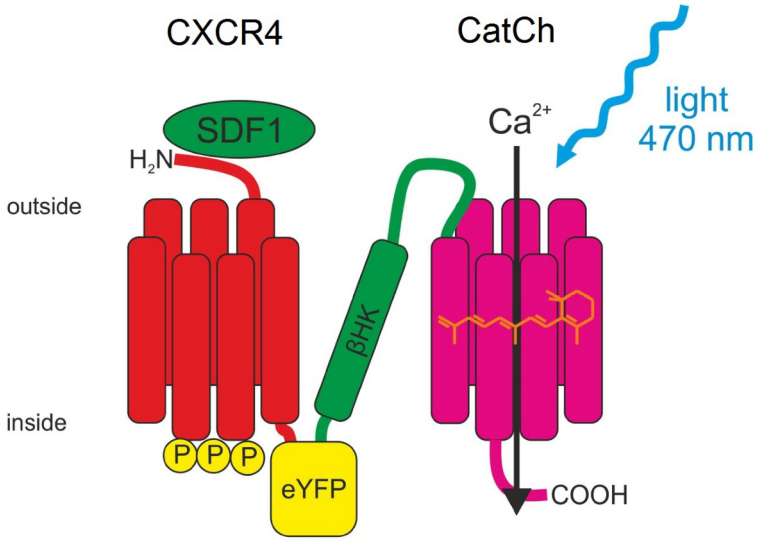

Figure 7.1: Scheme of an optochemokine tandem. The CXCR4 receptor is placed at the N-terminus and C-terminally followed by eYFP, the β helix of the rat gastric H^+, K^+-ATPase β subunit [110] and the cation channel CatCh [112]. Image altered from [111].

In optochemokine tandems [111] microbial rhodopsins are combined with a chemokine receptor in a functional tandem protein (Figure 7.1). In the following sections two tandem proteins are described: tCXCR4/CatCh and tCXCR4/Arch. Both utilize the CXCR4 receptor [105] that internalizes upon activation with its agonist SDF1 [96] which also displaces the light-gated tandem partner into the intracellular lumen enabling a potential intracellular light-activation of the tandem partner. The microbial rhodopsins used are the channelrhodopsin 2 [4] mutant ChR2(L132C) (CatCh) [112], an inwardly rectifying cation channel with increased Ca^{2+} permeability compared to the wild type, and the outward proton pump Arch [113]. The optochemokine tandems tCXCR4/CatCh and tCXCR4/Arch potentially allow the generation of Ca^{2+} and proton permeability in cell organelles, respectively.

7.1 Electrophysiological Monitoring of tCXCR4/CatCh Internalization

In order to study the conserved functionality of CatCh in the tandem, tCXCR4/Catch was heterologously expressed in NG108-15 cells and the photocurrents were measured in whole-cell patch clamp experiments. Cells were illuminated at 473 nm under saturating light conditions. In Figure 7.2, the typical signals of cells expressing tCXCR4/CatCh or CatCh::eYFP were depicted. A typical CatCh signal [112] could be observed in both cases. Upon illumination at −100 mV applied membrane potential a transient current peak appears that is followed by a stationary current. Stationary photocurrents decay back to the dark current level after the end of the illumination period. The mean current densities measured at −100 mV in whole-cell configuration were -67 ± 19 pA/pF (n = 11) for tCXCR4/CatCh and -125 ± 30 pA/pF (n = 14) for CatCh (published in [111]). The functionality of CatCh in the tandem could be confirmed whereby in NG108-15 cells the level of expression of the tandem is reduced in comparison to CatCh::eYFP alone.

Measuring the CatCh photocurrents in patch clamp experiments further allows the monitoring of the tCXCR4/CatCh internalization. In cell-attached configuration the same pipette and bath solutions were used whereas the pipette solution was attributed with 50 nM of the CXCR4 agonist SDF1β. Despite smaller signals the cell-attached configuration is advantageous since it conserves the cytosolic composition and avoids any negative effects on the internalization process. The bath solution was kept at a temperature of about 34 °C and the light-triggered CatCh signals were measured every 2 min at −100 mV membrane potential. In Figure 7.3 A the signals from cell-attached measurements can be

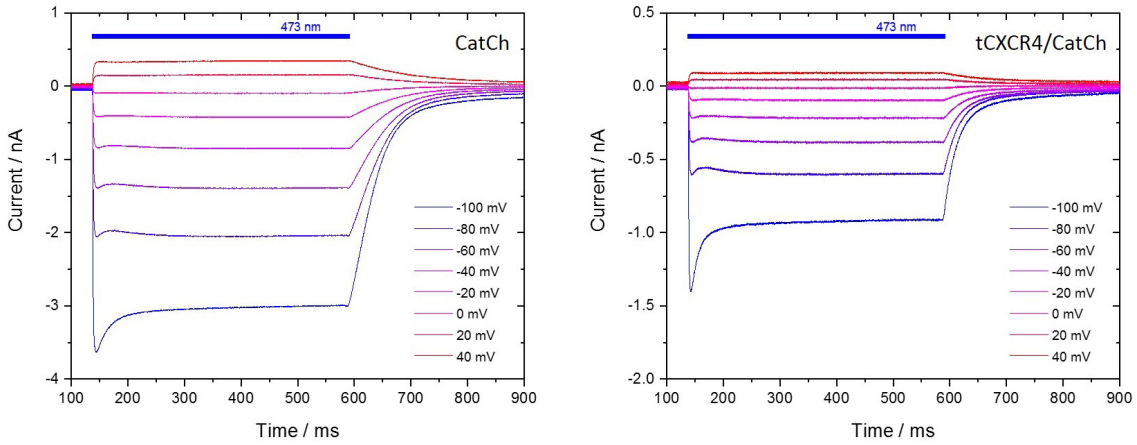

Figure 7.2: Patch clamp measurements on tCXCR4/CatCh and CatCh::eYFP expressing NG108-15 cells. Cells were illuminated at 473 nm and measured in whole-cell configuration.

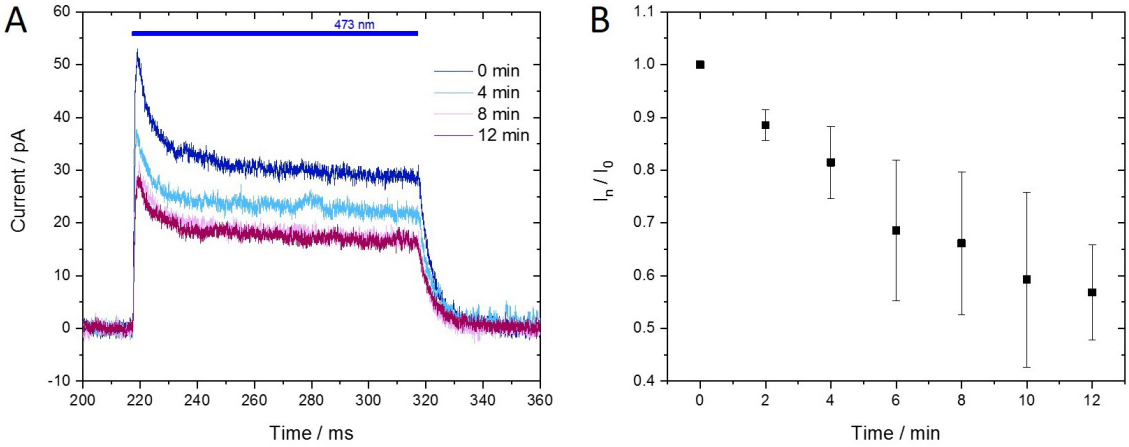

Figure 7.3: Patch clamp investigation of tCXCR4/CatCh at 34°C in the presence of 50 nM SDF1β in the pipette solution. (A) Photo currents of tCXCR4/CatCh expressing NG108-15 cells measured in cell-attached configuration. Cells were illuminated at 473 nm and a membrane potential of 100 mV was applied (corresponds to −100 mV in whole-cell). Measurements were repeated every 2 min. (B) Time dependence of the relative tCXCR4/CatCh photocurrent in the presence of 50 nM SDF1β (n = 3 cells, mean ± S.D.). Data in B was published in [111].

seen as well as the time-dependent reduction of the current. The relative CatCh signals of tCXCR4/CatCh were reduced to about 57% of the original response in a time course of 12 min after forming the gigaseal. The reduction of the signal is attributed to the SDF1β induced internalization of the optochemokine tandem that leads to less CatCh proteins in the membrane that can contribute to the photocurrent.

7.2 Confocal Laser Scanning Microscopy of tCXCR4/Arch Internalization

The internalization of the optochemokine tandem tCXCR4/Arch expressed in HeLa cells was imaged by confocal laser scanning microscopy (CLSM). It is assumed that tCXCR4/Arch was expressed in one functional entity which was shown for previously described tandem proteins [110, 111]. The YFP fluorescence depicted in Figure 7.4 A and B represents the localization of tCXCR4/Arch that can be found in the cell membrane as well as in intracellular vesicles. In order to visualize the tCXCR4/Arch internalization into endosomes, the cells were treated with a functional CXCR4 specific antibody labeled with red-fluorescent dye (Anti-Mouse CD 184 PE-eFlur 610) for 30 min. Internalization was triggered or blocked by adding the agonist SDF1α or the antagonist AMD3100 to the medium for 45 min.

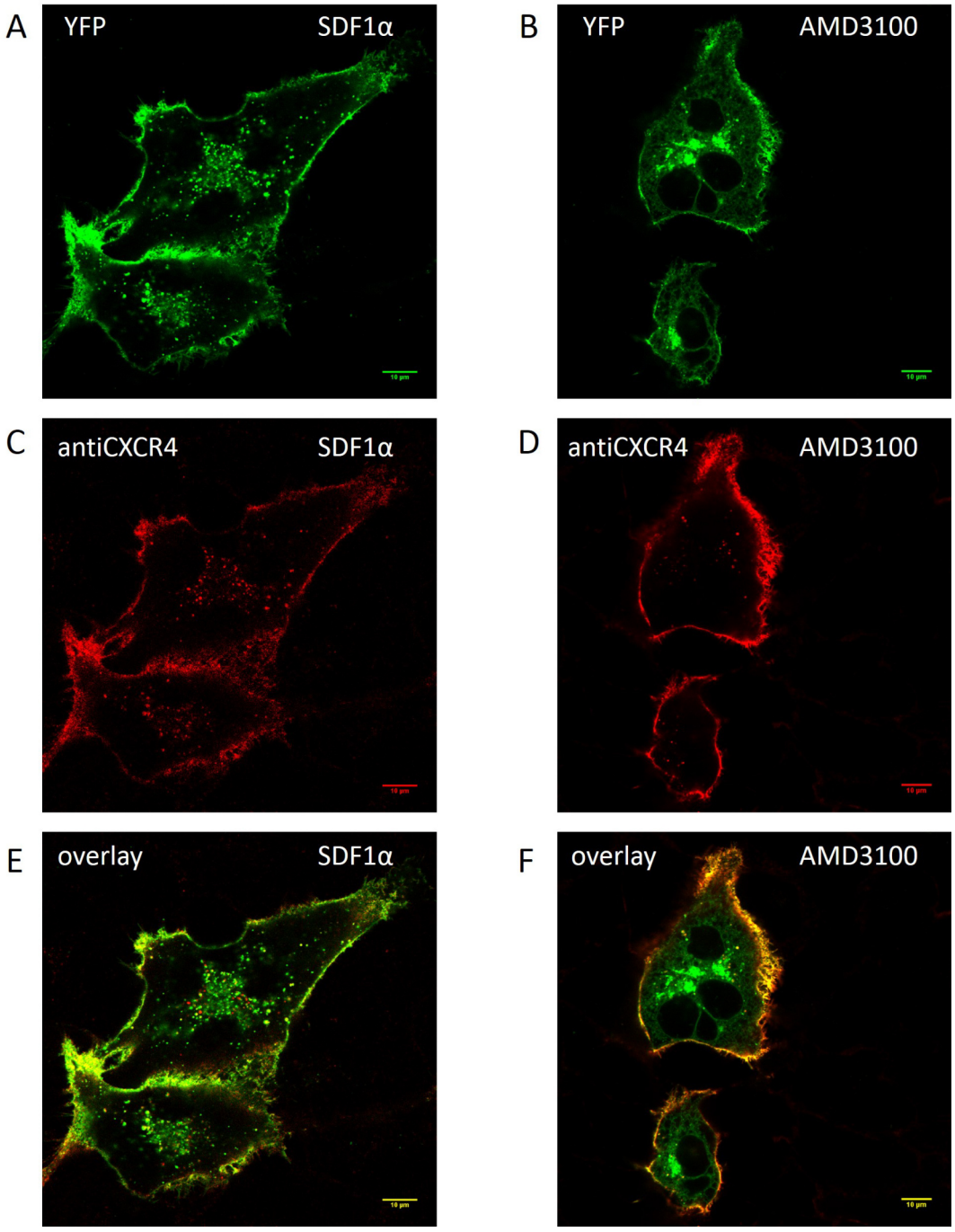

Figure 7.4: Confocal laser scanning micrographs of tCXCR4/Arch expressing HeLa cells. Z-stack overlays of typical tCXCR4/Arch cells treated with 50 nM SDF1α for 45 min (A) or with 10 μM AMD3100 (B). (C and D) Internalization of the anti-CXCR4 antibody. Overlay of the fluorescence signals of tCXCR4/Arch and anti-CXCR4 after treatment with SDF1α (E) or AMD3100 (F). CLSM was performed in collaboration with Dr. U. Terpitz and J. Schlegel from the Julius Maximilian University, Würzburg.

After several hours of incubation the immuno-labeled CXCR4 was located not only in the cell membrane but also in intracellular vesicles (Figure 7.4 C and D). The number of vesicles was strongly reduced with AMD3100 (Figure 7.4 D) which accounts for the successful blocking of the CXCR4 activation [98]. The intracellular vesicles show both green and red fluorescence (yellow in overlay images in Figure 7.4 E and F) indicating that tCXCR4/Arch was indeed translocated from the cell membrane.
CLSM imaging of the successful internalization of tCXCR4/Arch directly shows the functionality of the CXCR4 receptor in the tandem cassette.

8 Discussion Part III: Optochemokine Tandems

The precise expression of optogenetic tools in intracellular compartments is a major challenge due to the absence of suitable targeting strategies. The optochemokine tandems described in this work provide the opportunity for light-activated manipulation of intracellular Ca^{2+} levels and pH using tandem proteins located in endosomes.

The electrophysiological measurements on tCXCR4/CatCh showed that CatCh is still fully functional in the tandem and the SDF1β-induced time-dependent decrease of the cell membrane CatCh signal indicates the internalization of the tandem due to CXCR4 activity. The signal decrease to 57% after 12 min of SDF1β exposure is in agreement with the CXCR4 internalization kinetics in other cell types [143, 144].

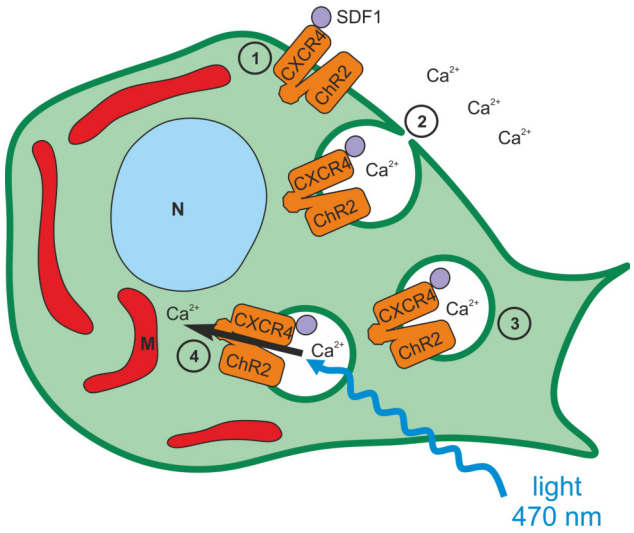

Figure 8.1: Scheme of the tCXCR4/CatCh function. (1) tCXCR4/CatCh is expressed and targeted to the cell membrane. The CXCR4 agonist SDF1 is bound and CXCR4 activated. (2) The tandem is internalized into endosomes with a higher Ca^{2+} concentration compared to the cytosol. (3) The endosomes migrate to the cells inside. (4) Blue light activation of CatCh leads to channel opening and a transient increase of the Ca^{2+} concentration. Increase of the second messenger concentration might trigger physiological processes. N: nucleus, M: mitochondrion. Image taken from [111].

The light-induced release of Ca^{2+} from tCXCR4/CatCh endosomes was demonstrated by Feldbauer *et al.* [111]. A schematic overview of the tCXCR4/CatCh function is given in Figure 8.1. Upon activation of the CXCR4 receptor by SDF1 binding, the tandem protein is internalized into endosomes that are filled with the solution from the extracellular lumen. The Ca^{2+} concentration is considerably higher in the extracellular lumen compared to the cytosol with $\sim$ 1 mM and 100 nM, respectively [145]. The endosomes naturally release Ca^{2+} to around 40 μM [145] and are simultaneously acidified [89, 146]. Blue light illumination of tCXCR4/CatCh opens the channel and releases Ca^{2+} from the 40 μM intraendosomal Ca^{2+} reservoir into the cytosol. The transient Ca^{2+} signal might trigger physiological processes like induction of gene expression, cell proliferation and cell death [16, 147, 148].

Imaging of the tCXCR4/Arch internalization showed the activation by SDF1 and the inhibition of the internalization with AMD3100. The functionality of Arch in the tandem was not verified, but assuming that the pump activity of Arch is conserved similar to the microbial rhodopsins in other tandems [110, 111], it would be possible to manipulate the intracellular pH with light as was done with an optogenetic tool in synapses [149]. In the endocytic pathway, vesicles are progressively acidified with early endosomes being least acidic and lysosomes reaching pH values as low as 4.5-4.7 [150]. Essential reactions depend on the changing pH of the endosomal compartments as the maturation from early to late endosomes [151] and uncoupling of ligands from receptors [150].

Further investigations on the functionality of the otpochemokine tandems are needed. Especially in respect to triggering cell biological processes, effects triggered by CXCR4 activation and tandem activity have to be distinguished. Introducing other GPCRs or mutations that alter the CXCR4 function [152] might be considered.

9 Conclusions and Outlook

The characterization of the inward proton pump NsXeR and the outward sodium ion pump KR2 by electrophysiological methods resulted in new insights into the pumping mechanisms of both.

NsXeR was heterologously expressed in NG108-15 cells for patch clamp measurements that showed that NsXeR actively transports protons against an electrochemical load confirming previous reports [32]. The proton transport is mainly kinetically limited and independent of the intracellular pH. In BLM photovoltage measurements on NsXeR reconstituted in proteoliposomes, three electrogenic steps and their contributions to the overall charge transfer were identified and assigned to transitions in the photocycle. The Schiff base reprotonation step has an unusual pH dependence with a deceleration at more acidic pH values. Also, the attributed charge transfer contribution is pH dependent which is explained by a delayed charge transfer at acidic pH values. In mutational studies, the importance and influence of the primary proton acceptor Asp220 that does not act as a counterion to the retinal Schiff base could be verified. In order to confirm the assumptions on the charge transfer steps, H_2O/D_2O exchange and FTIR measurements could give information on the protonation states of Asp220 and the putative proton donor Asp76 during the photocycle and the transitions that are related to proton transport steps.

For NsXeR a unique blue-light-effect was found which shows that the Schiff base can be reprotonated from both the intracellular and the extracellular side. A mechanism was proposed that explains the results based on a switch between the MI and MII intermediates and a potential sensitive equilibrium between both. The different nature of the accessibility switch of NsXeR compared to BR is suggested to be key to the pump vectoriality. The unique blue-light-effect in NsXeR might be exploited in optogenetic applications where the signal might be up- or down-regulated by additional blue light illumination. For that, experiments with continuous blue light illumination would be necessary. Apart from a possible application as a tool for neuronal excitation by cell depolarization, NsXeR could potentially also be applied in the field of acidosis-induced cell death in anticancer therapies [153].

In patch clamp measurements on KR2 expressing NG108-15 cells, sodium ion and proton transport by KR2 could be confirmed in continuous illumination experiments. The steady-state currents are kinetically limited and the potential dependence reveals the existence

of at least one reaction step with a reverse potential dependence. Three electrogenic steps were found in single turnover experiments and were assigned to the KR2 photocycle by application of a model developed by J. Sörmann [141]. A potential dependence for the ratio of the second and third charge transfer steps Q_2/Q_3 was found and a compensatory charge transfer was suggested in order to explain the experimental data. For further investigations and the confirmation of the proposed model, patch clamp experiments with different Na^+ and pH gradients would be of interest. KR2 could be a potential tool for neuronal silencing as the application of proton pumps and anion channels can lead to unexpected neurotransmitter release [154]. In line with that, studying the potassium pumping mutant KR2(N61PG263W) [59] would be promising.

The conserved operating of CatCh in the optochemokine tandem tCXCR4/CatCh was confirmed in patch clamp experiments. Further, the functionality of the CXCR4 internalization in the tandem was demonstrated by electrophysiological measurements and by CLSM imaging. The optochemokine tandems could be used for the study of various questions. The internalization kinetics of CXCR4 or other unknown GPCRs could be investigated by electrophysiological methods. Utilizing the SDF1 dependent internalization of CXCR4, CatCh may be activated intracellularly. The manipulation of the intracellular Ca^{2+} concentration by Ca^{2+} release from endosomes in a specific spatiotemporal pattern could be used to study the cell behavior in a non invasive approach. The microbial rhodopsin featured in the tandem proteins may be varied. Exchanging CatCh for NsXeR could allow the manipulation of the intracellular and endosomal pH which plays a role in the transition from early to late endosomes that could be studied [151].

10 Summary

Optogenetics is a technique that allows the manipulation of cellular activities by light. In order to achieve this, strategies for the genetic modification of cells by introducing the genes of light-sensitive proteins are combined with their fast optical control. In this way the activation or deactivation of processes in specific cells becomes possible.
The discovery of the light-activated cation channel channelrhodopsin 2 (ChR2) from the green alga *Chlamydomonas reinhardtii* [3, 4] revolutionized the developments on the field and a family of naturally occurring light-controlled proteins came into focus: the microbial rhodopsins (MRs). Their existence was known since the first light-driven proton pump bacteriorhodopsin (BR) from the haloarchaeon *Halobacterium salinarum* was found in the 1970s [8]. Microbial rhodopsins share a common 7-transmembrane helix structure with a retinal chromophore that binds to the 7^{th} helix via a Schiff base. Despite the similar architecture, MRs are functionally divers with family members that act as ion pumps, ion channels and light-sensors.
In optogenetic applications the properties of microbial rhodopsins are exploited. Expressing ChR2 and the inward chloride pump halorhodopsin (NpHR) [9] in neurons, for example, enabled the signal activation or silencing by blue or yellow light, respectively [10, 11]. Due to the different requirements in optogenetic applications, the search for new microbial rhodopsins and the study of their properties is essential in order to expand the optogenetic toolbox.
Apart from the application in electrically excitable cells, the optical control of intracellular signaling pathways enables the use in basically all tissues and cell types. The light-induced signaling of G-protein coupled receptors (GPCRs) could be achieved by the construction of vertebrate rhodopsin-GPCR chimeras (optoXRs) [13].
Optogenetics can be used as a tool in basic research on diseases like Parkinson's disease [20] or epilepsy [21] and for the mapping of neuronal networks, but it also could be used as a clinical tool in the treatment of human diseases such as retinitis pigmentosa disease [22]. Future challenges for optogenetic applications are the precise cell-specific expression of optogenetic tools as well as their targeting to intracellular compartments.

In the present work, the inward proton pump NsXeR [31, 32] and the outward sodium ion pump KR2 [33] were characterized. Both were discovered only recently and their

unique features make them potential optogenetic tools. Furthermore, an unconventional optogenetic application was studied that combines the chemokine receptor CXCR4, a rhodopsin-like GPCR, with a microbial rhodopsin in a single tandem protein. Upon CXCR4 activation by SDF1 binding, the tandem protein can be internalized into endosomes, which enables the intracellular excitation of the light-sensitive protein.

NsXeR from the nanohaloarchaeon *Nanosalina* belongs to a new class of microbial rhodopsins called xenorhodopsins that pump protons from the extracellular to the cytoplasmic side of a cell [31, 32]. Since the dependence of the pump on the electrochemical gradient is negligible compared to the passive transport of channelrhodopsins, NsXeR would be appealing as an optogenetic tool. The inward pumping of protons by NsXeR was confirmed and the structure was solved [32], but the mechanism that determines the pump vectoriality remained unclear. Therefore, a comprehensive electrophysiological study on NsXeR was performed in the present work.
In patch clamp measurements NsXeR was investigated under precise control of the membrane potential as well as the ionic composition of the intracellular and extracellular solutions. The protein was heterologously expressed in NG108-15 cells. In measurements with continuous 561 nm illumination, active pump currents were observed working against an electrochemical gradient. The steady-state photocurrents I_{ss} that were evoked by the continuous illumination showed a liner potential dependence. The influence of the intracellular pH was investigated and no dependence of the extrapolated potentials of zero current E_0 (118 mV at pH 7.4) and the exponential decay rate constant of the steady-state currents k_2 was observed. Comparison of the decay rate k_2 to the kinetics of the photocycle transitions allows the conclusion that the rate-limiting step is the MII decay. The MII decay was suggested to be accompanied by the reprotonation of the retinal Schiff base from the extracellular side [32] which is in agreement with the independence of the photocurrents on the intracellular pH.
For measurements using the black lipid membrane technique (BLM), NsXeR protein was purified and reconstituted in proteoliposomes. The proteoliposomes were attached to a BLM and illuminated with 20 ns light pulses at 556 nm. The synchronous excitation of a single photocycle turnover causes proton transport that can be monitored as a photovoltage signal. The photovoltage measured is directly proportional to the transported charge. With this method the electrogenic steps of the NsXeR photocycle can be determined with a high temporal resolution. The photovoltage signal was exponentially fitted and three active electrogenic steps could be identified. At pH 7.4 the three observed time constants were 220 μs, 1 ms and 15 ms that accounted for 42%, 10% and 48% of the overall transferred charge, respectively. The comparison with flash photolysis data allowed the assignment of the electrogenic steps to the transitions in the NsXeR photocycle. The

first step with the time constant t_1 was attributed to the MI rise that is accompanied by the Schiff base deprotonation and a proton release to the intracellular side [32]. t_2 was assigned to the MI→MII transition that was proposed to include a switch that changes the accessibility of the Schiff base from the intracellular to the extracellular side. The kinetics of the MII decay correlate with t_3. The MII decay was associated with the Schiff base reprotonation and a proton uptake from the extracellular side.
In pH titration measurements, no strong pH dependence was observed for the kinetics and transported charge of the second electrogenic step. As the MI→MII transition was not associated with a proton transfer step, the pH independence of t_2 can be explained by the conformational change that seems to rule the transition. The acceleration of t_1 at high pH value can be explained by an easier proton release to the intracellular side. The same pH dependence of t_3 is less intuitive. A direct proton exchange between the extracellular side and the Schiff base can be excluded. It is more likely that the Schiff base is reprotonated from a donor group. Asp76 was proposed to be that group. The pH-sensitive changes of the transported charges of the first and third electrogenic steps ($\Delta\Psi$I and $\Delta\Psi$III) were explained by a possible delay of the early proton release at low pH values.
In NsXeR mutational studies, the influence of the side chains in the proton transport pathway was investigated. The putative proton acceptor to the Schiff base Asp220 was replaced by Asn and Glu and studied in patch clamp as well as UV-Vis spectroscopy measurements. For the mutant D220N no pump currents could be detected and the maximal absorption wavelength did not differ from the wild type. In D220E on the other hand a reduction of the Schiff base pK_a was determined and the I_{ss} decay rate k_2 from continuous illumination experiments was reduced (D220E $k_2 = 27.1 \pm 1.8$ Hz, wild type $k_2 = 83.1 \pm 2.6$ Hz). The results show that Asp220 is crucial for the proton transport and that it does not act as a counterion to the protonated Schiff base. Further, D220E does seem to have an influence on the electronic environment of the Schiff base. The Glu228 residue of the putative proton release pair Glu228-His94 was mutated to Asp and Asn, but at pH 7.4 no effect in the pump activity could be detected.
In patch clamp experiments featuring a continuous 561 nm background illumination and additional laser flashes at 355 nm, the blue-light-effect in NsXeR was investigated. Due to the continuous illumination, a constant part of the NsXeR protein populates the M intermediates that can absorb blue light. In bacteriorhodopsin the blue light absorption by protein in the M state leads to the reprotonation of the Schiff base from the primary proton acceptor Asp85 which short-circuits the photocycle and causes transient quenching of the steady-state photocurrents [74–76]. In the case of NsXeR, a potential dependent vectoriality could be observed for the transient currents induced by the 355 nm laser flashes. That is a novel observations made for microbial rhodopsins. It seems that in the NsXeR blue-light-effect a reprotonation of the Schiff base can occur from both sides which

was explained by the different accessibilities of the two M intermediates MI and MII. In order to understand this unique blue-light-effect in NsXeR a model was proposed that is based on a potential dependent equilibrium between MI and MII.
The investigation in the present work gave new insights into the proton transport by NsXeR. In particular, the unusual blue-light-effect hints the special switch in NsXeR that is a decisive factor for the vectoriality of the proton transport.

The first microbial rhodopsin in which Na^+ pumping was observed is KR2 from the flavobacterium *Krokinobacter eikastus* [33]. KR2 could be a useful inhibitory optogenetic tool in situations where a change of the Cl^- or H^+ gradients is undesirable. In the absence of Na^+, KR2 also transports Li^+ or H^+ which raises the question how this variable active transport works. Despite several studies on KR2 the transport mechanism could not be fully explained.
The KR2 pump currents were investigated in patch clamp measurements with controlled ionic conditions and membrane potentials. KR2 was heterologously expressed in NG108-15 cells and the pump currents were studied at 532 nm continuous or under pulsed 530 nm illumination. In continuous illumination measurements the Na^+ concentration of the intra- and extracellular solutions was varied in a symmetrical manner to look at the Na^+ dependence of the steady-state currents I_{ss}. With increase of the Na^+ concentration I_{ss} showed a transition of the potential dependence from linear over a saturation-like behavior to an almost bell-shaped potential dependence. The exponential decay rate of the steady-state currents k_2 showed the same potential dependence correlating with I_{ss}. Therefore, it could be concluded that the currents are mainly kinetically limited. The behavior at high Na^+ concentrations and depolarizing potentials indicates the existence of a transport step with an inverse potential dependence. Due to the increase of the rate k_2 with rising Na^+ concentrations between -120 mV and -60 mV it could be concluded that the intracellular Na^+ uptake is the rate-limiting step for the pump at these conditions.
In similar measurements, the influence of the intracellular pH under Na^+ "free" conditions was investigated. The rate k_2 increased at low intracellular pH. The potential E_0 was extrapolated from the linear potential dependence of the photocurrents I_{ss} and showed a shift to to more hyperpolarizing potentials with low intracellular pH. The results indicate that a significant part of the steady-state currents was carried by proton transport.
In measurements with pulsed illumination the transient pump currents were measured that were caused by a single synchronized photocycle turnover. The decay of the currents was exponentially fitted and three electrogenic steps could be identified. A potential and Na^+ dependence could only be observed for the third step with the rate $1/\tau_3$ that increases with the Na^+ concentration and at more positive potentials. At Na^+ "free" conditions $1/\tau_3$ also increases with lower intracellular pH values. Trying to assign the electrogenic steps to the

KR2 photocycle transitions solely based on the kinetics leads to discrepancies. τ_3 is in the same range as the O decay, but the strongest sodium dependence was reported for the L/M→O transition [33]. Therefore, a photocycle model was applied that was developed in order to overcome the inconsistencies described above [141]. The model introduces a spectroscopically silent M1→M2 transition that the second electrogenic step was assigned to. Based on the Na^+ dependence of the rate $1/\tau_3$ two competitive rates k_{Na} and k_H as well as the k_4 were introduced. The rates k_{Na} and k_H describe the M2→O transitions in the cases of Na^+ or H^+ transport, respectively. The Na^+ and pH independent O→KR2 transition was attributed to k_4.
The relative transported charges Q_2 and Q_3 of the second and third electrogenic steps exhibited a potential and Na^+ dependence. In order to explain the results a model was proposed that introduces a compensatory charge transfer by a proton release and uptake during the photocycle.

The chemokine receptor CXCR4 is a rhodopsin-like GPCR that is involved in many biological processes [91–95] and is activated upon binding its agonist SDF1 [96]. The activation causes the internalization of CXCR4 into endosomes which was utilized by the tandem proteins investigated in this work. The expression of CXCR4 together with microbial rhodopsins in a single functional entity should allow the excitation of the light-driven proteins in endosomes.
In patch clamp measurements the conserved functionality of the mutant ChR2(L132C) (CatCh) that has an enhanced Ca^{2+} permeability was verified. Also the internalization of the tCXCR4/CatCh tandem upon CXCR4 activation by SDF1 could be observed by monitoring the time dependent reduction of the CatCh signal. Using tCXCR4/Arch, a tandem that carries the proton pump Arch [113], the SDF1 induced internalization could be investigated using confocal laser scanning microscopy. The fluorescence signals of a labeled CXCR4-specific antibody and the YFP that is expressed in the tandem were detected. In cells that were exposed to SDF1 the signals colocalized in intracellular vesicles. Treatment with the CXCR4 antagonist AMD3100 [98] impaired the internalization and the colocalization of the signals was observed mainly in the cell membrane. The results show the functionality of both tandem partners and the applicability of this kind of optochemokine tandems that could be used to manipulate the intracellular Ca^{2+} concentration or pH value.

11 Zusammenfassung

Die Optogenetik ist eine Technologie, welche die Manipulation von zellulären Aktivitäten durch Licht ermöglicht. Dazu werden Strategien zur genetischen Modifikation von Zellen durch Einbringen der genetischen Information von lichtsensitiven Proteinen mit deren schneller optischer Kontrolle kombiniert. Die Aktivierung oder Deaktivierung von Vorgängen in spezifischen Zellen wird dadurch realisierbar.
Die Entdeckung von Channelrhodopsin 2 (ChR2) aus der Grünalge *Chlamydomonas reinhardtii* [3, 4], einem lichtaktivierten Kationenkanal, revolutionierte die Entwicklungen auf dem Feld und lenkte den Fokus auf natürlich vorkommende lichtgesteuerte Proteine aus derselben Familie: den mikrobiellen Rhodopsinen (MR). Deren Existenz war bereits seit der Entdeckung der ersten lichtgetriebenen Protonenpumpe Bacteriorhodopsin (BR) aus dem Haloarchaeon *Halobacterium salinarum* [8] in den 1970er Jahren bekannt. Mikrobielle Rhodopsine verfügen über eine gemeinsame 7-Transmembranhelix Struktur mit einem Retinal Chromophor, welches über eine Schiff'sche Base an die siebte Transmembran Helix bindet. Trotz der ähnlichen Architektur, sind MR funktionell divers. Unter den Mitgliedern finden sich Ionenpumpen, Ionenkanäle und sensorische Proteine.
In optogenetischen Anwendungen werden die Eigenschaften von mikrobiellen Rhodopsinen ausgenutzt. Durch die Expression von ChR2 und der einwärts Cl^--Pumpe Halorhodopsin (NpHR) [9] in Neuronen ist es beispielsweise möglich, Signale durch blaues oder gelbes Licht zu aktivieren bzw. zu inhibieren [10, 11]. Aufgrund unterschiedlichster Anforderungen in optogenetischen Applikationen, ist die Suche nach neuen mikrobiellen Rhodopsinen und die Untersuchung ihrer Eigenschaften unerlässlich für die Erweiterung der Auswahl an optogenetischen Werkzeugen.
Neben den naheliegenden Anwendungen in elektrisch erregbaren Zellen, bringt die optische Kontrolle von intrazellulären Signalwegen auch Einsatzmöglichkeiten in anderen Gewebe- und Zelltypen. Dazu wurden beispielsweise Rhodopsin-GPCR Chimären (optoXR) konstruiert [13], welche die optische Anregung intrazellulärer Signalkaskaden durch G-Protein gekoppelte Rezeptoren (GPCR) ermöglichen.
Die Anwendungsmöglichkeiten der Optogenetik erstrecken sich von der Grundlagenforschung an Krankheiten wie Parkinson [20] oder Epilepsie [21] und der Kartierung neuronaler Netzwerke, bis zum Einsatz als klinisches Werkzeug beispielsweise in der Wiederherstellung des Sehvermögens bei der Behandlung von Retinitis pigmentosa [22]. Hürden

für weitere Anwendungen sind die präzise, zellspezifische Expression der optogenetischen Werkzeuge sowie das Targeting zu intrazellulären Zellkompartimenten.

In der vorliegenden Arbeit wurden die einwärts transportierende Protonenpumpe NsXeR [31, 32], sowie die auswärts Natriumionenpumpe KR2 [33] untersucht. Beide wurden in jüngerer Zeit entdeckt und verfügen über Eigenschaften, die sie zu potentiellen optogenetischen Werkzeugen machen. Des Weiteren wurde eine unkonventionelle optogenetische Anwendung betrachtet, bei der der Chemokinrezeptor CXCR4, ein Rhodopsin-ähnlicher GPCR, mit einem mikrobiellen Rhodopsin kombiniert wurde. Die Internalisierung des Tandems in Endosomen, die durch die Aktivierung von CXCR4 durch seinen Liganden SDF1 ausgelöst wird, ermöglicht die intrazelluläre Anregung des Licht-sensitiven Proteins.

NsXeR aus dem Nanohaloarchaeon *Nanosalina* gehört zu der neuen Klasse mikrobieller Rhodopsine, die Xenorhodopsine genannt werden und Protonen von der extrazellulären zur zytoplasmatischen Seite einer Zelle pumpen [31,32]. Da die Abhängigkeit der Pumpaktivität vom elektrochemischen Potential im Vergleich zu den passiven Strömen durch Channelrhodopsine vernachlässigbar ist, wäre NsXeR ein attraktives optogenetisches Werkzeug. Der einwärts gerichtete, aktive Transport von Protonen durch NsXeR wurde bestätigt und die NsXeR Struktur gelöst [32], aber der Mechanismus, der die Vektorialität bestimmt, blieb weiter unklar. Aufgrund dessen wurde in der vorliegenden Arbeit eine umfassende elektrophysiologische Untersuchung von NsXeR durchgeführt.
An NsXeR wurden Patch Clamp Messungen durchgeführt, die eine genaue Kontrolle des Membranpotentials sowie der ionischen Zusammensetzung der intra- und extrazellulären Lösungen erlauben. Dafür wurden NG108-15 Zellen mit einem Konstrukt transfiziert, welches eine P2A Peptidsequenz [108] beinhaltet, die für eine Teilung zwischen NsXeR und dem Fluoreszenzprotein Katushka [109] sorgt. In Messungen, bei denen die Zellen kontinuierlich mit 561 nm Licht beleuchtet wurden, konnten auch entgegen eines elektrochemischen Gradienten aktive Einwärtsströme gemessen werden. Die steady-state Ströme I_{ss}, die sich bei Dauerbelichtung einstellen, zeigten eine lineare Abhängigkeit vom Membranpotential. Der Einfluss des intrazellulären pHs wurde untersucht, wobei keine Abhängigkeit der extrapolierten Potentiale E_0 (118 mV bei pH 7.4, I_{ss} = 0 pA) und der exponentiellen Abfallrate der steady-state Ströme k_2 festgestellt werden konnten. Der Vergleich der Abfallrate k_2 mit den Übergängen im NsXeR Photozyklus, lässt den Schluss zu, dass der ratenlimitierende Schritt der MII Zerfall ist. Dieser soll mit der Reprotonierung der Schiff'schen Base von der extrazellulären Seite einhergehen [32], was zu der Unabhängigkeit der Ströme vom intrazellulären pH passt.
Für elektrische Messungen an der black lipid membrane (BLM) wurde NsXeR Protein aufgereinigt und in Proteoliposomen rekonstituiert. Diese wurden an der BLM angelagert

und mit einem 20 ns Lichtpuls bei 556 nm Wellenlänge belichtet. Durch die synchrone Anregung eines einzelnen Photozyklusdurchlaufs werden Protonen transportiert, was als Spannungssignal gemessen werden kann. Dieses ist direkt proportional zur transportierten Ladung. Die elektrogenen Schritte im NsXeR Photozyklus können mit dieser Methode mit einer hohen zeitlichen Auflösung bestimmt werden. Das Spannungssignal wurde exponentiell gefittet, wobei drei aktive elektrogene Schritte identifiziert werden konnten. Bei pH 7.4 betrugen die ermittelten Zeitkonstanten etwa 220 μs, 1 ms und 15 ms, denen 42%, 10% und 48% an der Gesamtladungsverschiebung zugeordnet wurden. Durch den Vergleich mit Blitzlichtphotolyse Daten konnten die elektrogenen Schritte den Übergängen im Photozyklus zugeordnet werden. Der erste Schritt mit der Zeitkonstante t_1 wurde dem MI Aufbau zugeschrieben, der begleitet wird von der Deprotonierung der Schiff'schen Base und einer Protonenabgabe zur intrazellulären Seite [32]. t_2 wurde dem MI→MII Übergang zugeordnet, für den eine Änderung der Zugänglichkeit der Schiff'schen Base, einem Switch, vom Intra- zum Extrazellulären vorgeschlagen wurde. Die Kinetik des MII Zerfalls korreliert mit t_3. Der MII Zerfall wurde mit der Reprotonierung der Schiff'schen Base sowie einer Protonenaufnahme von der extrazellulären Seite her in Verbindung gebracht.
In pH Titrationsmessungen wurde keine starke pH Abhängigkeit für die Kinetik und den Ladungstransportanteil des zweiten elektrogenen Schritts gefunden. Da dem MI→MII Übergang keine Protonentransferschritte zugeordnet wurden, lässt sich die pH Unabhängigkeit dadurch erklären, dass t_2 durch eine Konformationsänderung bestimmt wird. Die Beschleunigung von t_1 bei höheren pH Werten lässt sich mit einer erleichterten intrazellulären Protonenabgabe erklären. Dieselbe pH Abhängigkeit für t_3 ist weniger intuitiv. Ein direkter Protonenaustausch zwischen der extrazellulären Seite und der Schiff'schen Base können ausgeschlossen werden. Wahrscheinlicher ist die Reprotonierung durch eine Donor-Gruppe, für die Asp76 vorgeschlagen wurde. Die pH-sensitive Änderung der relativen Ladungstransferanteile des ersten und dritten elektrogenen Schrittes ($\Delta\Psi$I und $\Delta\Psi$III) wurden durch eine mögliche Verzögerung der frühen Protonenabgabe bei niedrigen pH Werten erklärt.
In Messungen an NsXeR Mutanten wurde der Einfluss von Seitenketten im angenommenen Protonentransportweg betrachtet. Der mutmaßliche Protonenakzeptor Asp220 wurde gegen Asn und Glu ausgetauscht und in Patch Clamp sowie UV-Vis Spektroskopie Messungen untersucht. Für D220N konnten keine Pumpströme festgestellt werden und die maximale Absorptionswellenlänge λ_{max} unterschied sich nicht vom Wildtyp. D220E dagegen führte zu einer Erniedrigung des pK_a-Werts der Schiff'schen Base und zu einer Verminderung der I_{ss}-Abfallsrate k_2 in Patch Clamp Dauerbelichtungsmessungen (D220E $k_2 = 27.1 \pm 1.8$ Hz, Wildtyp $k_2 = 83.1 \pm 2.6$ Hz). Es konnte gezeigt werden, dass Asp220 wesentlich für den Protonentransport ist und nicht als Gegenion für die protonierte Schiff'sche Base dient. D220E scheint einen Einfluss auf die elektronische Umgebung

der Schiff'schen Base zu haben. Auch Glu228 des mutmaßlichen Protonenabgabepaars Glu228-His94 wurde durch Asp und Asn ausgetauscht, aber es konnte bei pH 7.4 kein Einfluss auf die Pumpaktivität festgestellt werden.
In Patch Clamp Experimenten bei 561 nm Dauerbelichtung und zusätzlicher gepulster Belichtung bei 355 nm wurde der Blaulichteffekt an NsXeR untersucht. Durch die hintergründige Dauerbelichtung befinden sich ständig NsXeR Proteine in einem der M Intermediate, welche blaues Licht absorbieren können. In Bacteriorhodopsin führt die Blaulichtabsorption des M Zustands zu einer Reprotonierung der Schiff'schen Base vom primären Protonenakzeptor Asp85, was den Photozyklus kurz schließt und in Strommessungen als transientes Quenching sichtbar wird [74–76]. Für NsXeR konnte eine Potentialabhängigkeit für die Richtung der transienten Ströme, die durch die 355 nm Belichtung hervorgerufen wurden, festgestellt werden. Dies ist eine neuartige Beobachtung für mikrobielle Rhodopsine. In NsXeR scheint beim Blaulichteffekt eine Reprotonierung der Schiff'schen Base von beiden Seiten möglich zu sein, was auf die unterschiedlichen Zugänglichkeiten in den beiden M Zuständen MI und MII zurückgeführt wurde. Für den Blaulichteffekt in NsXeR wurde ein Modell vorgeschlagen, welches auf einem potentialabhängigen Gleichgewicht zwischen MI und MII basiert.
Die Untersuchungen in der vorliegenden Arbeit ergaben neue Einsichten in den Protonentransport durch NsXeR. Insbesondere der ungewöhnliche Blaulichteffekt gibt Hinweise auf einen besonderen Switch in NsXeR, welcher die Vektorialität des Protonentransports maßgeblich beeinflusst.

Das erste mikrobielle Rhodopsin, bei dem das Pumpen von Na^+ beobachtet wurde, ist KR2 aus dem Flavobakterium *Krokinobacter eikastus* [33]. In Situationen, in denen die Änderung von Cl^-- oder H^+-Gradienten unerwünscht ist, würde sich KR2 als inhibitorisches optogenetisches Werkzeug eignen. In der Abwesenheit von Na^+ pumpt KR2 auch Li^+ und H^+ auswärts, was die Frage nach dem Mechanismus dieses variablen, aktiven Transports aufwirft. Trotz inzwischen zahlreicher Studien konnte der Transportmechanismus durch KR2 nicht vollständig geklärt werden.
Die KR2 Pumpströme wurden in Patch Clamp Messungen bei kontrollierten ionischen Bedingungen und Membranpotentialen untersucht. Dazu wurde KR2 heterolog in NG108-15 Zellen exprimiert und die Pumpströme wurden bei 532 nm Dauerbelichtung oder bei gepulster 530 nm Belichtung gemessen. Bei kontinuierlicher Belichtung wurde die Na^+-Konzentration der intra- und extrazellulären Lösungen symmetrisch variiert, um den Einfluss von Na^+ auf die steady-state Ströme zu betrachten. In Abhängigkeit der Na^+-Konzentration konnte eine Veränderung der Form der Potentialabhängigkeit der steady-state Ströme I_{ss} beobachtet werden. Mit steigender Na^+-Konzentration zeigte diese den Übergang von einer linearen Abhängigkeit, zu einem sättigungsähnlichen Verhalten bis hin

zu einer fast glockenförmigen Form. Die exponentielle Abfallrate der steady-state Ströme k_2 korrelierte in ihrer Potentialabhängigkeit mit den I_{ss}. Daraus konnte geschlossen werden, dass die Ströme überwiegend kinetisch limitiert sind. Das Verhalten bei hohen Na^+-Konzentrationen und depolarisierenden Potentialen weist dabei auf einen Transportschritt mit einer entgegengesetzten Potentialabhängigkeit hin. Aus der Erhöhung der Rate k_2 mit steigender Na^+-Konzentration zwischen -120 mV und -60 mV kann geschlossen werden, dass die Na^+-Aufnahme von der intrazellulären Seite bei diesen Bedingungen die Limitierung für die Pumpe darstellt.
In ähnlichen Messungen wurde unter Na^+-"freien" Bedingungen, der Einfluss des intrazellulären pHs untersucht. Für die Rate k_2 wurde eine Erhöhung bei niedrigen pH Werten festgestellt. Aus der linearen Potentialabhängigkeit der Ströme I_{ss} wurde das Potential bei dem keine Ströme fließen E_0 extrapoliert, welches bei niedrigerem intrazellulären pH zu hyperpolarisierenden Potentialen verschoben wurde. Aus diesen Ergebnissen lässt sich schließen, dass die steady-state Ströme zu einem nicht vernachlässigbaren Teil durch den Transport von Protonen hervorgerufen wurden.
In Messungen mit gepulster Belichtung wurden die transienten Pumpströme gemessen, die durch einen einzelnen, synchronisierten Photozyklusdurchlauf hervorgerufen wurden. Durch exponentielles Fitten des Stromabfalls konnten drei elektrogene Schritte identifiziert werden. Eine Abhängigkeit vom Potential und der Na^+-Konzentration konnte nur für den dritten Schritt mit der Rate $1/\tau_3$ festgestellt werden, wobei $1/\tau_3$ mit der Na^+-Konzentration und bei positiveren Potentialen steigt. Unter Na^+-"freien" Bedingungen steigt $1/\tau_3$ auch mit niedrigeren intrazellulären pH Werten. Die Zuordnung der elektrogenen Schritte zum KR2 Photozyklus auf Basis der Kinetiken führt zu Unstimmigkeiten. τ_3 ist zwar in der Größenordnung des O Zerfalls, aber die größte Na^+-Abhängigkeit wurde für den Übergang L/M→O berichtet [33]. Aufgrund dessen wurde ein Photozyklus Modell angewendet, das wegen dieser Diskrepanzen entwickelt wurde [141]. Das Modell führt einen M1→M2 Übergang ein, dem der zweite elektrogene Schritt zugeordnet wurde. Auf Basis der Na^+-Abhängigkeit von $1/\tau_3$ wurden zwei kompetitive Ratenkonstanten k_{Na} und k_H, sowie die Rate k_4 eingeführt. k_{Na} und k_H beschreiben dabei den M2→O Übergang bei Na^+- oder H^+-Transport. Der Na^+- und pH-unabhängige O→KR2 Übergang erfolgt mit k_4.
Die relativen Ladungstransportanteile Q_2 und Q_3 des zweiten und dritten elektrogenen Schrittes sind sowohl potential- als auch Na^+-abhängig. Um dieses Verhalten zu erklären, wurde ein Modell vorgeschlagen, bei dem ein Ausgleichsladungstransfer in Form von einer Protonenabgabe und -wiederaufnahme während des Photozyklus eingeführt wurde.

Der Chemokinrezeptor CXCR4 ist ein Rhodopsin-ähnlicher GPCR, welcher in vielen biologischen Prozessen involviert ist [91–95] und durch die Bindung seines Agonisten SDF1 [96]

aktiviert wird. Dies führt zu der Internalisierung von CXCR4 in Endosomen, was in den hier untersuchten Tandem Proteinen ausgenutzt wurde. Die Expression von CXCR4 zusammen mit mikrobiellen Rhodopsinen in einer funktionellen Einheit sollte die Anregung der lichtgetriebenen Proteine in Endosomen erlauben.
Die erhaltene Funktionalität der ChR2 Mutante ChR2(L132C) (CatCh) mit erhöhter Ca^{2+}-Permeabilität [112] im Tandem Protein tCXCR4/CatCh wurde in Patch Clamp Messungen nachgewiesen. Auch die Internalisierung von tCXCR4/CatCh konnte anhand der zeitabhängigen Abnahme des CatCh-Signals nach der CXCR4-Aktivierung durch SDF1 in Strommessungen beobachtet werden. Für tCXCR4/Arch, ein Tandem Protein mit einer Protonenpumpe [113], wurde die SDF1-induzierte Internalisierung mit Hilfe der konfokalen Laser-Scanning-Mikroskopie betrachtet. Bei Zellen, die mit SDF1 behandelt wurden, konnte eine Kolokalisierung der Fluoreszenz des im Tandem exprimierten YFP und der eines gelabelten CXCR4-spezifischen Antikörpers in intrazellulären Vesikeln beobachtet werden. Bei Behandlung mit dem CXCR4 Antagonisten AMD3100 [98] wurde die Kolokalisierung hauptsächlich in der Zellmembran festgestellt, da die Internalisierung blockiert war. Die Ergebnisse zeigen die Funktionalität beider Tandempartner und die Anwendbarkeit dieser Art von Tandemproteinen, die zum Beispiel für die Manipulation der intrazellulären Ca^{2+}-Konzentration oder des pH-Wertes eingesetzt werden könnten.

References

[1] Adams, S. R. & Tsien, R. Y. Controlling Cell Chemistry with Caged Compounds. *Annu. Rev. Physiol.* **55**, 755–784 (1993).

[2] Zemelman, B. V., Lee, G. A., Ng, M. & Miesenböck, G. Selective Photostimulation of Genetically ChARGed Neurons. *Neuron* **33**, 15–22 (2002).

[3] Nagel, G. *et al.* Channelrhodopsin-1: A Light-Gated Proton Channel in Green Algae. *Science* **296**, 2395–2398 (2002).

[4] Nagel, G. *et al.* Channelrhodopsin-2, a directly light-gated cation-selective membrane channel. *PNAS* **100**, 13940–13945 (2003).

[5] Boyden, E. S., Zhang, F., Bamberg, E., Nagel, G. & Deisseroth, K. Millisecond-timescale, genetically targeted optical control of neural activity. *Nat. Neurosci.* **8**, 1263–8 (2005).

[6] Li, X. *et al.* Fast noninvasive activation and inhibition of neural and network activity by vertebrate rhodopsin and green algae channelrhodopsin. *PNAS* **102**, 17816–17821 (2005).

[7] Nagel, G. *et al.* Light Activation of Channelrhodopsin-2 in Excitable Cells of *Caenorhabditis elegans* Triggers Rapid Behavioral Responses. *Curr. Biol.* **15**, 2279–2284 (2005).

[8] Oesterhelt, D. & Stoeckenius, W. Rhodopsin-like Protein from the Purple Membrane of *Halobacterium halobium*. *Nat. New Biol.* **233**, 149–152 (1971).

[9] Schobert, B. & Lanyi, J. K. Halorhodopsin Is a Light-driven Chloride Pump. *J. Biol. Chem.* **257**, 306–313 (1982).

[10] Zhang, F. *et al.* Multimodal fast optical interrogation of neural circuitry. *Nature* **446**, 633–639 (2007).

[11] Han, X. & Boyden, E. S. Multiple-Color Optical Activation, Silencing, and Desynchronization of Neural Activity, with Single-Spike Temporal Resolution. *PLOS ONE* **2**, e299 (2007).

[12] Deisseroth, K. Optogenetics. *Nat. Methods* **8**, 26–29 (2011).

[13] Airan, R. D., Thompson, K. R., Fenno, L. E., Bernstein, H. & Deisseroth, K. Temporally precise *in vivo* control of intracellular signalling. *Nature* **458**, 1025–1029 (2009).

[14] Levskaya, A., Weiner, O. D., Lim, W. A. & Voigt, C. A. Spatiotemporal control of cell signalling using a light-switchable protein interaction. *Nature* **461**, 997–1001 (2009).

[15] Wu, Y. I. *et al.* A genetically encoded photoactivatable Rac controls the motility of living cells. *Nature* **461**, 104–108 (2009).

[16] Brini, M., Calì, T., Ottolini, D. & Carafoli, E. *Intracellular calcium homeostasis and signaling*, vol. 12 (Springer, Dordrecht, 2013).

[17] Li, D., Hérault, K., Isacoff, E. Y., Oheim, M. & Ropert, N. Optogenetic activation of LiGluR-expressing astrocytes evokes anion channel-mediated glutamate release. *J. Physiol.* **590**, 855–873 (2012).

[18] Kyung, T. *et al.* Optogenetic control of endogenous Ca^{2+} channels *in vivo*. *Nat. Biotechnol.* **33**, 1092–1096 (2015).

[19] Ishii, T. *et al.* Light generation of intracellular Ca^{2+} signals by a genetically encoded protein BACCS. *Nat. Commun.* **6**, 8021 (2015).

[20] Gradinaru, V., Mogri, M., Thompson, K. R., Henderson, J. H. & Deisseroth, K. Optical Deconstruction of Parkinsonian Neural Circuitry. *Science* **324** (2009).

[21] Cela, E. & Sjöström, P. J. Novel Optogenetic Approaches in Epilepsy Research. *Front. Neurosci.* **13** (2019).

[22] Busskamp, V. & Roska, B. Optogenetic approaches to restoring visual function in retinitis pigmentosa. *Curr. Opin. Neurobiol.* **21**, 942–6 (2011).

[23] Moser, T. Optogenetic stimulation of the auditory pathway for research and future prosthetics. *Curr. Opin. Neurobiol.* **34**, 29–36 (2015).

[24] Spudich, J. L., Yang, C.-S., Jung, K.-H. & Spudich, E. N. Retinylidene Proteins: Structures and Functions from Archaea to Humans. *Annu. Rev. Cell D. Biol.* **16**, 365–392 (2000).

[25] Palczewski, K. G Protein–Coupled Receptor Rhodopsin. *Annu. Rev. Biochem.* **75**, 743–767 (2006).

[26] Shichida, Y. & Matsuyama, T. Evolution of opsins and phototransduction. *Phil. Trans. R. Soc. B* **364**, 2881–2895 (2009).

[27] Schmidt, T. M., Chen, S.-K. & Hattar, S. Intrinsically photosensitive retinal ganglion cells: many subtypes, diverse functions. *Trends Neurosci.* **34**, 572–580 (2011).

[28] Pierce, K. L., Premont, R. T. & Lefkowitz, R. J. Seven-transmembrane receptors. *Nat. Rev. Mol. Cell Biol.* **3**, 639–650 (2002).

[29] Saranak, J. & Foster, K. F. Rhodopsin guides fungal phototaxis. *Nature* **387**, 465–466 (1997).

[30] Avelar, G. M. *et al.* A Rhodopsin-Guanylyl Cyclase Gene Fusion Functions in Visual Perception in a Fungus. *Curr. Biol.* **24**, 1234–40 (2014).

[31] Ugalde, J. A., Podell, S., Narasingarao, P. & Allen, E. E. Xenorhodopsins, an enigmatic new class of microbial rhodopsins horizontally transferred between archaea and bacteria. *Biol. Direct* **6**, 52 (2011).

[32] Shevchenko, V. *et al.* Inward H^+ pump xenorhodopsin: Mechanism and alternative optogenetic approach. *Sci. Adv.* **3**, e1603187 (2017).

[33] Inoue, K. *et al.* A light-driven sodium ion pump in marine bacteria. *Nat. Commun.* **4**, 1678 (2013).

[34] Ernst, O. P. *et al.* Microbial and Animal Rhodopsins: Structures, Functions, and Molecular Mechanisms. *Chem. Rev.* **114**, 126–163 (2014).

[35] Govorunova, E. G., Sineshchekov, O. A., Li, H. & Spudich, J. L. Microbial Rhodopsins: Diversity, Mechanisms, and Optogenetic Applications. *Annu. Rev. Biochem.* **86**, 845–872 (2017).

[36] Jung, K.-H., Trivedi, V. D. & Spudich, J. L. Demonstration of a sensory rhodopsin in eubacteria. *Mol. Microbiol.* **47**, 1513–1522 (2003).

[37] Inoue, S. *et al.* Spectroscopic characteristics of *Rubricoccus marinus* xenorhodopsin (*Rm*XeR) and a putative model for its inward H^+ transport mechanism. *Phys. Chem. Chem. Phys.* **20**, 3172–3183 (2017).

[38] Inoue, K. *et al.* A natural light-driven inward proton pump. *Nat. Commun.* **7**, 13415 (2016).

[39] Béjà, O. *et al.* Bacterial Rhodopsin: Evidence for a New Type of Phototrophy in the Sea. *Science* **289**, 1902–1906 (2000).

[40] Mitchell, P. Chemiosmotic coupling in oxidative and photosynthetic phosphorylation. *Biol. Rev.* **41**, 445–501 (1966).

[41] Luecke, H., Schobert, B., Richter, H. T., Cartailler, J.-P. & Lanyi, J. K. Structure of Bacteriorhodopsin at 1.55 Å Resolution. *J. Mol. Biol.* **291**, 899–911 (1999).

[42] Gushchin, I. *et al.* Structural insights into the proton pumping by unusual proteorhodopsin from nonmarine bacteria. *PNAS* **110**, 12631–12636 (2013).

[43] Balashov, S. P. *et al.* Aspartate–Histidine Interaction in the Retinal Schiff Base Counterion of the Light-Driven Proton Pump of *Exiguobacterium sibiricum*. *Biochemistry* **51**, 5748–5762 (2012).

[44] Lanyi, J. K. Proton transfers in the bacteriorhodopsin photocycle. *Biochim. Biophys. Acta* **1757**, 1012–1018 (2006).

[45] Lanyi, J. K. Bacteriorhodopsin. *Annu. Rev. Physiol.* **66**, 665–688 (2004).

[46] Luecke, H. Atomic resolution structures of bacteriorhodopsin photocycle intermediates: the role of discrete water molecules in the function of this light-driven ion pump. *Biochim. Biophys. Acta* **1460**, 133–156 (2000).

[47] Wickstrand, C., Dods, R., Royant, A. & Neutze, R. Bacteriorhodopsin: Would the real structural intermediates please stand up? *Biochim. Biophys. Acta* **1850**, 536–553 (2015).

[48] Inoue, K. *et al.* Spectroscopic Study of Proton Transfer Mechanism of Inward Proton Pump Rhodopsin, *Parvularcula oceani* Xenorhodopsin. *J. Phys. Chem. B* **122**, 6453–6461 (2018).

[49] Bamann, C., Kirsch, T., Nagel, G. & Bamberg, E. Spectral Characteristics of the Photocycle of Channelrhodopsin-2 and Its Implication for Channel Function. *J. Mol. Biol.* **375**, 686–694 (2008).

[50] Ito, S., Sugita, S., Inoue, K. & Kandori, H. FTIR Analysis of a Light-driven Inward Proton-pumping Rhodopsin at 77 K. *Photochem. Photobiol.* **93**, 1381–1387 (2017).

[51] Balashov, S. P. Protonation reactions and their coupling in bacteriorhodopsin. *Biochim. Biophys. Acta* **1460**, 75–94 (2000).

[52] Balashov, S. P. *et al.* Light-Driven Na^+ Pump from *Gillisia limnaea*: A High-Affinity Na^+ Binding Site Is Formed Transiently in the Photocycle. *Biochemistry* **53**, 7549–7561 (2014).

[53] Yoshizawa, S. *et al.* Functional characterization of flavobacteria rhodopsins reveals a unique class of light-driven chloride pump in bacteria. *PNAS* **111**, 6732–6737 (2014).

[54] Inoue, K., Kato, Y. & Kandori, H. Light-driven ion-translocating rhodopsins in marine bacteria. *Trends Microbiol.* **23**, 91–98 (2015).

[55] Li, H., Sineshchekov, O., daÂ Silva, G. Z. & Spudich, J. InÂ Vitro Demonstration of Dual Light-Driven Na^+/H^+ Pumping by a Microbial Rhodopsin. *Biophys. J.* **109**, 1446–1453 (2015).

[56] Bertsova, Y. V., Bogachev, A. V. & Skulachev, V. P. Proteorhodopsin from *Dokdo-*

nia sp. PRO95 Is a Light-Driven Na^+-Pump. *Biochemistry (Moscow)* **80**, 449–454 (2015).

[57] Tsunoda, S. P. *et al.* Functional characterization of sodium-pumping rhodopsins with different pumping properties. *PLOS ONE* **12**, e0179232 (2017).

[58] Khan, S. T., Nakagawa, Y. & Harayama, S. *Krokinobacter* gen. nov., with three novel species, in the family *Flavobacteriaceae*. *Int. J. Syst. Evol. Microbiol.* **56**, 323–328 (2006).

[59] Kato, H. E. *et al.* Structural basis for Na^+ transport mechanism by a light-driven Na^+ pump. *Nature* **521**, 48–53 (2015).

[60] Grimm, C., Silapetere, A., Vogt, A., Bernal Sierra, Y. A. & Hegemann, P. Electrical properties, substrate specificity and optogenetic potential of the engineered light-driven sodium pump eKR2. *Sci. Rep.* **8**, 9316 (2018).

[61] Gushchin, I. *et al.* Crystal structure of a light-driven sodium pump. *Nat. Struct. Mol. Biol.* **22**, 390–395 (2015).

[62] Shibata, M. *et al.* Oligomeric states of microbial rhodopsins determined by high-speed atomic force microscopy and circular dichroic spectroscopy. *Sci. Rep.* **8**, 8262 (2018).

[63] Kovalev, K. *et al.* Structure and mechanisms of sodium-pumping KR2 rhodopsin. *Sci. Adv.* **5**, eaav2671 (2019).

[64] Konno, M. *et al.* Mutant of a Light-Driven Sodium Ion Pump Can Transport Cesium Ions. *J. Phys. Chem. Lett.* **7**, 51–55 (2016).

[65] Gushchin, I. *et al.* Structure of the light-driven sodium pump KR2 and its implications for optogenetics. *FEBS J.* **283**, 1232–1238 (2016).

[66] Kaur, J. *et al.* Solid-state NMR analysis of the sodium pump *Krokinobacter* rhodopsin 2 and its H30A mutant. *J. Struct. Biol.* **206**, 55–65 (2018).

[67] Shigeta, A. *et al.* Long-distance perturbation on Schiff base-counterion interactions by His30 and the extracellular Na^+-binding site in *Krokinobacter* rhodopsin 2. *Phys. Chem. Chem. Phys.* **20**, 8450–8455 (2018).

[68] Shigeta, A. *et al.* Solid-State Nuclear Magnetic Resonance Structural Study of the Retinal-Binding Pocket in Sodium Ion Pump Rhodopsin. *Biochemistry* **56**, 543–550 (2017).

[69] Hontani, Y. *et al.* The photochemistry of sodium ion pump rhodopsin observed by watermarked femto- to submillisecond stimulated Raman spectroscopy. *Phys. Chem. Chem. Phys.* **18**, 24729–24736 (2016).

[70] Suomivuori, C. M., Gamiz-Hernandez, A. P., Sundholm, D. & Kaila, V. R. I. Energetics and dynamics of a light-driven sodium-pumping rhodopsin. *PNAS* **114**, 7043–7048 (2017).

[71] Kandori, H., Inoue, K. & Tsunoda, S. P. Light-Driven Sodium-Pumping Rhodopsin: A New Concept of Active Transport. *Chem. Rev.* **119**, 10646–10658 (2018).

[72] Kato, Y., Inoue, K. & Kandori, H. Kinetic Analysis of H^+–Na^+ Selectivity in a Light-Driven Na^+-Pumping Rhodopsin. *J. Phys. Chem. Lett.* **6**, 5111–5115 (2015).

[73] Ormos, P., Dancsházy, Z. & Karvaly, B. Mechanism of generation and regulation of photopotential by bacteriorhodopsin in bimolecular lipid membrane. *Biochim. Biophys. Acta* **503**, 304–315 (1978).

[74] Nagel, G., Kelety, B., Möckel, B., Büldt, G. & Bamberg, E. Voltage Dependence of Proton Pumping by Bacteriorhodopsin Is Regulated by the Voltage-Sensitive Ratio of M_1 to M_2. *Biophys. J.* **74**, 403–412 (1998).

[75] Geibel, S. *et al.* The Voltage-Dependent Proton Pumping in Bacteriorhodopsin Is Characterized by Optoelectric Behavior. *Biophys. J.* **81**, 2059–2068 (2001).

[76] Geibel, S., Lörinczi, E., Bamberg, E. & Friedrich, T. Voltage Dependence of Proton Pumping by Bacteriorhodopsin Mutants with Altered Lifetime of the M Intermediate. *PLOS ONE* **8**, e73338 (2013).

[77] Eckert, C. E., Kaur, J., Glaubitz, C. & Wachtveitl, J. Ultrafast Photoinduced Deactivation Dynamics of Proteorhodopsin. *J. Phys. Chem. Lett.* **8**, 512–517 (2017).

[78] Dorsam, R. T. & Gutkind, J. S. G-protein-coupled receptors and cancer. *Nat. Rev. Cancer* **7**, 79–94 (2007).

[79] Rosenbaum, D. M., Rasmussen, S. G. F. & Kobilka, B. K. The structure and function of G-protein-coupled receptors. *Nature* **459**, 356–363 (2009).

[80] Ballesteros, J. A. *et al.* Activation of the β_2-Adrenergic Receptor Involves Disruption of an Ionic Lock between the Cytoplasmic Ends of Transmembrane Segments 3 and 6. *J. Biol. Chem.* **276**, 29171–29177 (2001).

[81] Farahbakhsh, Z. T., Ridge, K. D., Khorana, H. G. & Hubbell, W. L. Mapping Light-Dependent Structural Changes in the Cytoplasmic Loop Connecting Helixes C and D in Rhodopsin: A Site-Directed Spin Labeling Study. *Biochemistry* **34**, 8812–8819 (1995).

[82] Gilman, A. G. G Proteins: Transducers of Receptor-Generated Signals. *Annu. Rev. Biochem.* **56**, 615–649 (1987).

[83] Neves, S. R., Ram, P. T. & Iyengar, R. G Protein Pathways. *Science* **296**, 1636–1639

(2002).

[84] Pitcher, J. A., Freedman, N. J. & Lefkowitz, R. J. G Protein-Coupled Receptor Kinases. *Annu. Rev. Biochem.* **67**, 653–692 (1998).

[85] Krupnick, J. G. & Benovic, J. L. The Role of Receptor Kinases and Arrestins in G Protein-Coupled Receptor Regulation. *Annu. Rev. Pharmacol. Toxicol.* **38**, 289–319 (1998).

[86] Lohse, M. J., Benovic, J. L., Codina, J., Caron, M. G. & Lefkowitz, R. J. β-Arrestin: A Protein That Regulates β-Adrenergic Receptor Function. *Science* **248**, 1547–1550 (1990).

[87] Scott, M. G. H., Benmerah, A., Muntaner, O. & Marullo, S. Recruitment of Activated G Protein-coupled Receptors to Pre-existing Clathrin-coated Pits in Living Cells. *J. Biol. Chem.* **277**, 3552–3559 (2002).

[88] Santini, F., Gaidarov, I. & Keen, J. H. G protein–coupled receptor/arrestin3 modulation of the endocytic machinery. *J. Cell Biol.* **156**, 665–676 (2002).

[89] Andersen, C. B. F. & Moestrup, S. K. How calcium makes endocytic receptors attractive. *Trends Biochem. Sci.* **39**, 82–90 (2014).

[90] Marchese, A. Endocytic trafficking of chemokine receptors. *Curr. Opin. Cell Biol.* **27**, 72–77 (2014).

[91] Nagasawa, T. *et al.* Defects of B-cell lymphopoiesis and bone-marrow myelopoiesis in mice lacking the CXC chemokine PBSF/SDF-1. *Nature* **382**, 635–638 (1996).

[92] Zou, Y.-R., Kottmann, A. H., Kuroda, M., Taniuchi, I. & Littman, D. R. Function of the chemokine receptor CXCR4 in haematopoiesis and in cerebellar development. *Nature* **393**, 595–599 (1998).

[93] Ma, Q. *et al.* Impaired B-lymphopoiesis, myelopoiesis, and derailed cerebellar neuron migration in CXCR4- and SDF-1-deficient mice. *PNAS* **95**, 9448–9453 (1998).

[94] McGrath, K. E., Koniski, A., Maltby, K. M., McGann, J. K. & Palis, J. Embryonic Expression and Function of the Chemokine SDF-1 and Its Receptor, CXCR4. *Dev. Biol.* **213**, 442–456 (1999).

[95] Nagasawa, T., Tachibana, K. & Kishimoto, T. A novel CXC chemokine PBSF/SDF-1 and its receptor CXCR4: their functions in development, hematopoiesis and HIV infection. *Semin. Immunol.* **10**, 179–185 (1998).

[96] Nagasawa, T., Kikutani, H. & Kishimoto, T. Molecular cloning and structure of a pre-B-cell growth-stimulating factor. *PNAS* **91**, 2305–2309 (1994).

[97] Janowski, M. Functional diversity of SDF-1 splicing variants. *Cell Adh. Migr.* **3**,

243–249 (2009).

[98] Hatse, S., Princen, K., Bridger, G., De Clercq, E. & Schols, D. Chemokine receptor inhibition by AMD3100 is strictly confned to CXCR4. *FEBS Lett.* **527**, 255–262 (2002).

[99] Busillo, J. M. & Benovic, J. L. Regulation of CXCR4 signaling. *Biochim. Biophys. Acta* **1768**, 952–963 (2007).

[100] Diaz, G. A. & Gulino, A. V. WHIM Syndrome: A Defect in CXCR4 Signaling. *Curr. Allergy Asthma Rep.* **5**, 350–355 (2005).

[101] Cronin, P. A., Wang, J. H. & Redmond, H. P. Hypoxia increases the metastatic ability of breast cancer cells via upregulation of CXCR4. *BMC Cancer* **10** (2010).

[102] Hiller, D. J., Li, B. D. L. & Chu, Q. D. CXCR4 as a Predictive Marker for Locally Advanced Breast Cancer Post-Neoadjuvant Therapy. *J. Surg. Res.* **166**, 14–18 (2011).

[103] Popple, A. *et al.* The chemokine, CXCL12, is an independent predictor of poor survival in ovarian cancer. *Br. J. Cancer* **106**, 1306–1313 (2012).

[104] Zhao, C., Lu, X., Bu, X., Zhang, N. & Wang, W. Involvement of tumor necrosis factor-α in the upregulation of CXCR4 expression in gastric cancer induced by Helicobacter pylori. *BMC Cancer* **10**, 419 (2010).

[105] Furusato, B., Mohamed, A., Uhlén, M. & Rhim, J. S. CXCR4 and cancer. *Pathol. Int.* **60**, 497–505 (2010).

[106] Arnolds, K. L. & Spencer, J. V. CXCR4: A virus's best friend? *Infect. Genet. Evolut.* **25**, 146–156 (2014).

[107] Gradinaru, V. *et al.* Molecular and Cellular Approaches for Diversifying and Extending Optogenetics. *Cell* **141**, 154–165 (2010).

[108] Kuzmich, A. I., Vvedenskii, A. V., Kopantzev, E. P. & Vinogradova, T. V. Quantitative Comparison of Gene Co-Expression in a Bicistronic Vector Harboring IRES or Coding Sequence of Porcine Teschovirus 2A Peptide. *Russ. J. Bioorganic Chem.* **39**, 406–416 (2013).

[109] Shcherbo, D. *et al.* Bright far-red fluorescent protein for whole-body imaging. *Nat. Methods* **4**, 741–746 (2007).

[110] Kleinlogel, S. *et al.* A gene-fusion strategy for stoichiometric and co-localized expression of light-gated membrane proteins. *Nat. Methods* **8**, 1083–1088 (2011).

[111] Feldbauer, K. *et al.* Optochemokine Tandem for Light-Control of Intracellular Ca^{2+}. *PLOS ONE* **11**, e0165344 (2016).

[112] Kleinlogel, S. *et al.* Ultra light-sensitive and fast neuronal activation with the Ca^{2+}-permeable channelrhodopsin CatCh. *Nat. Neurosci.* **14**, 513–518 (2011).

[113] Chow, B. Y. *et al.* High-performance genetically targetable optical neural silencing by light-driven proton pumps. *Nature* **463**, 98–102 (2010).

[114] Numberger, M. & Draghuhn, A. *Patch-Clamp-Technik* (Spektrum Akademischer Verlag, Heidelberg, Germany, 1996).

[115] Neher, E. & Sakmann, B. Single-channel currents recorded from membrane of denervated frog muscle fibres. *Nature* **260**, 799–802 (1976).

[116] Hamill, O. P., Marty, A., Neher, E., Sakmann, B. & Sigworth, F. J. Improved Patch-Clamp Techniques for High-Resolution Current Recording from Cells and Cell-Free Membrane Patches. *Pflügers Arch* **391**, 85–100 (1981).

[117] Mueller, P., Rudin, D. O., Tien, H. T. & Wescott, W. C. Reconstitution of Cell Membrane Structure *in vitro* and its Transformation into an Excitable System. *Nature* **194**, 979–980 (1962).

[118] Holz, M., Lindau, M. & Heyn, M. P. Distributed Kinetics of the Charge Movements in Bacteriorhodopsin: Evidence for Conformational Substates. *Biophys. J.* **53**, 623–633 (1988).

[119] Druckmann, S., Ottolenghi, M., Pande, A., Pande, J. & Callender, R. H. Acid-Base Equilibrium of the Schiff Base in Bacteriorhodopsin. *Biochemistry* **21**, 4953–4959 (1982).

[120] Forsyth, W. R., Antosiewicz, J. M. & Robertson, A. D. Empirical Relationships Between Protein Structure and Carboxyl pK_a Values in Proteins. *Proteins* **48**, 388–403 (2002).

[121] Wießalla, T. *Electrophysiological characterisation of the inward-directed light-driven proton pump Nanosalina Xenorhodopsin.* Bachelor thesis, Ruprecht-Karls Universität, Heidelberg, Germany (2017).

[122] Otto, H. *et al.* Aspartic acid-96 is the internal proton donor in the reprotonation of the Schiff base of bacteriorhodopsin. *PNAS* **86**, 9228–9232 (1989).

[123] Sineshchekov, O. A., Trivedi, V. D., Sasaki, J. & Spudich, J. L. Photochromicity of *Anabaena* Sensory Rhodopsin, an Atypical Microbial Receptor with a *cis*-Retinal Light-adapted Form. *J. Biol. Chem.* **280**, 14663–14668 (2005).

[124] Butt, H. J., Fendler, K., Bamberg, E., Tittor, J. & Oesterhelt, D. Aspartic acids 96 and 85 play a central role in the function of bacteriorhodopsin as a proton pump. *EMBO J.* **8**, 1657–1663 (1989).

[125] Subramaniam, S., Marti, T. & Khorana, H. G. Protonation state of Asp (Glu)-85 regulates the purple-to-blue transition in bacteriorhodopsin mutants Arg-82 → Ala and Asp-85 → Glu: The blue form is inactive in proton transpocation. *PNAS* **87**, 1013–1017 (1990).

[126] Lanyi, J. K., Tittor, J., Váró, G., Krippahl, G. & Oesterhelt, D. Influence of the size and protonation state of acidic residue 85 on the absorption spectrum and photoreaction of the bacteriorhodopsin chromophore. *Biochim. Biophys. Acta* **1099**, 102–110 (1992).

[127] Tittor, J., Schweiger, U., Oesterhelt, D. & Bamberg, E. Inversion of Proton Translocation in Bacteriorhodopsin Mutants D85N, D85T, and D85,96N. *Biophys. J.* **67**, 1682–1690 (1994).

[128] Karvaly, B. & Dancsházy, Z. Bacteriorhodopsin: A Molecular Photoelectric Regulator. *FEBS Lett.* **76**, 36–40 (1977).

[129] Druckmann, S. *et al.* The back photoreaction of the M intermediate in the photocycle of bacteriorhodopsin: mechanism and evidence for two M species. *Photochem. Photobiol.* **56**, 1041–1047 (1992).

[130] Haupts, U., Tittor, J., Bamberg, E. & Oesterhelt, D. General Concept for Ion Translocation by Halobacterial Retinal Proteins: The Isomerization/Switch/Transfer (IST) Model. *Biochemistry* **36**, 2–7 (1997).

[131] Lörinczi, E. *et al.* Voltage- and pH-Dependent Changes in Vectoriality of Photocurrents Mediated by Wild-type and Mutant Proteorhodopsins upon Expression in *Xenopus* Oocytes. *J. Mol. Biol.* **393**, 320–341 (2009).

[132] Kawanabe, A., Furutani, Y., Jung, K.-H. & Kandori, H. Engineering an Inward Proton Transport from a Bacterial Sensor Rhodopsin. *J. Am. Chem. Soc.* **131**, 16439–16444 (2009).

[133] Bergo, V. B. *et al.* Conformational Changes in the Photocycle of *Anabaena* Sensory Rhodopsin: Absence of the Schiff base Counterion Protonation Signal. *J. Biol. Chem.* **281**, 15208–15214 (2006).

[134] Dencher, N. A., Dresselhaus, D., Zaccai, G. & Büldt, G. Structural changes in bacteriorhodopsin during proton translocation revealed by neutron diffraction. *PNAS* **86**, 7876–7879 (1989).

[135] Koch, M. H. J. *et al.* Time-resolved X-ray diffraction study of structural changes associated with the photocycle of bacteriorhodopsin. *EMBO J.* **10**, 521–526 (1991).

[136] Subramaniam, S., Gerstein, M., Oesterhelt, D. & Henderson, R. Electron diffraction analysis of structural changes in the photocycle of bacteriorhodopsin. *EMBO J.* **12**,

1–8 (1993).

[137] Hoque, M. R. *et al.* A Chimera Na^+-Pump Rhodopsin as an Effective Optogenetic Silencer. *PLOS One* **11**, e0166820 (2016).

[138] Kovalev, K. *et al.* Molecular mechanism of light-driven sodium pumping. *bioRxiv* 2020.01.29.925347 (2020).

[139] Läuger, P. *Electrogenic Ion Pumps*, vol. 5 (Sinauer Associates, Inc., Sunderland, Massachusetts, 1991).

[140] Rakowski, R. F., Vasilets, L. A., LaTona, J. & Schwarz, W. A Negative Slope in the Current-Voltage Relationship of the Na^+/K^+ Pump in *Xenopus* Oocytes Produced by Reduction of External $[K^+]$. *J. Membrane Biol.* **121**, 177–187 (1991).

[141] Sörmann, J. *Ionentransport in Krokinobacter Eikastus Rhodopsin-2.* Doctoral dissertation, Goethe-Universität, Frankfurt am Main, Germany (2019).

[142] da Silva, G. F. Z., Goblirsch, B. R., Tsai, A.-L. & Spudich, J. L. Cation-Specific Conformations in a Dual-Function Ion-Pumping Microbial Rhodopsin. *Biochemistry* **54**, 3950–3959 (2015).

[143] Tilton, B. *et al.* Signal Transduction by CXC Chemokine Receptor 4: Stromal Cell–derived Factor 1 Stimulates Prolonged Protein Kinase B and Extracellular Signal–regulated Kinase 2 Activation in T Lymphocytes. *J. Exp. Med.* **192**, 313–324 (2000).

[144] Hesselgesser, J. *et al.* Identification and Characterization of the CXCR4 Chemokine Receptor in Human T Cell Lines: Ligand Binding, Biological Activity, and HIV-1 Infectivity. *J. Immunol.* **160**, 877–883 (1998).

[145] Lloyd-Evans, E., Waller-Evans, H., Peterneva, K. & Platt, F. Endolysosomal calcium regulation and disease. *Biochem. Soc. Trans.* **38**, 1458–1464 (2010).

[146] Abe, K. & Puertollano, R. Role of TRP Channels in the Regulation of the Endosomal Pathway. *Physiology* **26**, 14–22 (2011).

[147] Mattson, M. P. & Chan, S. L. Calcium orchestrates apoptosis. *Nat. Cell Biol.* **5**, 1041–1043 (2003).

[148] Li, G.-Y., Fan, B. & Zheng, Y.-C. Calcium Overload Is A Critical Step in Programmed Necrosis of ARPE-19 Cells Induced by High-Concentration H_2O_2. *Biomed. Environ. Sci.* **23**, 371–377 (2010).

[149] Rost, B. R. *et al.* Optogenetic acidification of synaptic vesicles and lysosomes. *Nat. Neurosci.* **18**, 1845–1852 (2015).

[150] Casey, J. R., Grinstein, S. & Orlowski, J. Sensors and regulators of intracellular pH. *Nat. Rev. Mol. Cell Bio.* **11**, 50–61 (2010).

[151] Clague, M. J., Urbé, S., Aníento, F. & Gruenberg, J. Vacuolar ATPase Activity Is Required for Endosomal Carrier Vesicle Formation. *J. Biol. Chem.* **269**, 21–24 (1994).

[152] Wescott, M. P. *et al.* Signal transmission through the CXC chemokine receptor 4 (CXCR4) transmembrane helices. *PNAS* **113**, 9928–9933 (2016).

[153] Pouysségur, J., Dayan, F. & Mazure, N. Hypoxia signalling in cancer and approaches to enforce tumour regression. *Nature* **441**, 437–443 (2006).

[154] Mahn, M., Prigge, M., Ron, S., Levy, R. & Yizhar, O. Biophysical constraints of optogenetic inhibition at presynaptic terminals. *Nat. Neurosci.* **19**, 554–556 (2016).

Appendix

List of Abbreviations

AAS	Atomic absorption spectrometry
ADP	Adenosine diphosphate
ANOVA	Analysis of variance
Arch	Archaerhodopsin-3
ASR	*Anabaena* sensory rhodopsin
ATP	Adenosine triphosphate
ATR	Attenuated total reflection
BLM	Black lipid membrane
BLQ	Blue-light-quenching
BR	Bacteriorhodopsin
CatCh	Calcium translocating channelrhodopsin
CCCP	Carbonyl cyanide *m*-chlorophenylhydrazone
ChR	Channelrhodopsin
ChR2	Channelrhodopsin 2
CLSM	Confocal laser scanning microscopy
CMV	Cytomegalovirus
CP	Cytoplasmic
CXCR4	C-X-C chemokine receptor 4
DDM	n-Dodecyl ß-D-maltoside
DMEM	Dulbecco's modified eagle's medium
DNase	Deoxyribonuclease
DPPC	1,2-Diphytanoyl-sn-glycero-3-phosphocholine
EC	Extracellular
EGTA	Ethylene glycol bis(2-aminoethyl ether)-N,N,N',N'-tetraacetic acid
eYFP	Enhanced yellow fluorescent protein
FBA	Feedback operational amplifier
FBS	Fetal bovine serum
FTIR	Fourier transform infrared
GLR	*Gillisia limnaea* rhodopsin
GPCR	G protein-coupled receptor
GRK	G protein-coupled receptor kinase
GS	Ground state
HEK293	Human embryonic kidney cell line 293

Hepes	4-(2-Hydroxyethyl)-1-piperazineethanesulfonic acid
HIV	Human immunodeficiency virus
IAR	*Indibacter alkaliphilus* rhodopsin
IC	Intracellular
IPTG	Isopropyl-ß-D-1-thiogalactopyranoside
IV	Current-voltage
KIE	Kinetic isotope effect
KR2	*Krokinobacter eikastus* rhodopsin 2
MES	2-(N-morpholino)ethanesulfonic acid
MR	Microbial rhodopsin
Na^+/K^+-ATPase	sodium-potassium adenosine triphosphatase
NaR	Na^+-pumping rhodopsin
NG108-15	Neuroblastoma glioma cell line 108-15
NMG	N-methyl-D-glucamine
NMR	Nuclear magnetic resonance
NM-R2	*Nonlabens marinus* rhodopsin 2
NpHR	*Natronomonas pharaonis* halorhodopsin
NsXeR	*Nanosalina* xenorhodopsin
OD	Optical density
optoXR	Vertebrate rhodopsin-GPCR chimera
P2A	Porcine teschovirus-1 2A
PCR	Polymerase chain reaction
PMSF	Phenylmethylsulfonyl fluoride
PoXeR	*Parvularcula oceani* rhodopsin
PR	Proteorhodopsin
RmXeR	*Rubicoccus marinus* rhodopsin
SB	Schiff base
SD	Standard deviation
SDF1	Stromal Cell-Derived Factor 1
SR	Sensory rhodopsins
SSM	Solid supported membrane
tCXCR4/MR	Optochemokine tandem
Tris	Tris(hydroxymethyl)aminomethane
UV-vis	Ultraviolet-visible
WHIM	Warts, hypogammaglobulinemia, immunodeficiency, and myelokathexis
WT	Wild type
XeR	Xenorhodopsin

Publication List

Feldbauer, K., Schlegel, J., Weissbecker, J., Sauer, F., Wood, P. G., Bamberg, E. & Terpitz, U. Optochemokine Tandem for Light-Control of Intracellular Ca^{2+}. *PLOS ONE* **11**, e0165344 (2016).

Weissbecker, J.*, Boumrifak, C.*, Breyer, M., Wießalla, T., Shevchenko, V., Mager, T., Slavov, C., Gordeliy, V., Wachtveitl, J. & Bamberg, E. Xenorhodopsin: Inward pump mechanism and spectroscopically and electrophysiologically obersevable Schiff base accessibility switch. (*equal contributions) (in preparation)

Sörmann, J., Eberhardt, P., Weissbecker, J., Bamberg, E., Wachtveitl, J. & Bamann, C. Competitive Ion Transport in *Krokinobacter Eikastus* Rhodopsin 2. (in preparation)

Declaration on Collaborative Work

Except where stated otherwise by reference or acknowledgment, the work presented was generated by myself under the supervision of my advisors during my doctoral studies. All contributions from colleagues are explicitly referenced in the thesis. The material listed below was obtained in the context of collaborative research:

Figure 7.4: Confocal laser scanning micrographs of tCXCR4/Arch expressing HeLa cells. CLSM was performed in collaboration with Dr. U. Terpitz and J. Schlegel from the Julius Maximilian University, Würzburg.

Part of the work was previously published in:

Feldbauer, K., Schlegel, J., Weissbecker, J., Sauer, F., Wood, P. G., Bamberg, E. & Terpitz, U. Optochemokine Tandem for Light-Control of Intracellular Ca^{2+}. *PLOS ONE* **11**, e0165344 (2016).

Declaration of Authorship

I declare that I have produced my doctoral dissertation single-handedly and only using the tools that were indicated therein. I have clearly acknowledged and identified all references borrowed from external sources. I confirm that I have not used the help of services on any commercial agency and that I have respected the principles of good scientific practice.

Place, Date

Signature